Frequency Domain Conductive Electromagnetic Interference Modeling and Prediction with Parasitics Extraction for Inverters

Xudong Huang

Dissertation submitted to the Faculty of the
Virginia Polytechnic Institute and State University
in partial fulfillment of the requirements for the degree of

Doctor of Philosophy
In
Electrical Engineering

Jih-Sheng Lai, Chairman
J. D. van Wyk
Douglas Nelson
Yilu Liu
Guo-Quan Lu

September 10, 2004
Blacksburg, Virginia

Keywords: electromagnetic interference (EMI), frequency domain, common mode (CM), differential mode (DM)

FREQUENCY DOMAIN CONDUCTIVE ELECTROMAGNETIC INTERFERENCE MODELING AND PREDICTION WITH PARASITICS EXTRACTION FOR INVERTERS

By
Xudong Huang
Jih-Sheng Lai, Chairman
Electrical Engineering

(ABSTRACT)

This dissertation is to focus on the development of modeling and simulation methodology to predict conductive electromagnetic interference (EMI) for high power converters. Conventionally, the EMI prediction relies on the Fast Fourier Transformation (FFT) method with the time-domain simulation result that requires long hours of simulation and a large amount of data. The proposed approach is to use the frequency-domain analysis technique that computes the EMI spectrum directly by decomposing noise sources and their propagation paths. This method not only largely reduces the computational effort, but also provides the insightful information about the critical components of the EMI generation and distribution. The study was first applied to a dc/dc chopper circuit by deriving the high frequency equivalent circuit model for differential mode (DM) and common mode (CM) EMIs. The noise source was modeled as the trapezoidal current and voltage pulses. The noise cut-off frequency was identified as a function of the rise time and fall time of the trapezoidal waves. The noise propagation path was modeled as lumped parasitic inductors and capacitors, and additional noise cut-off frequency was identified as the function of parasitic components. . Using the noise source and path models, the proposed method effectively predicts the EMI performance, and the results were verified with the hardware experiments. With the well-proven EMI prediction methodology with a dc/dc chopper, the method was then extended to the prediction of DM and CM EMIs of three-phase inverters under complex pulse width modulation (PWM) patterns. The inverter noise source requires the double Fourier integral technique because its switching cycle and the fundamental cycle are in two different time scales. The noise path requires parasitic parameter extraction through finite element analysis for complex-structured power bus bar and printed circuit layout. After inverter noise source and path are identified, the effects of different modulation schemes on EMI spectrum are evaluated through the proposed frequency-domain analysis technique and verified by hardware experiment. The results, again, demonstrate that the proposed frequency-domain analysis technique is valid and is considered a promising approach to effectively predicting the EMI spectrum up to tens of MHz range.

TO MY WIFE QUAN LI
AND MY PARENTS
SHIZHU FENG AND SHUCHUN HUANG

ACKNOWLEDGMENTS

Pursuing Ph. D degree is like going through dark jungle. I wouldn’t have reached the destination without the illumination of many other people.

I would like first to express my sincere appreciation to my advisor, Dr. Jih-Sheng Lai for his guidance, patience, encouragement and continuous support. He teaches me not only power electronics knowledge, but also the rigorous attitude towards research.

I am grateful to my committee: Dr. Daan van Wyk, Dr. Guoquan Lu, Dr. Douglas Nelson and Dr. Yilu Liu for their valuable suggestions on my research.

I would thank Elton Pepa, Huijei Yu, Chris Smith, Mike Gilliom, Amy Johnston, Changrong Liu, Junhong Zhang, Mike Schenck and Joel Gouker for their valuable suggestion, comments and discussions.

I would like to thank my parents, for their endless love and support. I highly appreciate my wife, Quan Li, for her continuous love and encouragement.

Table of Contents

List of Figures

List of Tables

Chapter 1 Literature Research and Present Challenge

The dissertation starts with a brief background of EMI. It then provides the motivation of the research work and a literature review of the existing work in related areas. Finally, the objectives of the research work are outlined and a brief description of the accomplishments in the subsequent chapters is presented.

1.1. Background and motivation of study

Electromagnetic interference (EMI) is undesirable electromagnetic noise from a device or system that interferes with the normal operation of the other devices or systems. Generally, EMI study is characterized into four different groups: conducted emissions, radiated emissions, conducted susceptibility, and radiated susceptibility [1, 2]. The first two groups target the undesirable emanations from a particular piece of equipment while the second two deal with a piece of equipment's ability to reject interference from external sources of noise. In this dissertation, we are only concerned with the conducted EMI emissions, which are defined as electromagnetic energy undesirable coupled out of an emitter or into a receptor via any of its respective connecting wires or cables [3, 4].

The purpose of studying conducted EMI is to understand what the causes are and how to prevent or suppress them. Ultimately the designed object should comply with its electrical environment or meet electromagnetic compatibility (EMC) criteria. Power inverters based motor drives have been traditionally used in industrial applications.

Recently they were found more and more applications in specialty purposes such as the automotive electric power steering systems, electric calipers and integrated starter-generators that tend to have more stringent EMC requirements [7-9]. Since the inverter based motor drives are known to have the tendency of producing large EMI, and the impact of inverter switching to the motor drive EMI is relatively unknown, it is necessary to have a systematic study to better understand inverter EMI so that the inverter design can comply with the environments that have more and more stringent EMC requirements.

In the conventional design methodology, EMC issues are addressed only after a prototype is built. At that stage, the traditional EMC remedies are confined to adding extra components, metal shields, and metal planes, etc. The worst situation is to redesign the entire system because the added components may interfere with the original control loop bandwidth. In this case, there will be a significant penalty both on the cost and on the time-to-market of the products. To avoid such "band-aid" solutions at the post-development, it is desirable to take EMI into account at the converter design stage.

With complexity of circuits and control methods, the EMI produced in a three-phase inverter is even much more difficult to study than in a dc/dc converter. Much of past research was focusing on the EMI impact to the motor, ac output cable and compatibility issue [10 – 27], but not on the inverter itself, which is indeed the major source of EMI in the entire motor drive system. Although EMI production mechanism has been regarded as a "black" magic, especially for complicated circuits such as a three-phase inverter, it is necessary to find ways of solving such a black magic so that the EMI prevention can be taken care of at the early design stage but not afterward. How to model and predict EMI is thus becoming the major subject in recent power electronics researches.

The conducted EMI noise in a PWM inverter can be viewed as consisting of two major parts, differential mode (DM) noise and common mode (CM) noise [5, 6]. The general distribution mechanism for CM noise and DM noise is illustrated in Fig. 1.1. The DM noise propagates between power lines including line and neutral without going through ground. While the CM noise propagates both power lines and ground, for instance, it goes through not only between line and ground, but also between neutral and ground. In order to model and predict EMI generated by a three-phase inverter, it is necessary to analyze and model both CM noise and DM noise generation and propagation mechanism.

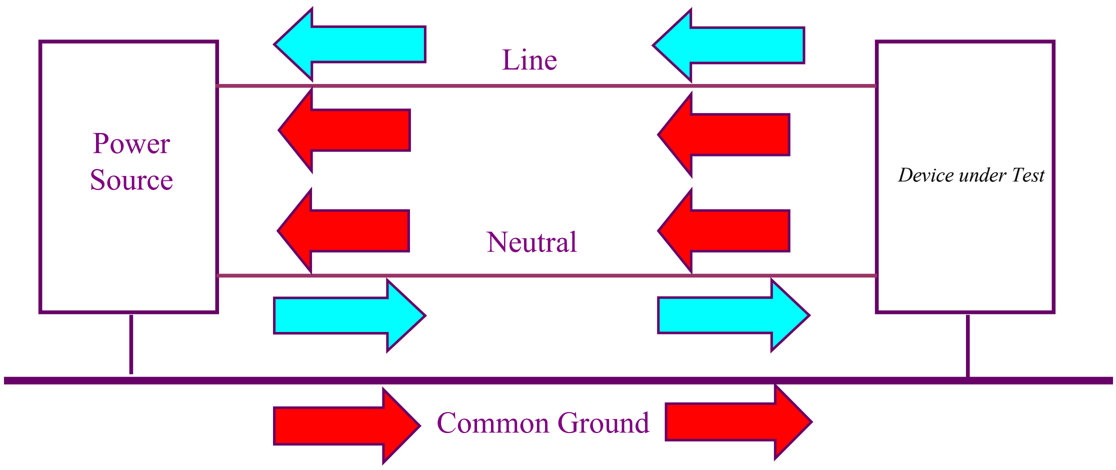

Fig. 1.1 The general distribution mechanism of CM and DM noise

1.2 Literature review on conductive EMI modeling and prediction

The purpose of EMI modeling of power converter is to get a better understanding of EMI generation mechanism, to predict the EMI level and to avoid or to alleviate EMI problem at the design stage. The goal to be aimed at is to provide insightful analysis on EMI generation and propagation mechanism, to predict with reasonable accuracy and to cover a wide frequency range. The basic process of EMI modeling and prediction requires two steps: (1) extracting parasitic parameters of PCB and circuit components to build high frequency circuit model and (2) predicting EMI emission with mathematics methods.

Parasitics exist in all kinds of element in power converters such as power device, capacitors, magnetic component, PCB traces, wire cables, etc. Several research efforts have been reported on methods of extracting parasitic parameters [28-35]. These methods can be classified into two approaches, measurement-based method and mathematics-based method. The mathematics method is to solve Maxwell field equation based on physical structure, material property and the geometry information. Although many different mathematics methods have been proposed, they can be divided into three categories: finite element methods (FEM), finite different methods (FDM) and method of moments (MoM). FEM and FDM techniques that solve the Maxwell's differential field equations require extensive computation and sometimes show poor convergence. The simulation tools using these methods are Maxwell 2D, Maxwell 3D, etc. MoM solves the Maxwell's integral equation instead so that it can greatly reduce the computation cost [31]. There are some simulation tools using MoM technique, such as Maxwell Q3D, etc. Some literatures claim that Maxwell Q3D is based on partial element equivalent circuit

(PEEC) method. This is misconception because PEEC model is the result of MoM or Maxwell Q3D, not the technique being used to solve Maxwell field equation. For the measurement-based method, the commercially off-the-shelf impedance analyzer can be used as a convenient tool for relatively large parasitics, but for small parasitics such as nano-Henry (nH) or sub-nH inductances, the time domain reflectory (TDR) method was proposed [32].

Once the parasitic parameters are extracted, the next step is to mathematically model and predict EMI emission. Recently, more and more mathematical modeling and analysis on electromagnetic interference (EMI) sources and propagation had shed a light on a better understanding of the EMI production mechanism [36– 66]. These researches can be divided into two classes, time domain approach and frequency domain approach, as shown in Fig. 1.2. The former method is to have time-domain simulation followed by "fast Fourier transform" (FFT) analysis. While the frequency domain approach is based on noise source/propagation path concept, which can be further divided into two categories, empirically measurement method and analytical method.

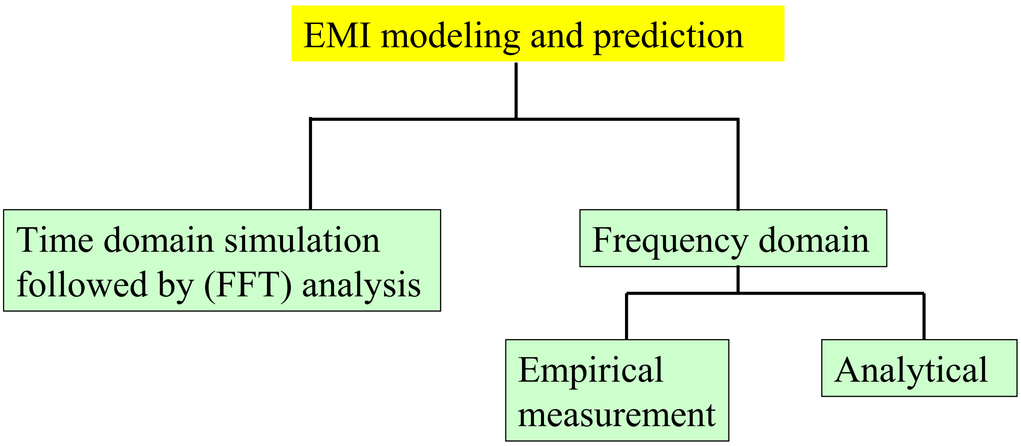

Fig. 1.2 Present approaches of EMI modeling and prediction

1.2.1 Time Domain Approach

The time domain method was performed by circuit simulator such as PSPICE, Saber. It was proven to be effective for differential mode (DM) EMI, which dominates the low-frequency region including the pulse-width-modulation (PWM) frequency and the resonant frequencies caused by the parasitic elements coupling with device switching dynamics in the EMI excitation [45]. However, this method is time consuming and requires a large amount of data storage because the simulation step needs to be very fine, typically in nano seconds. Table 1.1 shows the time constant of different periods. It is tedious for circuit simulation to finish several fundamental cycles with simulation step of nano seconds because the fundamental cycle is several orders of magnitude larger than the switching transition.

Table 1.1 Time constants of different periods for a motor drive

On/off Transition	ns
Switching period	us
Fundamental period	ms

For dc/dc converters, the simulation using the classical approach is possible because the simulation time is in the order of switching period, which is relatively manageable. For motor drive inverters, it is very difficult to reach the steady-state operating condition. The nonlinear characteristic of the semiconductor and many stray parameters make the model very complicated and sometimes lead to convergence problems in simulation. To include all the parasitic components for common mode (CM) EMI study, the time-domain simulation can be even more troublesome, and the FFT results are difficult to match the experimental results [45 - 47]. Furthermore, the time domain method cannot provide the deep sight into converter EMI behavior and it lacks the appreciation of the EMI mechanism, such as how the noise is excited and how it is propagated.

1.2.2 Frequency Domain Approach

The frequency domain method is based on noise source/propagation path concept. In conducted EMI measurement, a standard network, known as Line Impedance Stabilization Network (LISN), is used to provide standard load impedance to the noise source. The voltage across this load is measured as conducted noise emission of the device under test. Seen from the LISN, the whole system could be simplified as equivalent noise source, noise path and noise receiver. Here the LISN serves as the noise receiver. This basic concept is shown in Fig. 1.3.

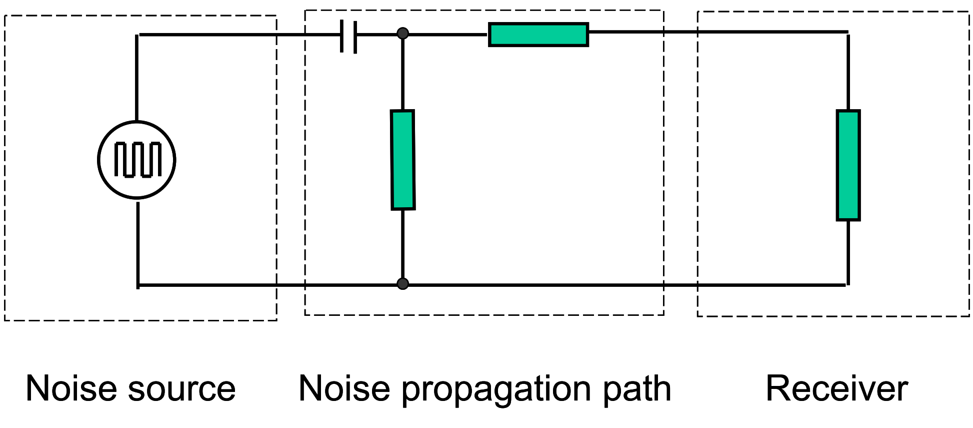

Fig. 1.3 Noise source and propagation concept

Noise source is time variant. Noise path is also time-variant and non-linear due to the switching operation. The noise measured at LISN is determined by the excitation of the noise source and the response of the noise transmission network. If in frequency domain, the noise source is expressed by its transfer function as N(s), and the noise transmission network is expressed by its transfer function as Z(s), then the noise measured at LISN, F(s), can be expressed in frequency domain as the function of N(s) and Z(s).

If the source is voltage source, then

$$F(s) = \frac{N(s)}{Z(s)} \tag{1-1}$$

If the source is current source then

$$F(s) = N(s)Z(s) \tag{1-2}$$

If the magnitude of each item in the above formula is represented in dB, then we have following equation:

$$20\log\left|F(s)\right| = 20\log\left|N(s)\right| + 20\log\left|Z(s)\right| \tag{1-3}$$

or

$$20\log\left|F(s)\right| = 20\log\left|N(s)\right| - 20\log\left|Z(s)\right| \tag{1-4}$$

Hence, the problem of EMI prediction becomes the problem of EMI noise source determination and EMI noise propagation path determination. There are also two methods to determine the noise source and noise propagation path. One is through empirical measurement and the other is through analytical method.

The empirical methods either measure the noise source through probe and noise path through network analyze directly, or calculate the Thévnin equivalent circuit for the noise source and noise path based on measurement results [55-57]. This method is good for

EMI characterization, but not appropriate for EMI prediction. First, because the measurement can only be done after the circuit prototype is built, it lacks of the essence of prediction which can be done without prototype. Second, this method belongs to "black box" in nature because the noise source and noise propagation path determined in this method have no physical meaning. Neither the relationship between parasitics of components and noise propagation path is indicated nor is the relationship between switching pattern and noise source established. This method cannot indicate the relationship between the performance and the components in the converter. Furthermore this way cannot give the converter designer a concrete concept on how to change some key components parameter to comply with the EMC standards. In addition, from measurement point of view, these methods are only suitable for circuit with a noise source that is conveniently measured, not for multiple noise source circuit like a three-phase inverter. This is due to the fact that it is extremely difficult to measure several noise sources simultaneously and there are also interaction between these sources. In short, these methods provide little insight how EMI generate and propagate.

It is also crucial that the noise source and noise propagation path have a predefined physical meaning, hence they can be modified according to EMI requirement at design stage. The analytical method which was derived from circuit operation analysis fits the above criteria and is of interest in the EMI prediction of power electronics circuit.

.

The analytical frequency-domain method was proposed in [53, 54] based on the description of the system topology using transfer function and a direct frequency representation of the noise sources. The "frequency-domain" analysis using transfer functions of noise path and direct frequency identification of the noise sources can be used to avoid computational convergence problem in time domain simulation.

The present status of analytical frequency domain EMI modeling and prediction can be divided into three categories from converter topology perspective: boost derived power factor correction (PFC) converter, buck (chopper) converter, and three-phase inverter.

In boost derived PFC converter, Crebier proposed in [60, 61] a voltage perturbation source as EMI source for both common mode noise and differential mode noise. However, the model derived is suitable for current-fed converters as boost converters and its associated PFC circuit while not for voltage-fed converter. For our purpose, this scope of the research will concentrate on voltage source converter such as buck or chopper circuit and three-phase inverter.

For modeling of buck converter, Nave proposed a current source to be used as the differential mode noise source and the voltage source for common mode noise source [53 – 54]. This method is appropriate for PWM switching frequency harmonics analysis, but far from accuracy at the high frequency range due to simplification of the model. No parasitics effect was considered in his paper and the interaction between CM and DM noises was neglected. Roudet considered the effect of parasitic component in [19] and showed the interaction between CM and DM noises. This model is not so accurate because only a current source is regarded as DM noise source; the parasitic capacitance of the device is not considered in DM noise model. The other disadvantage is that it lacks of a complete model to replace the nonlinear device so that the model is hardly adopted in multiple device converter circuit such as three phase inverters.

Few literatures can be found aiming at dealing with the EMI modeling of three phase inverter. Chen proposed a simple model to identify major EMI source. In [65], the DM noise source is the dc link current and the DM noise path is the dc link capacitor. There are several reasons that prevent this method providing reasonable results beyond a few MHz. Neither CM noise source model nor DM noise source model is analytically derived based on modulation scheme, therefore the source model is not accurate enough. In addition, the noise path mode is far from completed because the device parasitics and the power bus parasitics are not included.

Ran published two papers dealing with conducted electromagnetic emissions in induction motor drive system. Apart from the time domain analysis in one paper, the other paper [66] mainly focused on frequency domain model. In this paper, the modulation operation of inverter was given consideration. However, the CM source only considered the CM current going through the motor side, not that going through the inverter side that are parasitic capacitance between the device and the heat sink. The DM noise source is modeled as a voltage source, which is conflicted with the DM noise generation mechanism, where the DM noise is supposed to be current-driven. Moreover, the noise path model is far from completed because the device parasitics and the power bus parasitics are not included. Finally, the interaction between the CM and DM noise sources was totally neglected as well.

In short, the status of EMI modeling is summarized in the following:

1. Present methods provide little insight into the EMI generation and propagation in the medium and high frequency ranges.
2. For three phase inverter circuit, the complexity of PWM pattern has not been taken into account during EMI modeling. Neither analytical CM source model nor analytical DM source model has been presented with regard to switching patterns. The lack of knowledge in PWM impact to EMI producing mechanism could result in either over-design or under-design for the EMI filter.
3. The relationship between parasitic value in noise propagation path and the peaks in EMI spectrum needs to be established. The dominant parasitics in circuit components need to be identified.

From the above review, it can be seen that the first essential part of EMI prediction is to get a high frequency equivalent circuit that can agree with the EMI propagation mechanism. The next stage is to get more accurate representation of noise source and noise propagation path in frequency domain.

1.3 Outline of the Dissertation

The main emphasis of this dissertation is on the development of the methodology for modeling and predicting conductive EMI for a three-phase inverter in frequency domain. Since each phase in a three-phase inverter operates either as a buck converter or as a chopper, it is necessary to start from the single chopper circuit analysis to ensure the validity of the methodology.

In chapter 2 DM EMI mechanism for a single phase chopper is studied first. The limit of the conventional frequency domain model is presented. The conventional model fails to predict DM EMI up to high frequency range due to the absence of parasitic components. A new high frequency equivalent model including dc bus parasitic and device lead inductance and output capacitance is proposed. The parasitics inductance is obtained through Maxwell Q3D software. To verify the proposed DM model, time domain simulation and experiment were performed. Adding high frequency across dc bus will change the DM noise propagation path significantly. The proposed frequency domain method successfully predicts its impact and the result matches with the hardware experiment. After finishing the study on DM EMI, CM EMI mechanism for single phase chopper is investigated. The conventional model only considers the trapezoidal waveform as the CM noise source and neglects the voltage ringing as additional important noise source in the high frequency range. This causes the inaccuracy of the prediction in high frequencies. The proposed CM high frequency equivalent model includes this voltage ringing as the result of either a current source excitation or voltage source excitation. The closed-forms of this noise source expression in frequency domain are presented. The experimental CM EMI spectrum agrees well with the predicted result.

Second, a frequency domain approach to prediction of DM conducted EMI from three-phase inverter has been presented in chapter 3. This approach relies on identification of noise source based on inverter operation and extraction of parasitic parameters of the inverter components to predict the EMI currents produced in an inverter circuit. The analytical expression of DM noise source model was derived based on double Fourier technique. Methodologies for extraction of parasitic parameters of the inverter circuit are developed using finite element analysis. With accurate noise source and path models, the proposed "frequency-domain analysis" method avoids the computational problems in the conventional "time-domain analysis" and effectively predicts the DM EMI performance in high frequencies for an SVM based inverter. After the frequency domain analysis of DM EMI for three phase inverter is verified, it is feasible to evaluate the effect of different modulation schemes on DM EMI spectrum through frequency domain method analytically. Different modulation scheme leads to different noise sources and the noise sources under different modulation scheme are derived analytically in close form respectively. The calculated results are verified through experiment test. Compared with continuous PWM scheme, the discontinuous PWM scheme has a significant portion running with zero duty, and thus the overall produced noise source is lower in frequency domain, including in high frequency regions.

Chapter 4 proposes the frequency domain approach to prediction of CM conducted EMI from three-phase inverter. The conventional method usually derives the CM noise source and CM noise path from the AC load side, while this proposed approach focuses on the inverter side to identify the CM noise source and parasitic parameters of the inverter components in order to predict the CM EMI currents. A simplified CM circuit model of CM EMI in switching frequency and its harmonics range is proposed first and the noise source models under different modulation schemes are analytically derived through double Fourier technique. The impact of modulation index on CM EMI spectrum with different modulation schemes also evaluated analytically through frequency domain methods. The impact mainly occurs in the switching frequency and its harmonics range. To predict the CM EMI up to tens of Mega Hz range, additional CM noise source caused by voltage ringing is identified. A CM high frequency equivalent circuit model is derived with extracted parasitic parameters of the inverter circuit to predict the noise peak caused by the resonance of parasitic components. Compared with experimental results, the proposed "frequency-domain analysis" method effectively predicts the CM EMI performance not only in switching frequency and its harmonics range but also in high frequency range. The EMI performance, however, is highly affected by the modulation scheme both in the switching frequency related harmonic frequencies and in the noise path related resonant frequencies. In high frequency range, discontinuous PWM gives lowest noise envelop due to less switching action.

Finally, Chapter 5 summarizes the entire dissertation and proposes some ideas for future work.

Chapter 2 Frequency Domain EMI Modeling and Preditction – Single phase chopper

To avoid time-consuming computing process, the frequency-domain simulation approach was suggested in [53]. The frequency-domain approach requires knowledge on noise source and propagation path but significantly reduces computational effort, and thus is recommended as the preferred approach for EMI modeling and simulation. The basic idea is to model the switching noise source as a trapezoidal wave, which has a known frequency-domain characteristic, and then apply this source to the parasitic network with frequency-domain analysis. To make this approach effective, however, it is necessary to model the differential mode (DM) and common mode (CM) parasitic network separately and compute them independently.

Single phase chopper, a partial inverter phase leg, is used in this chapter as an example to show how to apply frequency-domain approach. Since it is the basic circuit for three phase inverter, it is necessary to study single phase chopper first before the investigation of three phase inverter. Although the circuit is simple, the result can be extended to more complex circuits and phenomena that will be discussed in the sequent chapters.

DM noise current, unlike CM noise current, propagates between power lines without going into ground. However, it has impact on CM noise propagation in high frequency range as investigated in the sequent chapters. Hence, the first step of EMI modeling is to derive an accurate DM EMI model for single phase chopper. In this chapter, we start with the conventional model for DM EMI modeling and prediction of single phase chopper. The limit of this conventional method, which lacks the accuracy for noise source and noise path determination, is identified. A high frequency equivalent circuit for DM EMI prediction and modeling is proposed, which focuses on more accurate noise source and parasitic path identification. The active device in the circuit is regarded as noise source which is replaced with a current source in parallel with device output capacitance. The parasitic components are identified using parasitics extraction tool – Maxwell Q3D™. The noise source and noise propagation path are represented in frequency domain by close form. It can be seen that the resonant point in the noise propagation path determines the noise peak occurring in the DM noise spectrum. This indicates that the EMI spectrum at high frequency range is mainly determined by the resonance of parasitic components.

CM noise, which is conducted through parasitic capacitance between component and ground plane, is another important aspect of EMI study. Under most cases, the CM noise could be more severe than DM noise. Moreover, CM model noise and differential noise are even related. The limit of the conventional method, which lacks the accuracy for CM noise source and noise path determination, is identified. We propose a high frequency equivalent circuit for CM EMI prediction and modeling, which focuses on more accurate noise source and parasitic path identification. The CM noise source and noise propagation path are represented in frequency domain by close form. It can be seen that the resonant point in the CM noise propagation path determines the noise peak occurring in the CM noise spectrum. This indicates that the CM EMI spectrum at high frequency range is mainly determined by the resonance of parasitic components.

To verify the proposed frequency domain method, Time domain simulations followed by FFT analysis and hardware experiments were performed. The results of these methods are successfully matched for the studied circuit.

Further verification are then directed to the EMI improvement with manipulation of the dc bus capacitor, which is a high frequency polypropylene capacitor and serves as the snubber to suppress the device turn-off voltage spike. This capacitor changes the EMI spectrum envelope drastically due to the resonance between this dc snubber capacitor and the parasitic inductance of the PCB track. The CM EMI and DM EMI with the snubber capacitor are studied with the proposed frequency domain methods. The results indicate that the frequency domain analysis with accurate noise source and parasitic modeling is an effective tool for EMI prediction. With its simplicity and numerical stability, this method is thus recommended for the study of a much more complicated converter system.

2.1 Differential mode modeling and prediction

Topologically, the three-phase PWM inverter can be configured with a total of eight different sub-circuits [75]. In order to verify the proposed approach, it is necessary to simplify the analysis, and thus only a part of the inverter phase-leg with lower switch and upper diode as the active component is considered in the following discussions. This circuit can also be regarded as voltage-fed single phase chopper circuit.

2.1.1 Conventional method of DM EMI prediction

Initially, the conventional method of DM EMI prediction for voltage-fed circuit should be reviewed. Fig. 2.1 shows the simple chopper circuit that consists an active device, and a freewheeling diode, and an electrolytic capacitor with an equivalent series resistor (ESR), R_{dc} and inductor (ESL), L_{dc}. The LISN is inserted between the dc source and the electrolytic capacitor to prevent the noise current from flowing to the source and to collect the noise voltage.

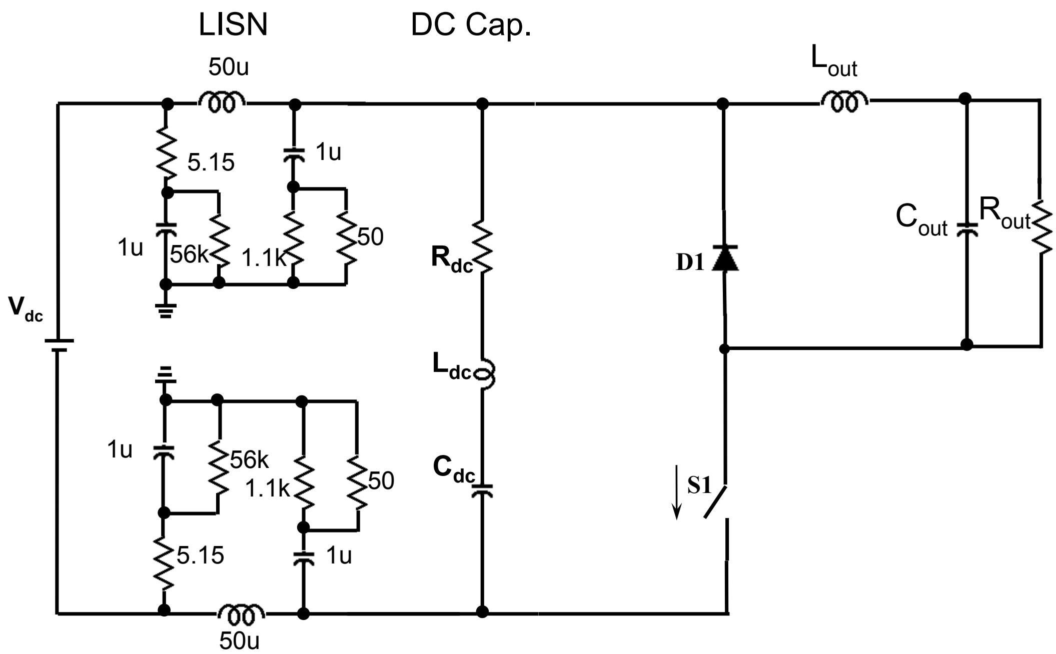

Fig. 2.1 Single phase Chopper Circuit

M. Nave proposed that the DM noise source can be determined as a current source which is seen by dc link and the noise path can be determined as the parasitics of the decoupling capacitors across the dc bus. Fig. 2.2 shows the equivalent circuit based on the conventional model and its noise source representation.

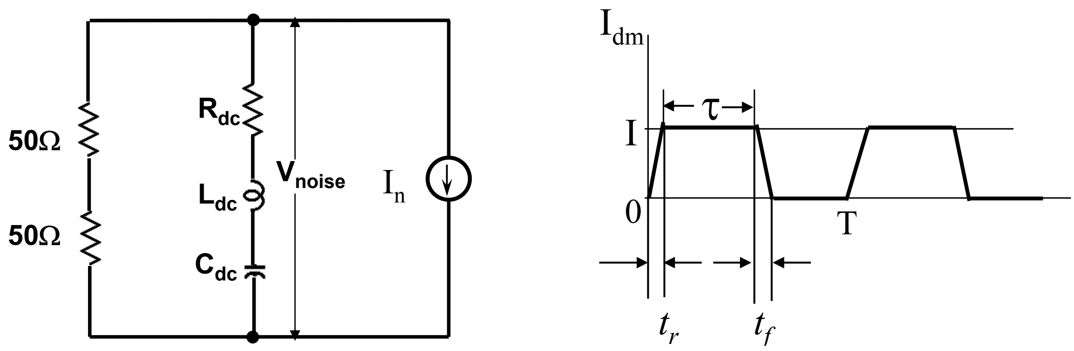

Fig. 2.2 Conventional DM EMI Model and noise source representation.

The switching noise source can be considered as a trapezoidal pulse train. Although the actual waveform will have different current rise and fall times (t_r and t_f), to simplify analysis, it is reasonable to assume that $t_r = t_f$. The frequency domain representation of the DM noise current can then be expressed in (2-1).

$$I_n = 2Id\frac{\sin(n\pi d)}{n\pi d}\frac{\sin({}^{n\pi t_f}\!/_{T})}{{}^{n\pi t_f}\!/_{T}}e^{-j\frac{n\pi(\tau+t_f)}{T}} \tag{2-1}$$

In the above expressions, d is the duty cycle, T is the inverter switching period, I is the current amplitude, τ is the on time of the switch and n is the harmonic order.

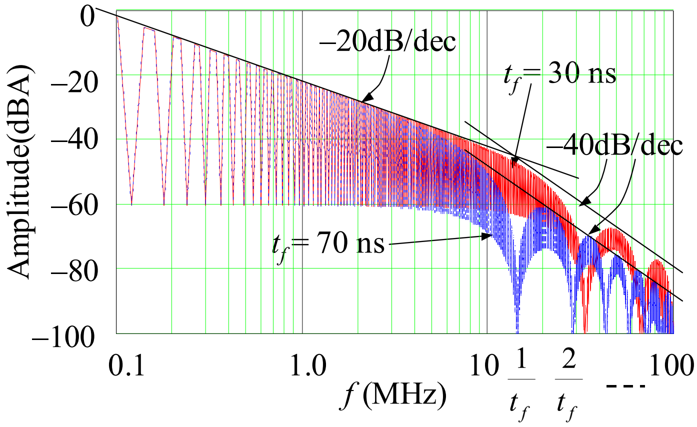

Fig. 2.3 Spectral representation of noise source with different fall times

Fig. 2.3 shows the spectral representation of a current source with 30 and 70 ns fall time, respectively. The noise source plot shows an initial –20 dB/dec drop, and an additional –20 dB/dec drop in the high frequency region, which is attributed to the switching period and fall time. A slower switching speed means larger t_f, which subsequently yields a lower cut-off frequency or less noise in high frequency range. Different fall times can be obtained by varying the gate resistance. A larger gate resistance would result in a lower noise source spectral envelope.

Fig. 2.4 shows the noise propagation path of conventional method which is the parasitic inductance and resistance of the decoupling capacitor. Neither inter-connect parasitics nor device parasitics are included in the noise propagation path. Fig. 2.5 shows derived propagation path transfer function plotted by the Mathcad. The flat part up to 1 MHz is dominated by parasitic resistance and beyond that the parasitic inductance becomes dominant.

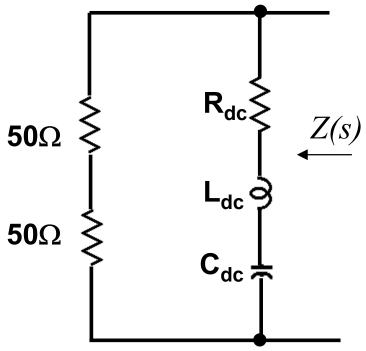

$$Z(s)=\frac{V_{noise}(s)}{I(s)}=-\frac{R_{dc}+sL_{dc}+\dfrac{1}{sC_{dc}}}{100+(R_{dc}+sL_{dc}+\dfrac{1}{sC_{dc}})}100$$

Fig. 2.4 noise propagation path of conventional method

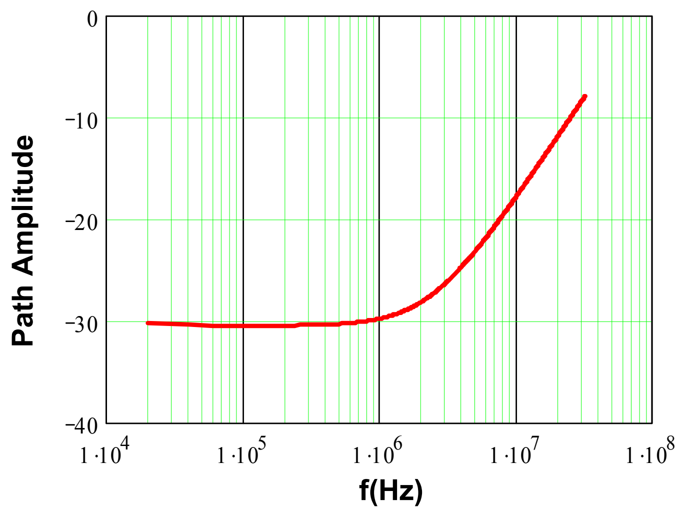

Fig. 2.5 Plot of noise propagation path transfer function

The DM noise voltage observed at LISN can be calculated by (2-2)

$$V_{noise}(f)=I(f)\cdot Z(f) \tag{2-2}$$

Fig. 2.6 shows the calculated result of DM noise spectrum with different switching speed. Compared to the experimental result shown in Fig. 2.7, the calculated result matches with the experimental result from low frequency range (hundreds of kHz) up to 10 MHz, but fails to predict the noise peak beyond 10 MHz.

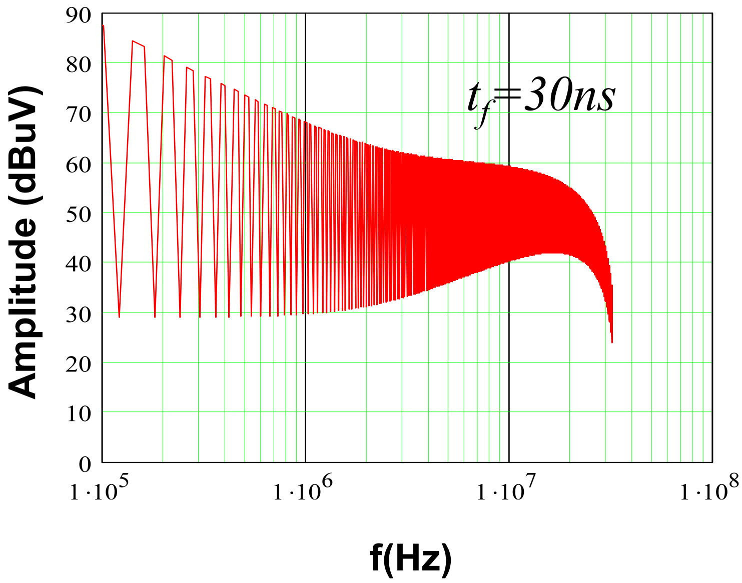

(a)

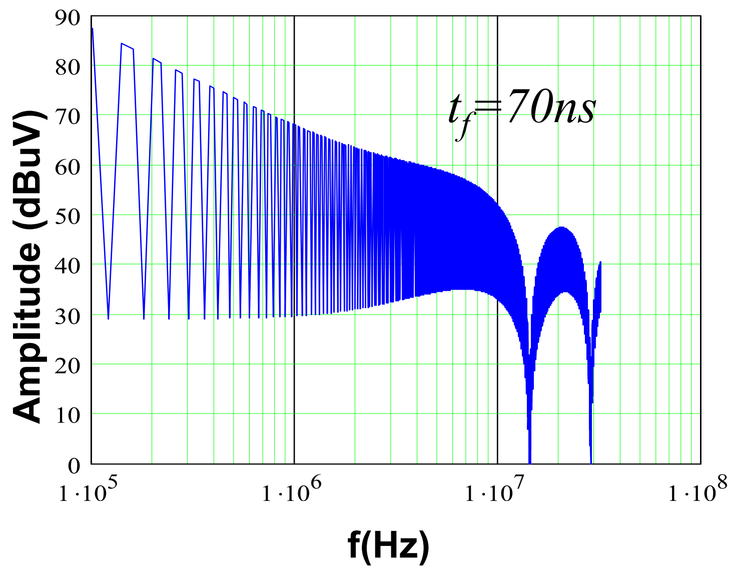

(b)

Fig. 2.6 Calculated result of DM noise spectrum based on the conventional method (a) t_f=30 ns (b) t_f=70 ns

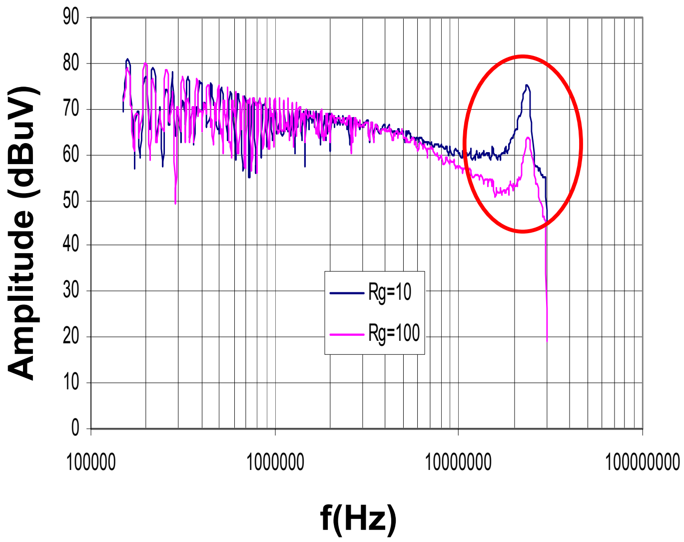

Fig. 2.7 Experimental result of DM EMI spectrum

The discrepancy between the calculated result and experimental result presents that the conventional method is not complete for high frequency EMI prediction. Interconnect parasitics and device parasitics should be included and the cause of the dominant noise high frequency peak should be identified.

2.1.2 The proposed DM model

Since the parasitic inductance plays an important role on the EMI performance, all the parasitic inductance values have to be known in order to predict EMI performance accurately. Fig. 2.8 shows the single phase chopper circuit with parasitic inductance. Here, the parasitic inductance includes the PCB track inductances (L_{dc+}, L_{mid} and L_{dc-}), top device lead inductance L_t and output capacitance C_t, bottom device lead inductance L_b and output capacitance C_b and ESL of electrolytic capacitor. These parasitic inductance can be obtained through parasitics extraction tools or measurement with impedance analyzer.

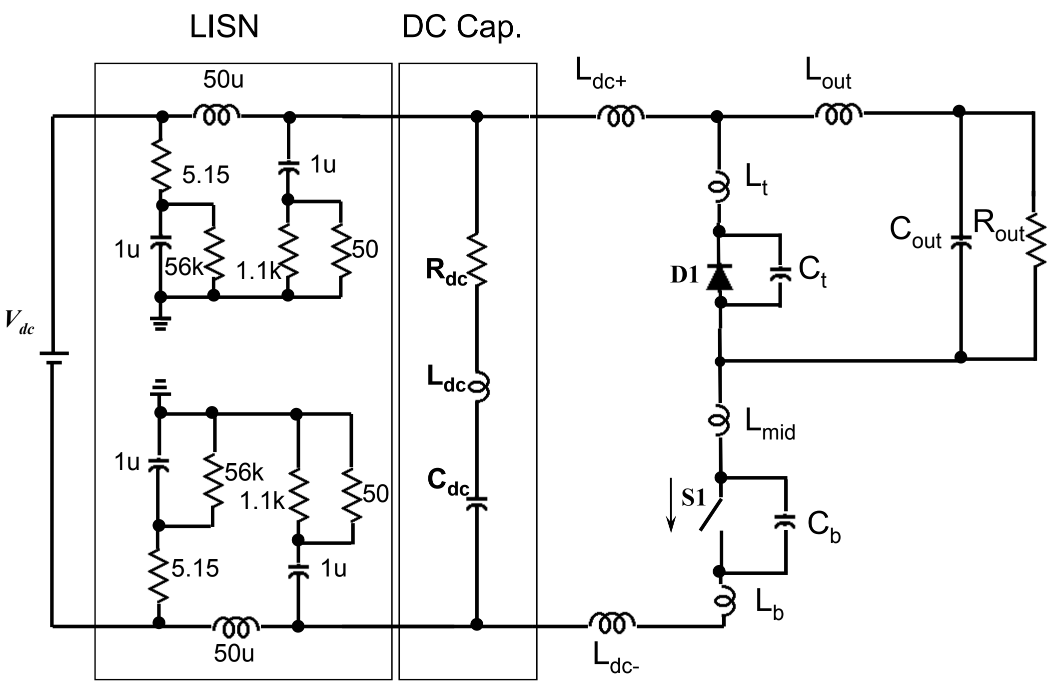

Fig. 2.8 Chopper Circuit with parasitic inductance

The concept of frequency domain EMI prediction is to get the frequency domain representation of the noise source and noise path respectively, then multiply them together, therefore the frequency domain equivalent circuit with parasitics must be derived first. In convention model, only the PWM switching current can be seen by the decoupling capacitor. In fact the decoupling capacitor absorbs not only the PWM switching current, but also the parasitic ringing current caused by the oscillation between the parasitic inductance and device output capacitance. Fig. 2.9 shows the waveform of the dc link current which is the sum of PWM switching current and parasitic ringing current. This explains why the conventional model can predict the DM EMI successfully in low frequency range but fail in high frequency range.

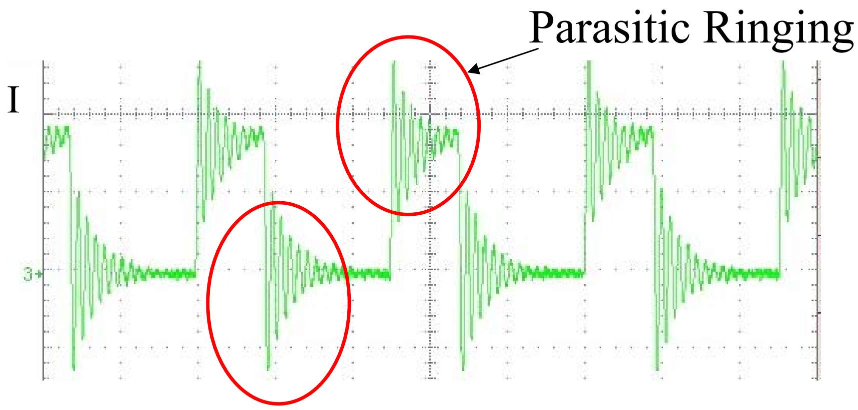

Fig. 2.9 DC link current waveform

A new high frequency equivalent circuit of the chopper circuit is necessary for DM EMI modeling at high frequency range. Such an equivalent circuit has to be derived based on the circuit operation analysis. It can be seen from Fig. 2.9 that the parasitic ringings occur during switching transient. For the chopper circuit, there are two switching transient, one is bottom active switch turn-off, the other is bottom active switch turn-on, which is equivalent to top switch turn-off. Two high frequency equivalent circuits can be derived for these two switching transients respectively. Fig. 2.10 shows these circuits.

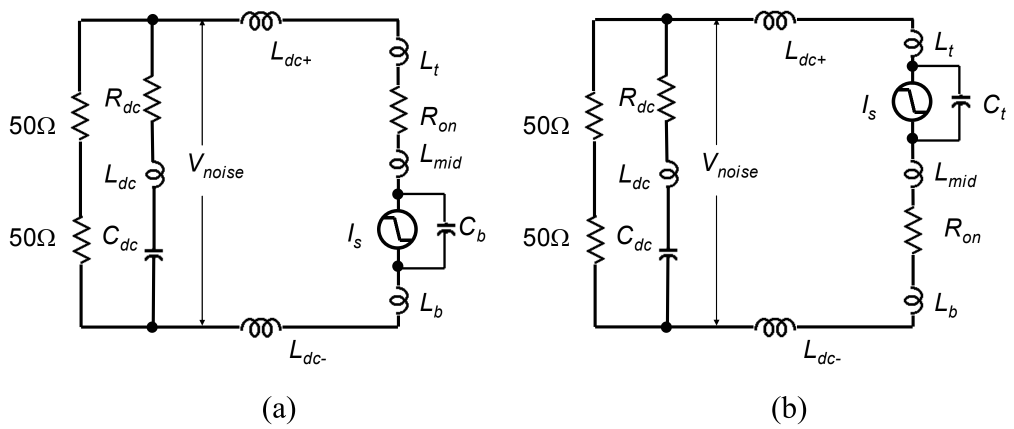

Fig. 2.10 High frequency equivalent circuits during switching transient (a) during bottom device turn off (b) during top device turn off

It is indicated from the above circuits that the parasitic ringing is caused by the resonation between loop parasitic inductance and device output capacitance. For instance, during bottom device turn off, the output capacitance of the bottom device resonates with loop parasitic inductance; while during top turn device turn-off, which is the same of bottom device turn-on, the output capacitance of the top device resonates with the loop inductance. If the top device parasitic capacitance is the same as the bottom device output capacitance, which is the case for two devices in a phase leg of inverter, these two equivalent circuits can be synthesized to a unified circuit.

Fig. 2.11 illustrates the proposed DM mode for EMI prediction that is generalized from the two equivalent circuits shown in Fig. 2.10. C_{oss} represents the device output capacitance. The proposed DM model should be the model in which the real dc link can be represented. In this model, the current source representation is still the same of that in conventional model, however, the parasitic ringing current has been taken into account by adding all the interconnect parasitics and device parasitics. Not only the PWM switching current can be seen by the decoupling capacitor, but the parasitic ringing current as well.

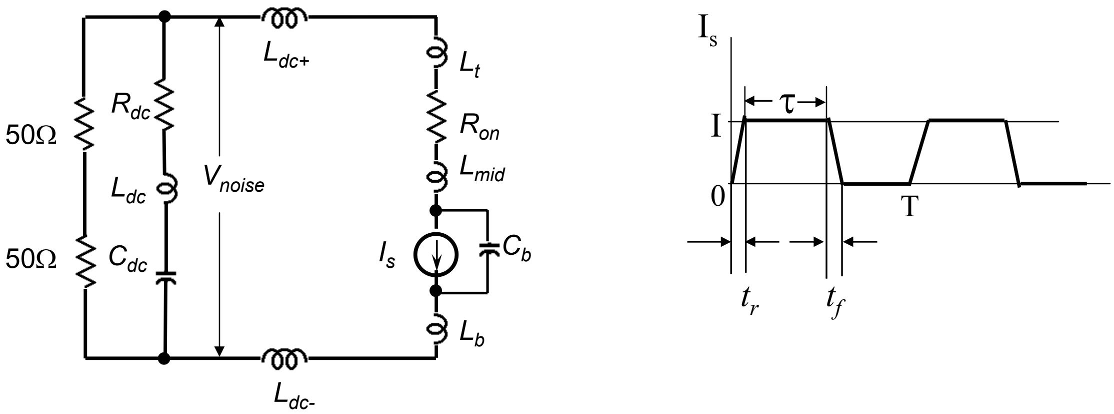

Fig. 2.11 Proposed DM noise model and noise current source representation

From another perspective, the nonlinear switch should be replaced by a voltage or current source to predict the EMI spectrum in frequency domain. The switch is commonly represented as a current source for DM mode modeling. Hence this proposed model can be viewed that the active switch is replaced with a current source in parallel with device capacitance while the free-wheeling diode is shorted.

It is noted that the diode reverse recovery is approximated as parasitic ringing in this frequency domain approach during diode turn-off. This is not the same as the switching characteristic of diode reverse recovery. However, the approximation leads to the convenience for the modeling process without too much sacrifice at result accuracy. The typical waveform of diode reverse recovery is shown in Fig. 2.12. The first peak of device current is caused by the recovered charge Q_{rr} while the rest of the peaks are caused by parasitic ringing of the circuit. The modeling method assumes the first peak is also determined by parasitic ringing instead of reverse recovery charge, which could result in the slight difference in the amplitude of the first peak. Since this only happens about one period of parasitic resonance and the EMI result is shown in log scale, the assumption will not have significant effect on the predicted result.

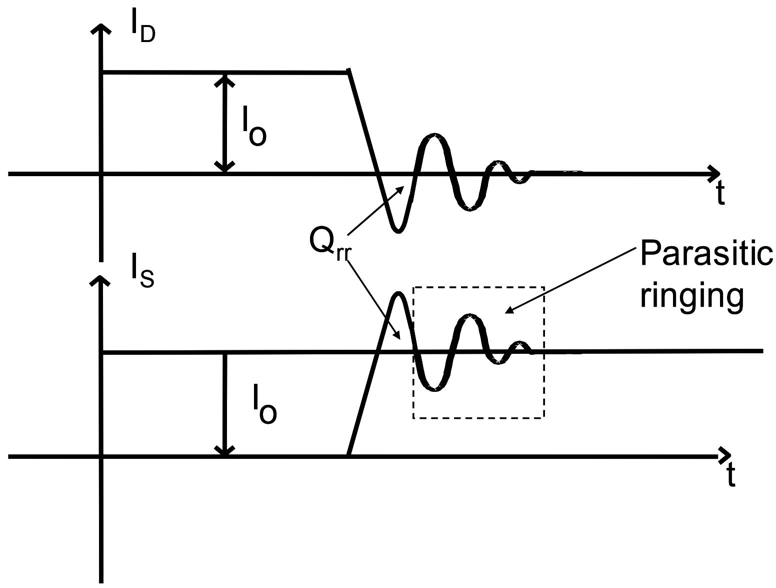

Fig. 2.12 Typical waveforms of diode reverse recovery

2.1.3 DM Noise Path Impedance Modeling and Parasitics Characterization

The noise propagation path impedance transfer function can be obtained by solving the equivalent circuit shown in Fig. 2.11 and can be expressed in (2-3).

$$Z(s) = \frac{V_{noise}(s)}{I(s)} = -\frac{1}{1+\frac{s}{Q\omega_0}+(\frac{s}{\omega_0})^2} \cdot \frac{R_{dc}+sL_{dc}+\frac{1}{sC_{dc}}}{100+(R_{dc}+sL_{dc}+\frac{1}{sC_{dc}})} 100 \tag{2-3}$$

The frequency of resonant peak is given in

$$\omega_0 = \frac{1}{\sqrt{L_{loop}C_{oss}}} \tag{2-4}$$

The damping factor is given by

$$Q = \frac{1}{R}\sqrt{\frac{L_{loop}}{C_{oss}}} \tag{2-5}$$

The loop inductance and loop resistance are given by

$$R = R_{dc} + R_{dcplus} + R_{dc\min us} + R_{middle} + R_{on} \quad (2\text{-}6)$$

$$L_{loop} = L_{dc+} + L_{dc-} + L_{mid} + L_t + L_b + L_{dc} - 2L_{12} - 2L_{23} + 2L_{13} \quad (2\text{-}7)$$

For the mutual inductances, L_{12} is between dc+ and dc– traces, L_{23} is between dc– and middle traces, and L_{13} is between dc+ and middle traces. It can be seen from (2-3) that the frequency of resonant point in the noise prorogation path is determined by the loop parasitic inductance and the device output capacitance. The damping factor is determined by loop inductance, loop AC resistance and device output capacitance. Larger AC resistance in the circuit can be helpful to reduce the resonant peak.

The parasitic inductance of the PCB track is obtained through Maxwell Q3D extractor. Fig. 2.13 shows the PCB layout for noise path identification. To get the appropriate inductance value, it is important to determine the current source and current sink when setting up the source condition for Maxwell Q3D extractor. In the chopper circuit, the high frequency current distribution determines the EMI propagation path, not the DC current distribution. Hence, the connection points of the output filter don't have an effect on the EMI path. For example, if the connecting point of the filter inductor changes from A to G or from B to H, the EMI path doesn't change because the high frequency current flows from C $\rightarrow$ A $\rightarrow$ B $\rightarrow$ D $\rightarrow$ E $\rightarrow$ F. Therefore, the source setup in Maxwell Q3D extractor is that C is source 1, A is sink 1, B is source 2 , D is sink 2, E is source 3 and F is sink 3. Table 2.1 lists the extracted inductance and resistance under dc and 100 MHz ac conditions. It can be seen that the parasitic inductance changes very slightly from dc to 100 MHz, therefore, the dc inductance can be used for the high frequency model.

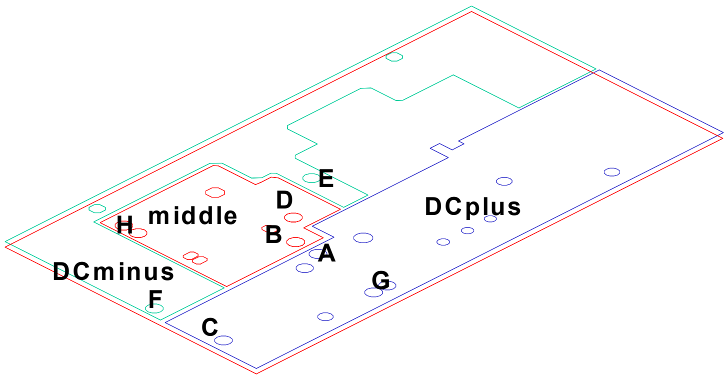

Fig. 2.13 Noise current path identification.

Table 2.1 Extracted dc and 100 MHz ac inductance and resistance

Inductance (H)	Dc			ac at 100 MHz		
	dc-plus	ground	m-trace	dc-plus	ground	m-trace
dc-plus	1.09E-08	3.98E-09	0.63E-09	1.15E-08	4.25E-09	0.79E-09
ground	3.98E-09	4.58E-08	1.96E-09	4.25E-09	4.58E-08	1.23E-09
m-trace	0.63E-09	1.96E-09	2.04E-09	0.79E-09	1.23E-09	1.99E-09

Resistance (Ω)	Dc			ac at 100 MHz		
	dc-plus	ground	m-trace	dc-plus	ground	m-trace
dc-plus	0.0083622	0	0	0.0057891	-0.00119958	0.000155485
ground	0	0.049333	0	-0.00119958	0.0329965	0.000556008
m-trace	0	0	0.007898	0.000155485	0.000556008	0.00357013

The dc bus capacitor was measured with L_{dc} = 2 nH, R_{dc} = 30 mΩ, C_{dc}=1 mF. The device output capacitance is C_{ds} = 0.9 nF. The lead inductance of deice and diode can be obtained using MaxwellQ3D as well, L_b=L_t=4 nH. Since all the parasitic components are known, we can calculate the loop inductance using (2-7), which is about 58 nH. The derived propagation path transfer function is plotted by the Mathcad, as shown in Fig.

2.14. It can be seen that there is resonant point occurring at 22 MHz, which is determined by the loop inductance and the parasitic output capacitance of the device.

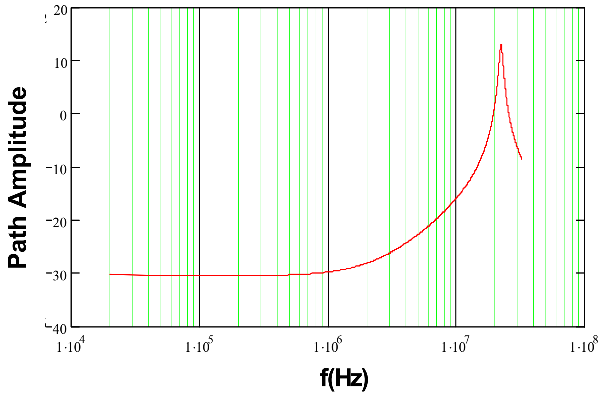

Fig. 2.14 Propagation path transfer function

2.1.4 Gate resistance effect on current rising time,

The current rising time and falling time can be calculated according to the gate drive circuit and operating condition. An equivalent circuit including parasitic inductance and the parasitic capacitance was presented in [67] to calculate the current rising speed of voltage-driven device during turn-on. Fig. 2.15 shows the equivalent circuit.

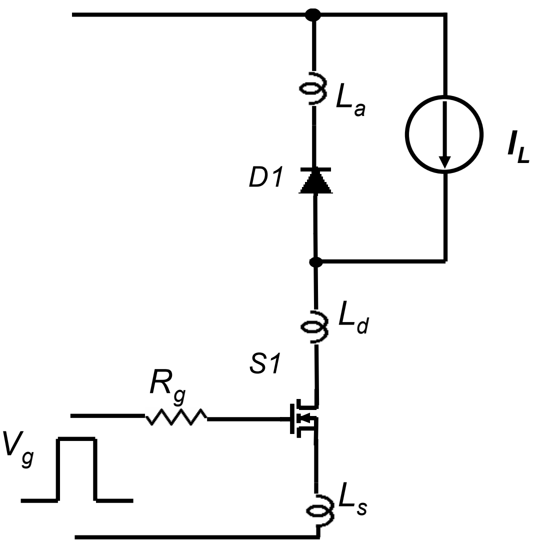

Fig. 2.15 Gate resistance effect during device switching

The current rising speed can be calculated by

$$\frac{di}{dt}_{on} \approx g_m \frac{V_g - V_{gs}}{C_{iss}R_{gon} + g_m L_s} \approx g_m \frac{V_g - V_{th}}{C_{iss}R_{gon} + g_m L_s} \tag{2-8}$$

It shows that the current rising speed is determined by gate-source voltage, threshold voltage, device input capacitance, transconductance, lead inductance and gate resistance. If all the values are fixed except the gate resistance, the current rising speed will be determined by gate resistance. The smaller the gate resistance is, the faster the current rising speed. The current rising time is determined by load current and the current rising speed as given in (2-9).

$$\tau_r = \frac{I_L}{\frac{di}{dt}_{on}} \tag{2-9}$$

2.1.5 Experimental verification of DM modeling

To verify the proposed modeling method, the hardware test and time domain simulation are performed. The chopper specifications are:

Input voltage: 42V

Output voltage: 14V

Output power: 100W

Switching frequency: 20kHz

Major devices and components are (1) MOSFET: HUFA76645P3, (2) Freewheeling diode: 12CTQ045, (3) Input capacitor C_{dc}: 1000uF, (4) output capacitor: 470uF, and (5) output inductor: 420 uH.

Fig. 2.16 shows the experimental switching waveform with the different gate resistance and it indicates the turn-off ringing is about 24 MHz that is caused by the oscillation between the loop inductance and parasitic capacitance of the MOSFET. The switching speed reduces as the increase of the gate resistance, for instance, current fall time increase from 30ns with 10Ω gate resistance to 70ns with 100Ω gate resistance.

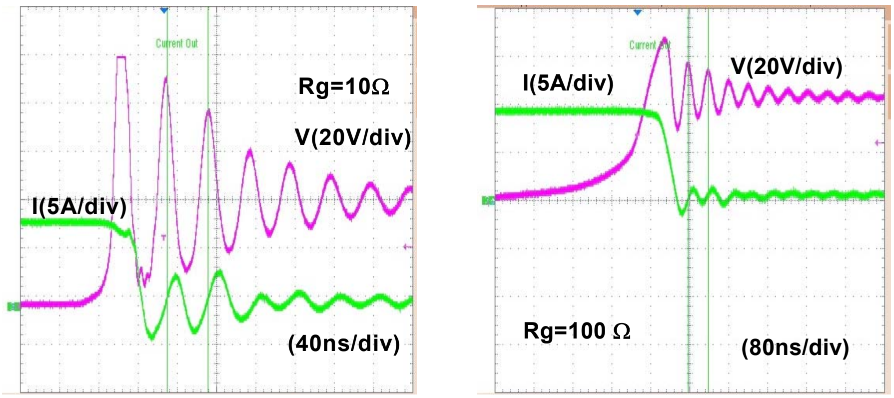

Fig. 2.16 Switching waveform with different gate resistance

The DM noise spectrum can then be calculated by multiplying (2-1) and (2-3), and Fig. 2.17 shows the calculated result of DM noise spectrum with different switching speed. The above frequency domain EMI prediction results can be verified with the experimental result and the conventional time domain simulation result.

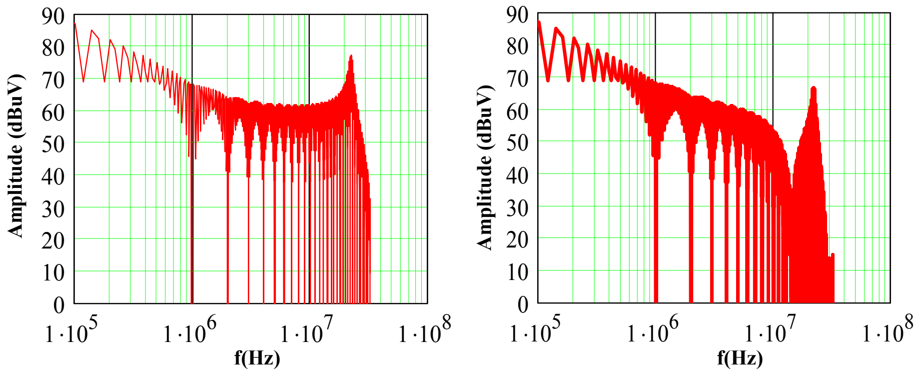

Fig. 2.17 Calculated DM noise spectrum (a) t_r=30ns (b) t_r=70ns

The DM noise spectrum from time domain simulation followed by FFT analysis and the experimental results are given in Fig. 2.18. Both results well match with the frequency-domain prediction. They also indicate that with the larger gate resistance the peak of the noise spectrum will be smaller.

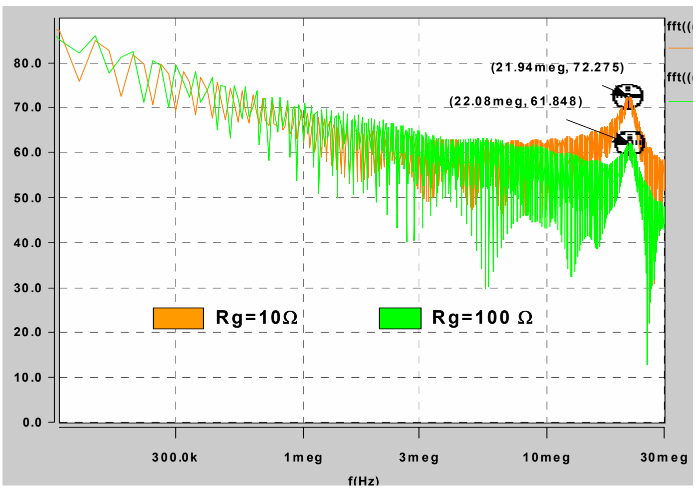

(a)

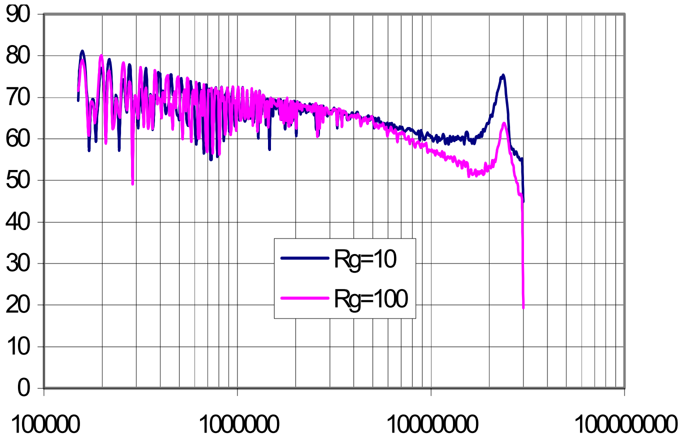

Fig. 2.18 Simulated and experimental spectrum (a) spectrum from time domain simulation followed by FFT of Saber (b) Experimental result

2.2 DM Case Study-Adding high frequency capacitor snubber

To further study the DM frequency domain modeling and prediction of the chopper circuit, another case was considered. It is a common practice to put high frequency capacitor across the dc bus as snubber to suppress the voltage spike across the device during MOSFET turn-off. In addition, the capacitor is required to put as near the switching device as possible as shown in Fig. 2.19. However, the addition of such snubber will have an effect on the DM noise spectrum because it changes the noise propagation path, which can be demonstrated by the frequency domain modeling and prediction method.

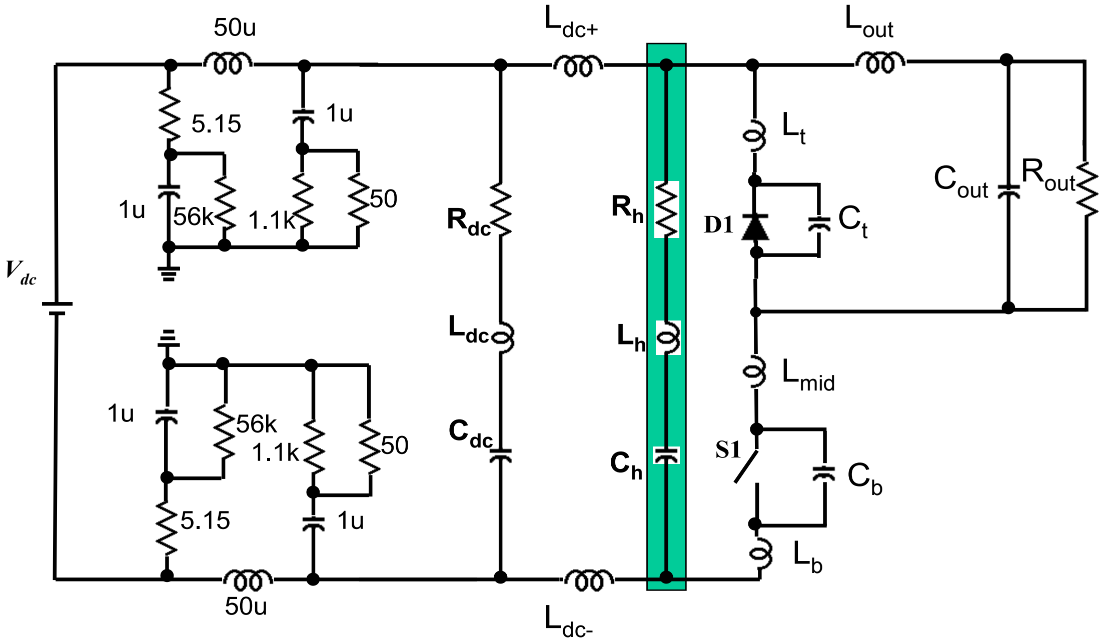

Fig. 2.19 Chopper circuit with the added high frequency capacitor

The frequency domain equivalent circuit of chopper is shown in Fig. 2.20 with the addition of the high frequency capacitor. Although the noise source is still a current source with the same expression as (2-1), the noise path changes significantly by adding the capacitor. Therefore the noise spectrum will change because of the resonance between the dc bus parasitic inductances and added capacitor.

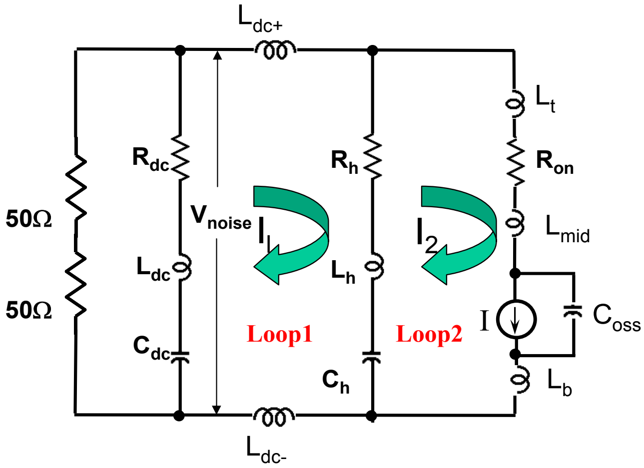

Fig. 2.20 Frequency domain circuit with high frequency capacitor

By solving the two current loop equations, the relation between I and I_1 can obtained as

$$F_1(s) = \frac{I_1(s)}{I(s)} \cong \frac{1 + \frac{s}{Q_z\omega_z} + (\frac{s}{\omega_z})^2}{1 + \frac{s}{Q_0\omega_0} + (\frac{s}{\omega_0})^2} \tag{2-9}$$

The relation between V_{noise} and I_1 can be derived as

$$Z_2(s) = \frac{V_{noise}(s)}{I_1(s)} = -\frac{R_{dc} + sL_{dc} + \frac{1}{sC_{dc}}}{100 + (R_{dc} + sL_{dc} + \frac{1}{sC_{dc}})}100 \tag{2-10}$$

Therefore, the noise propagation path transfer function is

$$Z(s) = \frac{V_{noise}(s)}{I(s)} = F_1(s)Z_2(s) \cong -\frac{1 + \frac{s}{Q_z\omega_z} + (\frac{s}{\omega_z})^2}{1 + \frac{s}{Q_0\omega_0} + (\frac{s}{\omega_0})^2} \cdot \frac{R_{dc} + sL_{dc} + \frac{1}{sC_{dc}}}{100 + (R_{dc} + sL_{dc} + \frac{1}{sC_{dc}})}100 \tag{2-11}$$

where: $\omega_0 = \frac{1}{\sqrt{L_0C_h}}, Q_0 = (\frac{1}{R + R_h})\sqrt{\frac{L_0}{C_h}}$,

$\omega_z = \frac{1}{\sqrt{L_zC_h}}, Q_z = \frac{1}{R_h}\sqrt{\frac{L_z}{C_h}}$,

$R = R_{dc} + R_{dcplus} + R_{dc\min us}$,

$L_0 = L_{dcplus} + L_{dc\min us} + L_{dc} + L_h - 2L_{12}$,

$L_z = L_h - 2L_{13} + 2L_{23}$.

(2-11) indicates that there is a pair of resonant poles caused by the high frequency capacitor and the parasitic inductance of dc-plus track and dc-minus track in the noise propagation path. The quality factor Q_0 is mainly determined by the capacitor value provided that the ESR and ESL value vary slightly. There is also a pair of high frequency zeros mainly caused by the self-resonation of the high frequency capacitor. To further explain this, three high frequency capacitors with different values are selected and the impedances of these capacitors are plotted in Fig. 2.21. Their capacitance value and measured ESR and ESL are shown in Table 2.2.

Table 2.2 Measured high frequency capacitor values

C_h	333.7nF	64nF	10nF
L_h	8.24nH	9.65nH	15nH
R_h	17.47mΩ	21mΩ	43mΩ

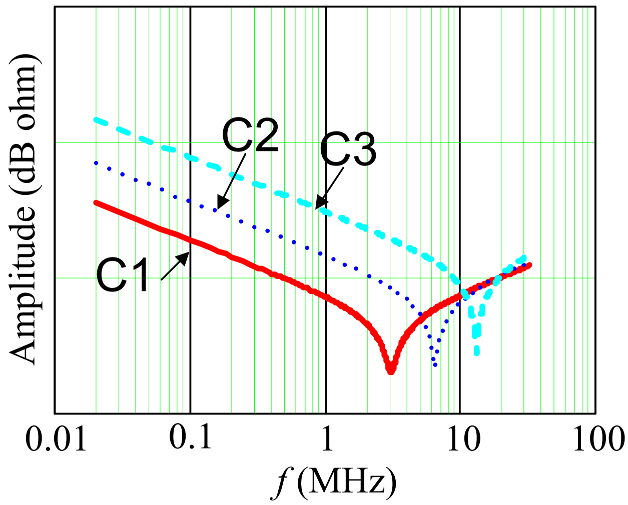

Fig. 2.21 High frequency capacitor amplitude plot

Fig. 2.22 compares the frequency-domain prediction and experimental results. Fig. 2.19(a) gives the plot of noise propagation path with different capacitors. It can be seen that the resonant pole moves to a higher frequency as the capacitance decreases, and the resonant peaks also increase. The DM noise spectrum can be calculated by multiplying (2-1) and (2-6). Fig. 19(b) shows the calculated result of DM noise spectrum with different capacitor. The results illustrate that the resonant points of the noise propagation path determine the location of the peak of the EMI spectrum. Fig. 19(c) shows the experimental spectrum with different capacitors. The first resonant peak points well match with the frequency-domain prediction.

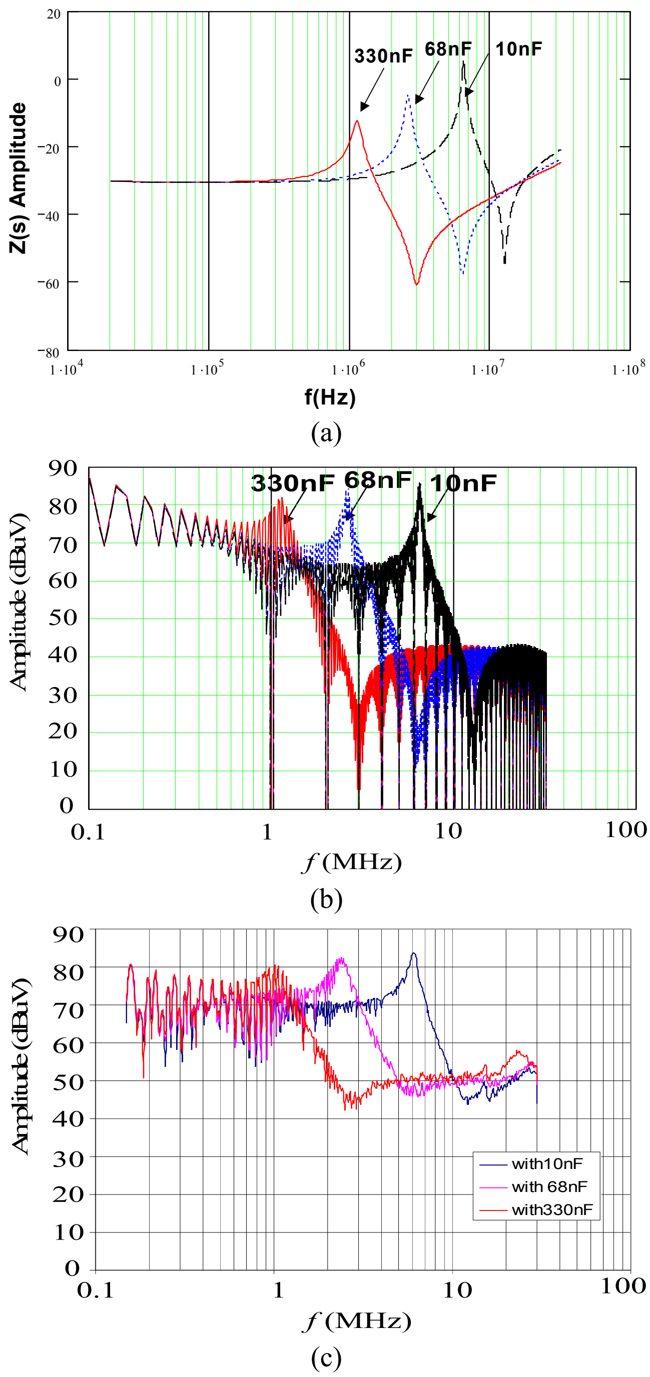

Fig. 2.22 Comparison of simulation and experimental results: (a) propagation path impedance; (b) calculated frequency spectrum with different capacitors; and (c) experimental results

2.3 Common mode modeling and prediction

CM mode noise is mainly conducted through parasitic capacitance between component and ground plane. It is excited by the common mode voltage, which is source voltage of the top device or drain voltage of the bottom device in a phase leg. The single phase chopper is still used as an example to illustrate how to apply frequency domain approach to modeling and simulate common mode noise.

Fig. 2.23 shows the chopper circuit configuration with three parasitic capacitors C_{L1gnd}, C_{L2gnd}, and C_{mgnd}, circled to represent the major CM noise path. The voltage amplitude variation on these capacitances is larger than those on other capacitance such as, dc bus to ground plane capacitance. The sum of these three parasitic capacitances is defined as Cp, which is the dominant element in the noise propagation path. Note that the output capacitor C_0 can be regarded as short circuit at high frequency. The common mode voltage is the drain voltage of the bottom device S_4.

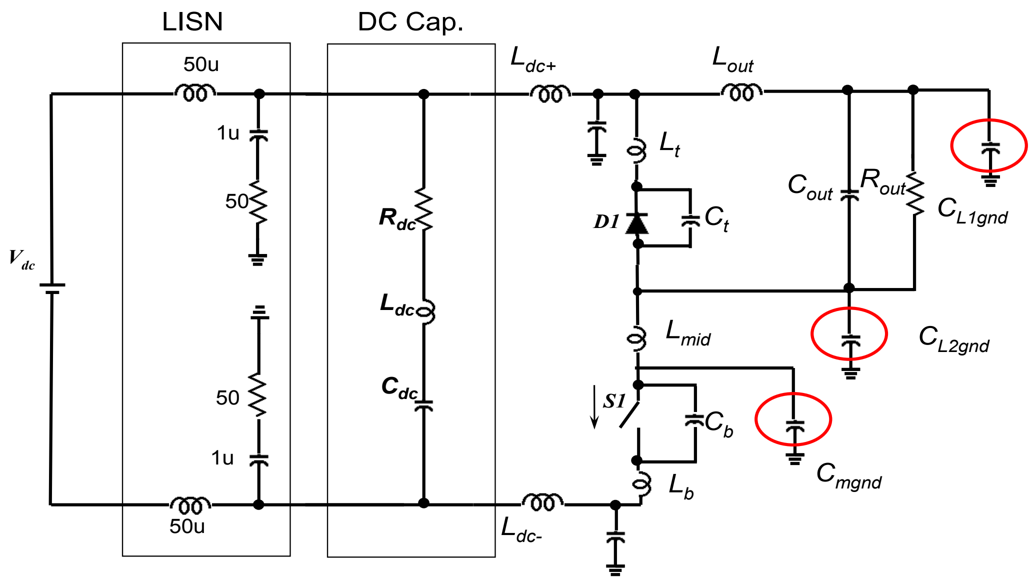

Fig. 2.23. Common mode circuit configuration for a part of the inverter.

2.3.1 Conventional method of CM EMI prediction for single phase chopper

Fig 2.24 shows the conventional common mode proposed by Nave. In this conventional model CM noise flows through both positive and negative buses symmetrically, switching dv/dt is the major source of CM noise, and parasitic capacitance *Cp* is the major propagation path, both treated as constant.

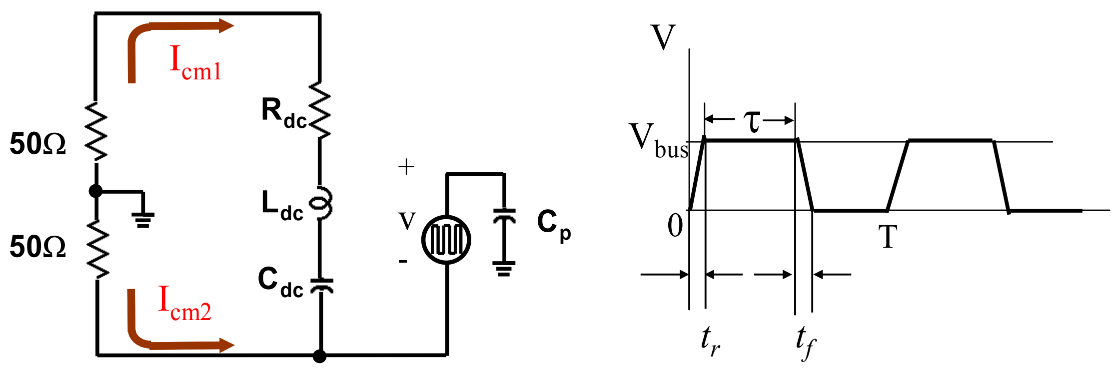

Fig. 2.24 Conventional Common mode model

The switching noise source can be considered as a trapezoidal pulse train. To simplify analysis, it is assumed that $t_r = t_f$. The frequency domain representation of the CM voltage source can then be expressed in (2-12).

$$V_n = 2V_{dc}(1-d)\frac{\sin(n\pi(1-d))}{n\pi(1-d)}\frac{\sin({n\pi t_f}/{T})}{{n\pi t_f}/{T}}\ell^{-j\frac{n\pi(\tau+t_f)}{T}} \tag{2-12}$$

In the above expressions, d is the duty cycle of the bottom device, T is the inverter switching period, V_{dc} is the dc bus voltage, τ is the off time of the switch and n is the harmonic order.

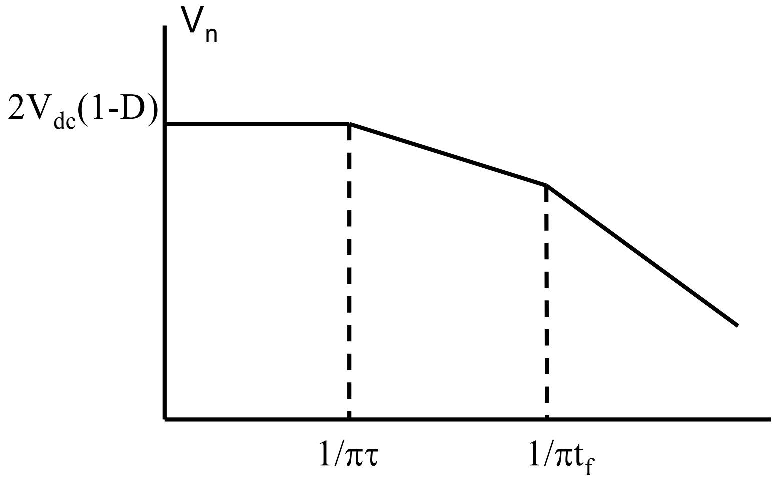

Fig. 2.25 Envelop of the amplitude of spectrum of CM voltage source

Fig. 2.25 shows envelop of the amplitude spectrum of CM source voltage. It can be seen that envelop of the spectra follows three asymptotes and two corner frequency. The first asymptote has a slope of 0 dB/decade and the second asymptote has a slope of -20 dB/decade. The first corner frequency is at $1/\pi\tau$. The third asymptote has a slope of -40 dB/decade in the high frequency region and the second corner frequency is at $1/\pi t_f$., which is attributed to the switching period and fall time. A slower switching speed means larger t_f, which subsequently yields a lower cut-off frequency or less noise in high frequency range.

The transfer function of noise propagation path of conventional model is given in (2-13) and its plot is shown in Fig. 2.26.

$$Z(s) = \frac{V_{noise}(s)}{V_n} = \frac{25}{25 + \dfrac{1}{sCp}} \tag{2-13}$$

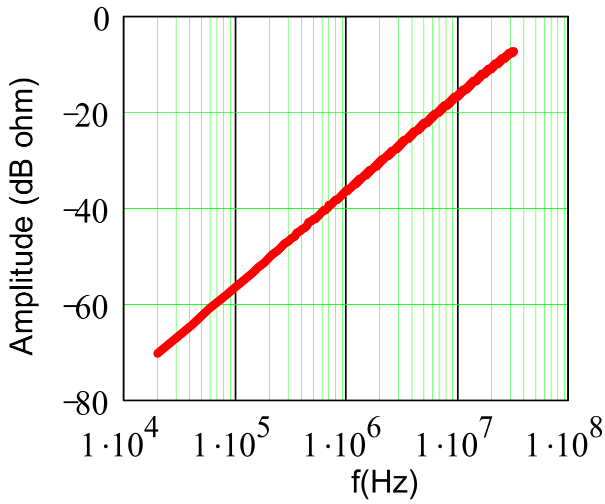

Fig. 2.26 Plot of noise propagation path transfer function

Multiplying (2-12) and (2-13), the CM noise voltage observed at LISN can be calculated by (2-14)

$$V_{cmnoise}(f) = V(f) \cdot Z(f) \tag{2-14}$$

Fig. 2.27 shows that the prediction result based on the conventional mode. It can be seen that the CM spectra envelop is a flat pedestal up to MHz range. This is due to that the -20dB/decade slope of noise source is offset by the 20 dB/decade slope of noise path. In addition, the CM EMI spectrums are almost the same up to about 10 MHz under different switching speed.

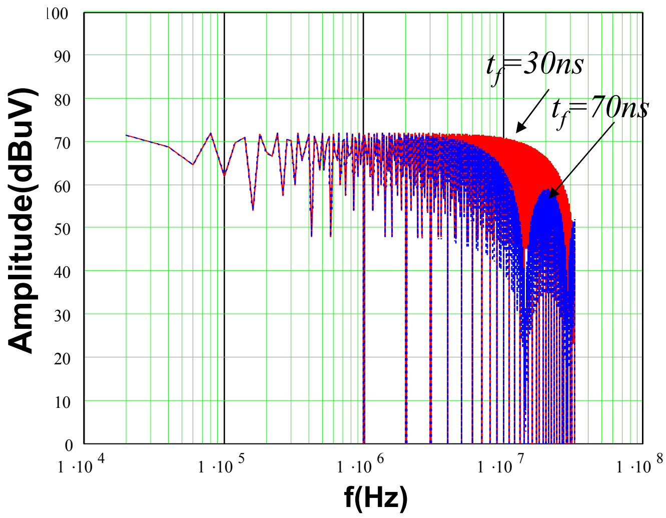

Fig. 2.27 Predicted result based on conventional model

2.3.2 Proposed CM Noise Source Modeling

The limitation of the conventional model is that the voltage source description is so simple that it doesn't include voltage overshoot and undershoot. Both of them are the CM noise source at high frequency and related to circuit parasitics because it is determined the resonance between the loop inductance and device parasitic capacitance. Fig. 2.28 shows decomposition waveform of the switching voltage. The switching voltage can be divided into two parts, one part is the same of the conventional model that is trapezoidal from, the other part is parasitic ringing determined by the resonation between the parasitic inductance and device output capacitance.

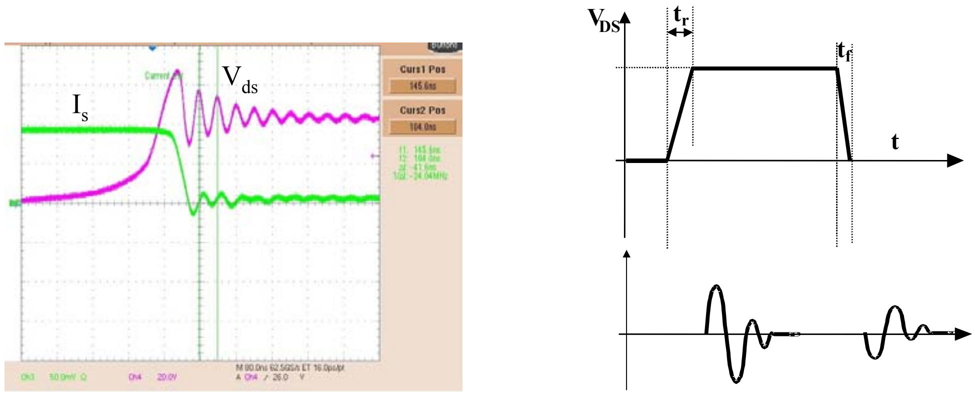

Fig. 2.28 Device voltage decomposition waveform

Using the decomposition waveform, the proposed CM model includes two noise sources, one is trapezoidal voltage switching waveform, and the other is parasitic ringing on the voltage waveform. The trapezoidal waveform is the same as the conventional model. The parasitic ringing on the voltage waveform is excited during switching action. Because both device voltage and current changes during switching transient, they all could be the excitation source. Fig. 2.29 shows the CM high frequency equivalent circuit during switching transient if the excitation source is the device switching current. The frequency domain expression of the parasitic ringing voltage across C_p can be calculated based on these equivalent circuits.

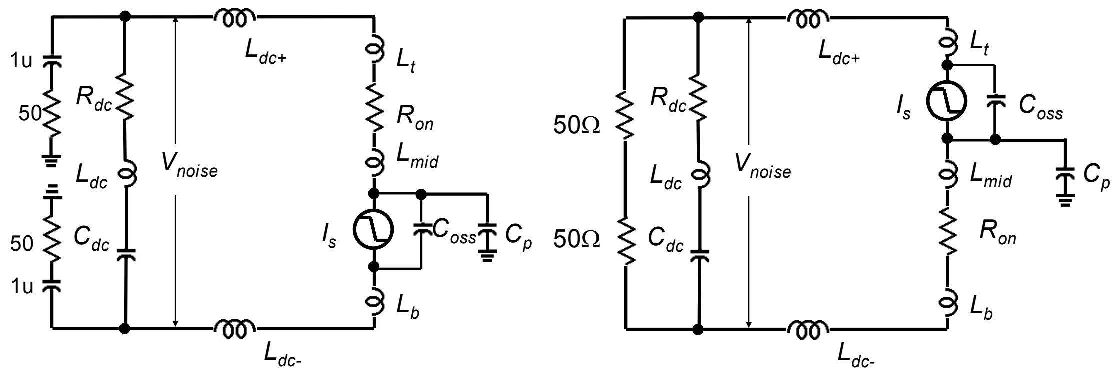

Fig. 2.29 CM high frequency equivalent circuits during switching transient-current source (a) during bottom device turn off (b) during top device turn off

Usually $C_{oss} >> C_p$, therefore the parasitic ringing is caused by the resonation between loop parasitic inductance and device output capacitance. Furthermore, these two equivalent circuits can be synthesized to a unified circuit if $L_{dc+} \approx L_{dc-}$ and $L_b \approx L_t$. Fig. 2.30 shows the proposed CM noise equivalent circuit, which is the combination of two noise sources. V_n is the same as conventional model in (2-12) that accounts for the CM noise up to MHz range, while I_c is the current source that creates another high frequency voltage noise source responsible for CM noise up to tens of MHz range.

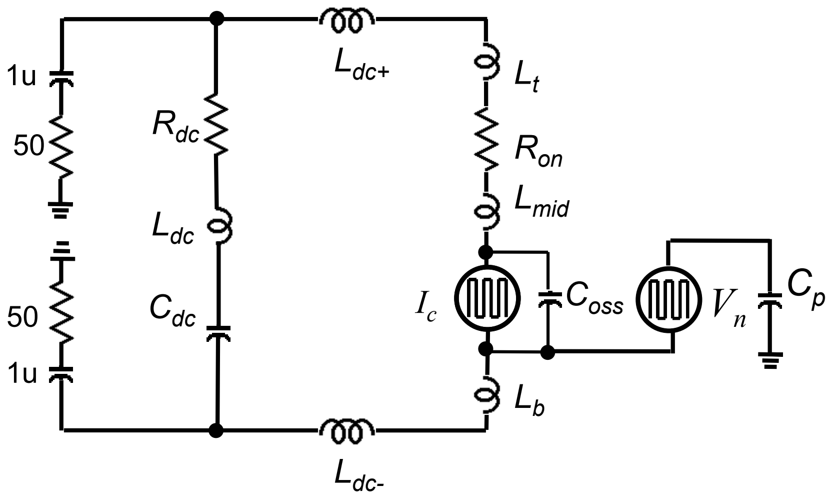

Fig. 2.30 CM noise equivalent circuit in frequency domain.

The frequency domain expression of the high frequency voltage ringing across Cp can be calculated $v_r(f)$,

$$v_r(f) \cong I_c(f) \frac{1}{1+\frac{s}{Q\omega_0}+(\frac{s}{\omega_0})^2} \cdot (sL_{dc-} + sL_b - \frac{sL_{dc}}{2}) \qquad (2\text{-}15)$$

where, $\omega_0 = \frac{1}{\sqrt{L_{loop}C_{oss}}}$, $Q = \frac{1}{R}\sqrt{\frac{L_{loop}}{C_{oss}}}$ and L_{loop} is given in (2-7). $I_c(f)$ is given in (2-1) that is the same as DM noise current representations

If the excitation source is device switching voltage, the CM high frequency equivalent circuit during switching transient is given in Fig. 2.31. The voltage source is the step voltage source with finite rising time as shown in Fig. 2.32.

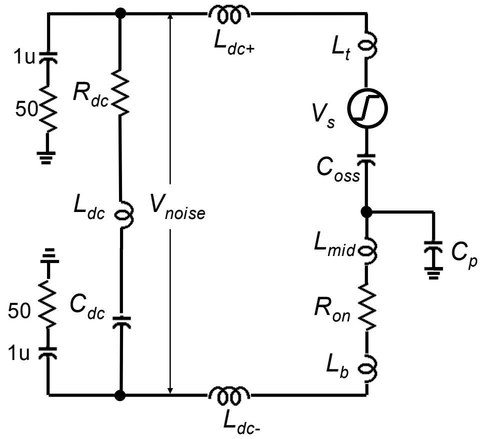

Fig. 2.31 CM high frequency equivalent circuits during switching transient-voltage source (a) during top device turn off (b) during bottom device turn off

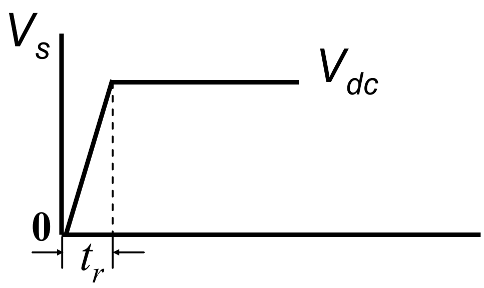

Fig. 2.32 The step voltage with finite rising time

$v_{r+}(f)$ is the ringing voltage when the top device turns off, which is given in ,

$$v_{r+}(f) = V_s(f)\frac{sCoss}{1+\frac{s}{Q\omega_0}+(\frac{s}{\omega_0})^2}\cdot(sL_{dc-}+sL_b-\frac{sL_{dc}}{2}) \qquad (2\text{-}16)$$

Here, $V_s(f)$ is the frequency domain expression of the step voltage.

$v_{r-}(f)$ is the ringing voltage when bottom top device turns off . Its expression is given in (2-17) if $L_{dc+} \approx L_{dc-}$ and $L_b \approx L_t$.

$$v_{r-}(f) = V_s(f)\frac{sCoss}{1+\frac{s}{Q\omega_0}+(\frac{s}{\omega_0})^2}\cdot(\frac{sL_{dc}}{2} - sL_{dc-} + sL_b -)e^{-s\tau} \quad (2\text{-}17)$$

Here, τ is the time delay between two transient.

To calculate the ringing voltage during a switching period, the ringing voltages caused by two switching transient have to be combined.

$$v_r(f) = v_{r+}(f) + v_{r-}(f) = V_s(f)\frac{sCoss}{1+\frac{s}{Q\omega_0}+(\frac{s}{\omega_0})^2}\cdot(sL_{dc-} + sL_b - \frac{sL_{dc}}{2}))(1-e^{-s\tau}) \quad (2\text{-}18)$$

The amplitude of the term $(1-e^{-s\tau})$ is shown in Fig. 2.33. It shows that it has a flat envelop of 2 in the high frequency range. It can be considered as the worst case, where the phase angles of v_{r+}(f) and *$v_{r-}(f)$* are the same.

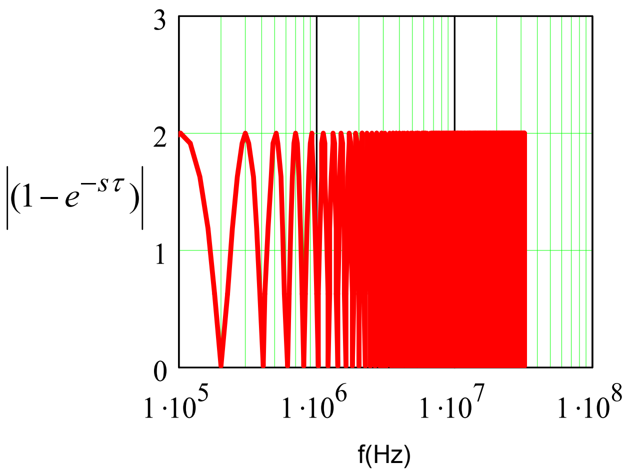

Fig. 2.33 The amplitude of term $(1-e^{-s\tau})$

Therefore, if the worst case is taken into account, (2-18) can be simplified as

$$v_r(f) = 2V_s(f)\frac{sCoss}{1+\frac{s}{Q\omega_0}+(\frac{s}{\omega_0})^2}\cdot(sL_{dc-}+sL_b-\frac{sL_{dc}}{2})) \tag{2-19}$$

Whether to use current source or voltage source as excitation source for parasitic ringing depends on converter operating conditions such as dc bus voltage and load current. The criteria to use voltage source is given in (2-20), otherwise, the current source should be used.

$$V_{dc} > \left|\frac{I_L}{sC_{oss}}\right| \tag{2-20}$$

According to the frequency-domain equivalent circuit, the CM noise voltage at the LISN can be calculated as the result of two noise sources multiplied with the propagation path, as given in (2-21).

$$V_{cmnoise}(f) \cong (V_n(f)+v_r(f))\cdot\frac{25}{25+\frac{1}{sC_p}} \tag{2-21}$$

The total noise observed at LISN can be calculated after the CM EMI spectrum is available. It is given in

$$V_{tota\ln oise}(f) = V_{cmnoise}(f)+V_{dmnoise}(f) \tag{2-22}$$

2.3.3 Parasitic capacitance calculation

The three parasitic capacitors that are considered the main CM noise paths are effectively in parallel and can be lumped together as a single parasitic capacitor, C_p. In the actual experimental setup, two CM path capacitances are formed between the cable and the ground plane, as shown in Fig. 2.34. With cable radius *r*, and the distance in between the ground plane *h*, the capacitance C_0 can be solved in a closed-form solution, as shown in (2-23).

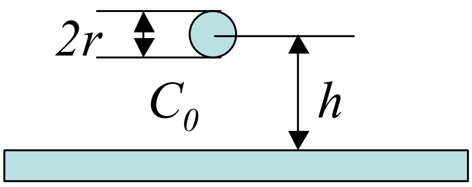

Fig. 2.34 CM path formed between cable and the ground plane.

$$C_0 = \frac{24.2\varepsilon}{\log\left[(h/r)+\sqrt{(h/r^2)-1}\right]} \quad \text{(pF/m)} \qquad (2\text{-}23)$$

The calculated CM path parasitic capacitances are: C_{L1gnd} = 38 pF, C_{L2gnd} = 25 pF. Given the parasitic capacitance between the device and heat sink ground, the total CM parasitic capacitance can be found as $C_{pa} = C_{mgnd} + C_{L1gnd} + C_{L2gnd}$ = 85 pF.

2.3.4 CM Experimental Verification

The resulting frequency-domain analysis spectra for different switching times are shown in Fig. 2.35. The load current is 8A and the switching current is used as the excitation source for high frequency ringing. The equivalent circuit shown in Fig. 2.30 is used for calculation. Again, the same circuit CM performance was then verified with hardware experiment. The results are shown in Fig. 2.36. The experimental result agrees with the frequency-domain simulation result very well. The predicted total EMI spectrum and the experimental result of total EMI spectrum are presented in Fig. 2.37. The predicted result matches well with the experimental result. The frequency-domain approach is again proven to be effective for EMI performance prediction.

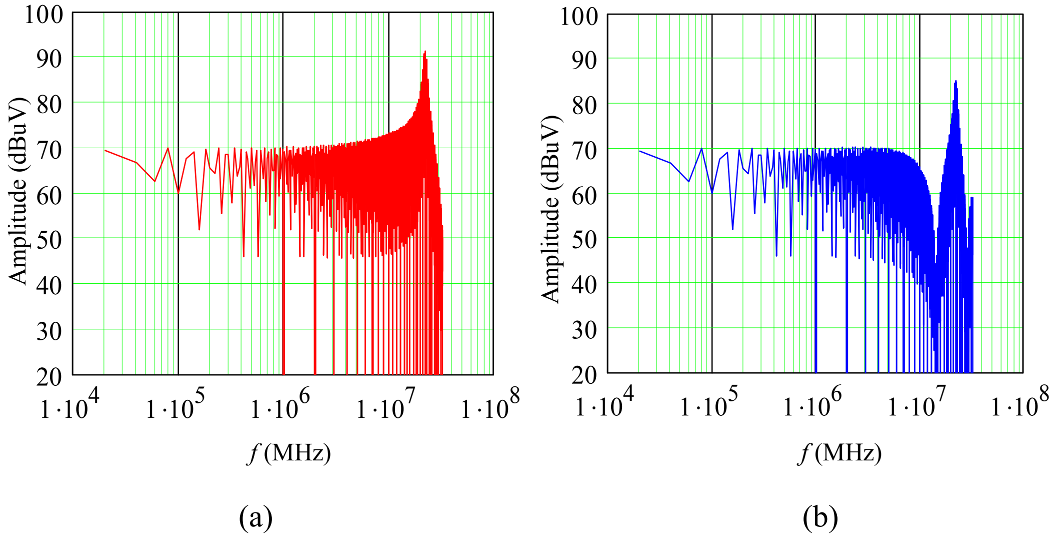

Fig. 2.35 Calculated DM noise spectra (a) t_r=30ns (b) t_r=70ns

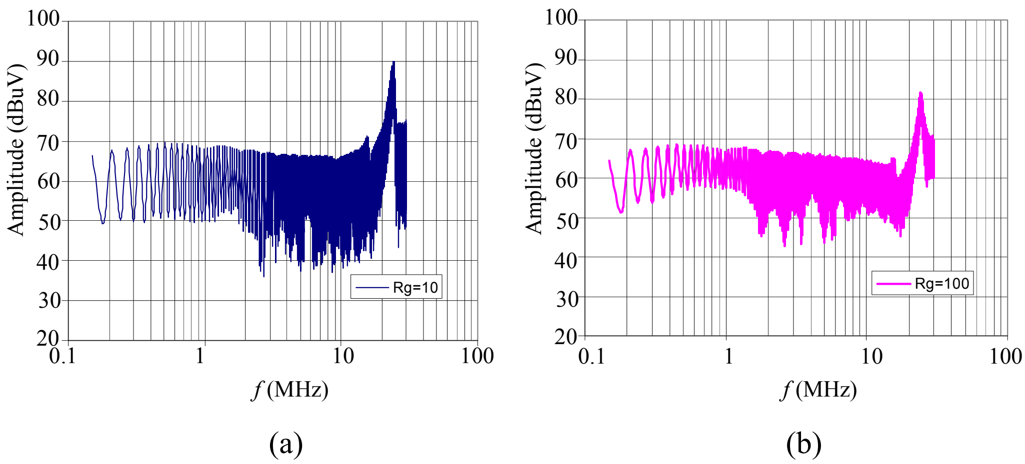

Fig. 2.36 Experimental result of CM noise spectra obtained with different gate resistance

(a) R_g=10 (b).R_g=100

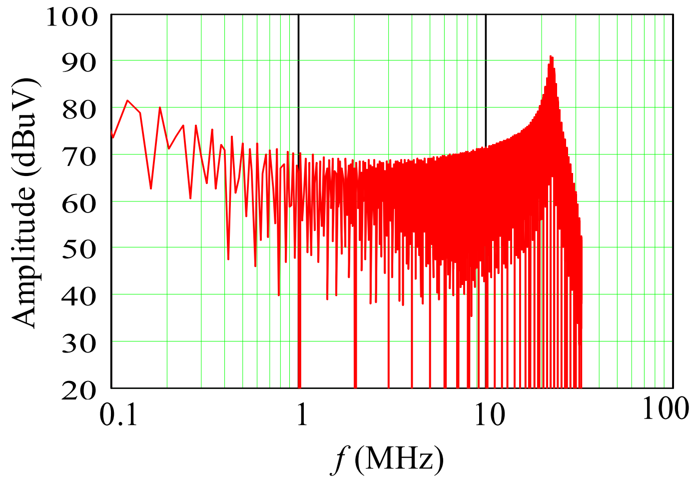

(a)

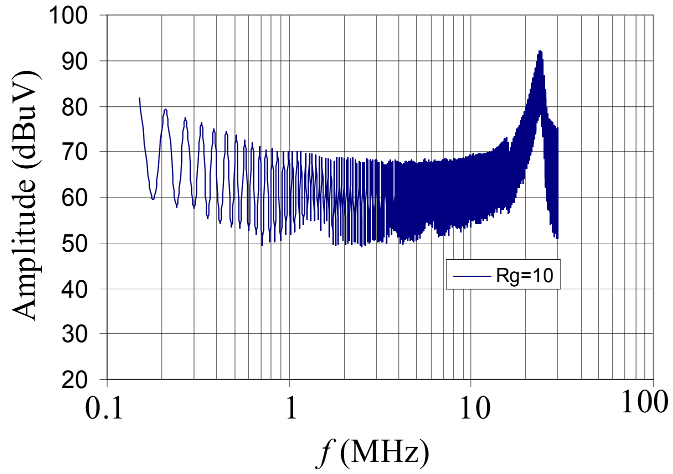

(b)

Fig. 2.37 Total noise spectra obtained with different methods; (a) frequency-domain approach (b) experimental result.

2.4 CM Case study- Adding high frequency capacitor snubber

The effect of adding high frequency capacitor across the bus on the DM EMI was presented in the previous section. It is interesting to investigate its effect on CM EMI spectrum. Since such kind of snubber will suppress the voltage spike across the device during device turn-off, it will change CM EMI spectrum in high frequency range. This effect can be demonstrated by the frequency domain modeling and prediction method. Fig. 2.38 shows the common mode circuit configuration after adding the high frequency circuit across the dc bus.

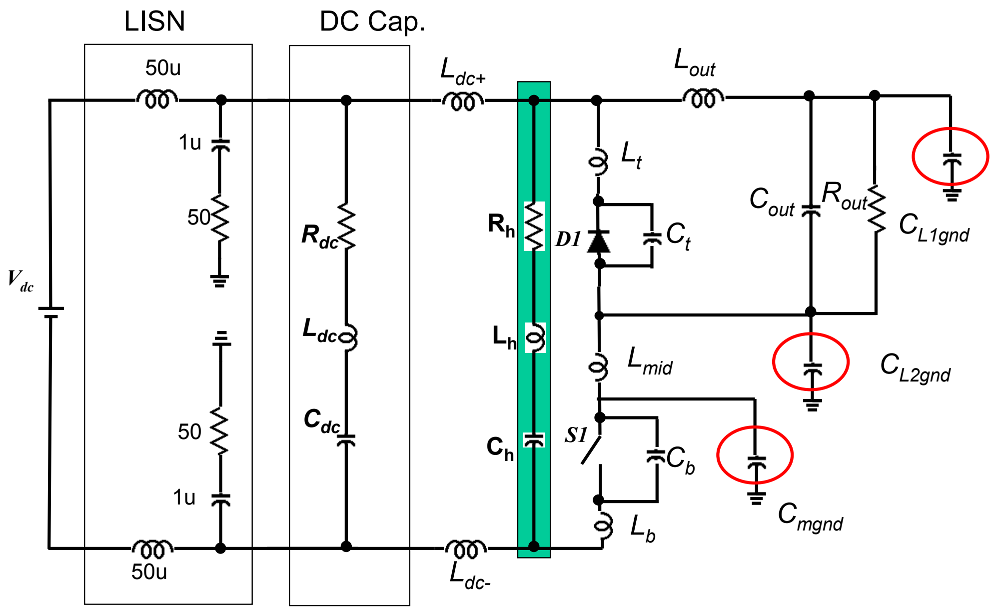

Fig. 2.38 Common mode circuit configuration with the added high frequency capacitor

Fig. 2.39 shows the CM frequency domain equivalent circuit with the addition of the high frequency capacitor. Although the current source and voltage source are still with the same expression as (2-1) and (2-13), the noise path in high frequency range changes significantly by adding the capacitor.

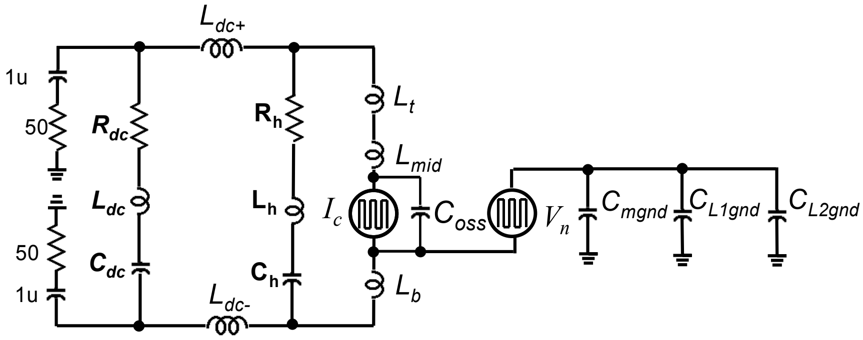

Fig. 2.39 CM frequency domain equivalent circuit with high frequency capacitor

The frequency domain expression of the high frequency voltage across the parasitic capacitance can be calculated based on the equivalent circuit,

$$v_r(f) \cong I_c(f)\frac{1+\dfrac{s}{Q_z\omega_z}+(\dfrac{s}{\omega_z})^2}{1+\dfrac{s}{Q_0\omega_0}+(\dfrac{s}{\omega_0})^2}\cdot(sL_{dc-}+sL_b-\frac{sL_{dc}}{2}) \tag{2-24}$$

The expression of Q_z, ω_z, Q_0 and ω_z are the same as given in (2-11). The CM EMI under the effect of two sources can be calculated using (2-21). The high frequency capacitance value and measured ESR and ESL are: C_h=330 nF, L_h=8 nH, R_h=18 mΩ.

Fig. 2.40 compares the frequency-domain prediction and experimental results of the EMI spectrum. The experimental result agrees well with the result from the frequency domain prediction. Compared with CM EMI spectrum shown in Fig.2.34, the high frequency peak around 22 MHz disappears. This is due to that the high frequency capacitor provides a path for the high frequency current, which decouples the devices lead inductance and dc bus parasitic inductance. Fig. 2.41 shows the predicted and experimental results of the total EMI spectrum after adding the capacitor. The predicted result matches well with hardware experimental result. The peak around 1 MHz is a result of DM EMI. It is caused by the resonant between the added capacitor and dc bus parasitic capacitance. In high frequency ranges, the CM EMI becomes dominant.

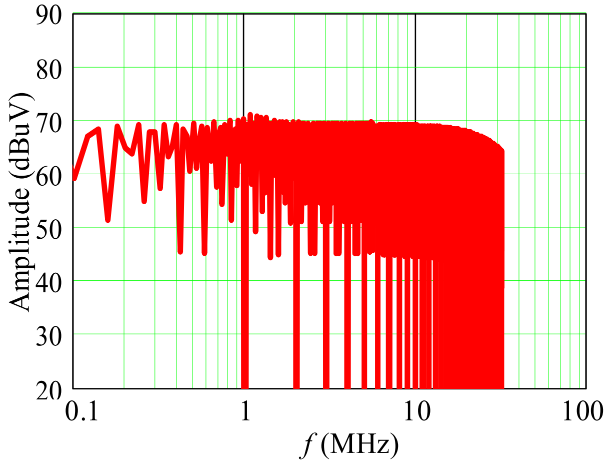

(a)

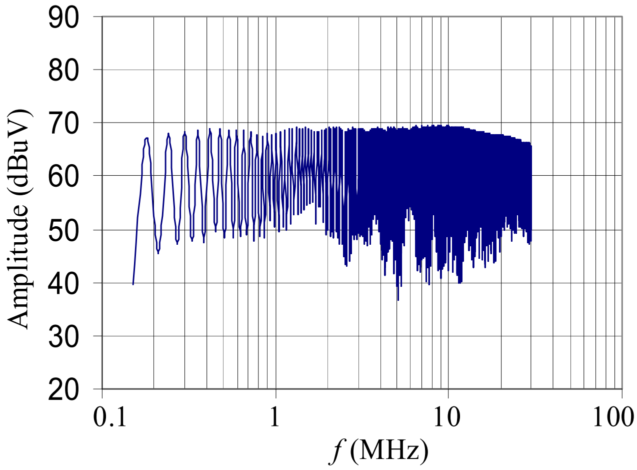

(b)

Fig. 2.40 CM EMI spectrum with added capacitor (a) calculated result (b) experimental results

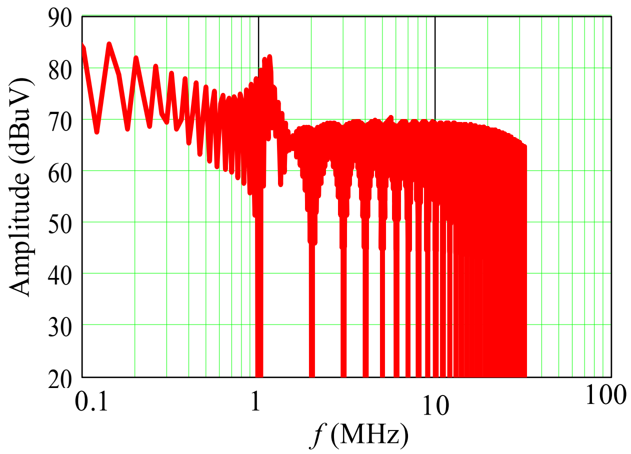

(a)

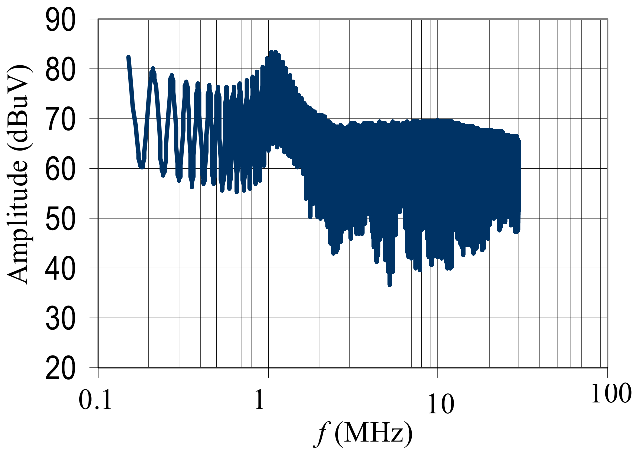

(b)

Fig. 2.41 Total EMI Spectrum with added capacitor (a) calculated result (b) experimental results

2.5 Summary

This chapter proposes the concept of the "frequency-domain" analysis to predict EMI spectrum for inverter circuit. A partial of inverter phase leg, single phase chopper circuit was used as studied circuit. High frequency equivalent circuit for both CM EMI and DM EMI are proposed. Through these high frequency circuits, the noise source and the noise path can be derived in close form. Using accurate noise source and path models, the proposed method avoids the computational problems in the conventional “time-domain” analysis and effectively predicts the EMI performance. The predicted results match well with the experimental result. Adding high frequency capacitor will change the noise propagation path of DM EMI and change the CM noise source in high frequency region significantly, thus producing different spectrum for both CM EMI noise and DM EMI noise. Its impact was effectively evaluated through frequency domain analysis and hardware experiments.

Chapter 3 DM EMI Modeling and Prediction- three phase inverter

With complexity of circuits and control methods, the electromagnetic interference (EMI) produced in a three-phase inverter is much more difficult to predict than in a dc/dc converter. Much of past research was focusing on the EMI impact to the motor and compatibility issue, but not on the inverter itself, which is indeed the major source of EMI in the entire motor drive system. Unlike dc/dc converters, motor drive inverters is very difficult to reach the steady-state operating condition in time domain simulation due to the huge difference between simulation step (nano seconds) and fundamental cycle (mili seconds) and most likely the simulation also has convergence problems. Frequency domain EMI analysis and modeling for three phase inverter is much more demanding than that for dc/dc converter.

A more accurate noise source and parasitic path identification for DM EMI prediction of chopper circuit was proposed in chapter 2. In this method, the active device current is identified as the noise source and the noise path including the interconnect parasitics and device parasitics identified through parasitics extraction tool –Maxwell Q3D. This method was proven to be effective for differential mode (DM) EMI. It shows the appreciation of the fundamental mechanisms by which the DM EMI noises are excited and propagated. The DM EMI is dominated in the low-frequency region by the pulse-width-modulation (PWM) switching and the resonant peak in high frequency region is caused by the parasitic elements coupling with device switching dynamics in the EMI excitation.

Although the prediction result from this modeling method matched well with numeric simulation and experiment in both low frequency and high frequency range for single noise source circuit, the adoption of this method to multiple noise source circuit – three-phase inverter with complex SVM operation is still a challenge. This chapter attempts to predict the DM EMI of three-phase inverter with more accurate noise source and path models based on this proposed modeling method. A 300 V, 10 kW, three-phase IGBT inverter was used as the studied circuit. Predictions with the proposed modeling method were performed and the predicted results are compared with experiment results. Since the modulation scheme is taken to account in the noise source modeling, this methodology can be applied to other three-phase PWM inverters to evaluate their DM EMI spectrum.

The three different noise source models based on three different modulation schemes, sinusoidal pulse width modulation (SPWM), SVM and bus-clamped discontinuous pulse width modulation (DPWM) are derived. Predictions with the proposed modeling method were performed for different modulation schemes, and the predicted results are compared with those from experiments. The results show that the modulation schemes have effects not only in switching frequency related harmonics, but also in high frequency range as well.

3.1 Introduction

The straightforward frequency-domain method was based on the description of the system topology using transfer function and a direct frequency representation of the noise sources. Using this method, we can avoid time domain simulation which is time consuming and requires a large amount of computer storage. However, the obstacle that prevents this method from widely used is the accuracy of the noise source and path identification and description. Chapter 2 proposed the method which focuses more accurate noise source and noise path identification for single phase chopper. However, for three phase inverter, the circuit topology becomes more complex, which means that the noise propagation path becomes more complex; the control method can be SPWM control or space vector modulation rather than constant duty PWM control, therefore, the noise source representation could be more complicated.

Since the single-phase chopper circuit is the base of three-phase inverter, it is necessary to start with the DM noise modeling of the chopper circuit to develop the more accurate DM model for three-phase inverter circuit. Fig. 3.1 shows the simple chopper circuit that consists a diode and an active switch and an electrolytic capacitor with an equivalent series resistor (ESR), R_{dc} and inductor (ESL), L_{dc}. Because the parasitic inductance plays an important role on the EMI performance, all the parasitic inductance values have to be known in order to predict EMI performance accurately.

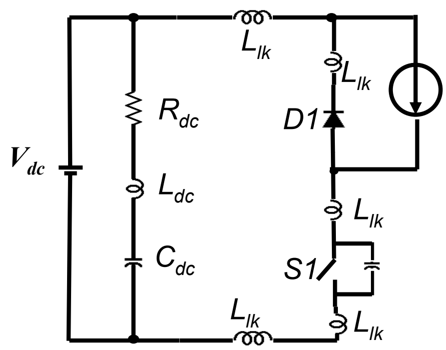

Fig. 3.1 Single phase Chopper Circuit

The single phase leg in the above chopper can be replaced with a high frequency circuit as shown in Fig. 3.2. It consist a current source as noise source and the parasitics including device lead inductance, output capacitance and as noise propagation path.

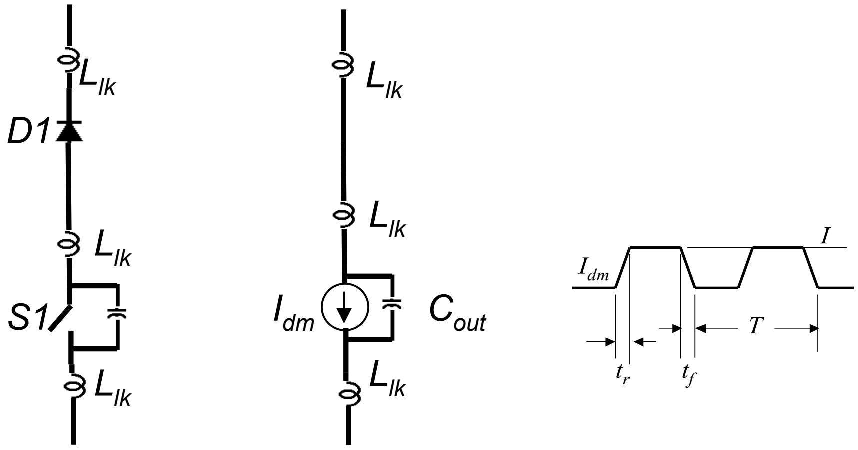

Fig. 3.2 high frequency equivalent circuit and noise current source representation

The time domain waveform of the current source as shown in Fig. 3.2 can be approximated as a trapezoidal waveform with finite rise time and fall time assuming that the filter inductor is large enough to make the current ripple small. It can also be assumed that the rise time is identical to the fall time.

The frequency domain representation of the trapezoid waveform is shown (1),

$$I_n = 2Id\,\frac{\sin(n\pi d)}{n\pi d}\,\frac{\sin\left(n\pi t_f / T\right)}{n\pi t_f / T} \tag{3-1}$$

where d is the duty cycle, T is the inverter switching period, I is the current amplitude, and n is the harmonic order.

The duty cycle d and current amplitude I are constant value in single phase chopper, however, this is not the case for three-phase inverter as shown in Fig. 3.3. In three-phase inverter, the duty cycle is determined by modulation scheme and the current amplitude varies sinusoidal during a line cycle. Therefore, (3-1) can not be used for three phase inverter. New noise source representation in frequency domain has to be found for three phase inverter.

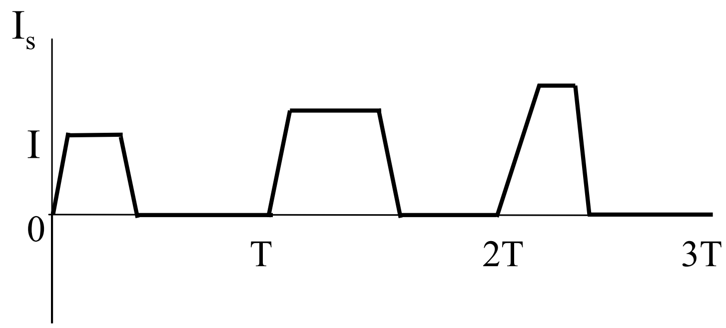

Fig. 3.3 Switching current within switching cycle

On the other hand, the physical layout of three phase inverter is much more complicated than that of single phase chopper, which increases the difficulty for noise propagation path determination. Fig. 3.4 shows a three-phase inverters circuit including six active switches, device parasitic inductance and interconnect inductance, which consists of six noise sources and has much more complex noise propagation paths than those of the single-phase chopper. Therefore, a unique high frequency equivalent circuit for three-phase inverter has to be determined first.

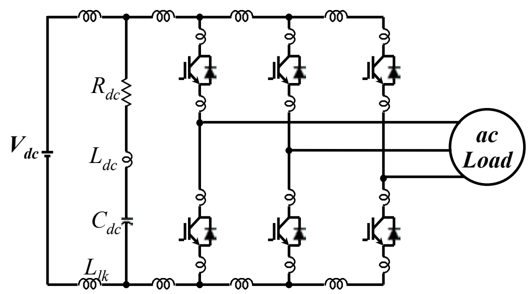

Fig. 3.4 Inverter circuit with parasitic Inductance

3.2 The proposed modeling and prediction method

The following part of this chapter attempts to apply this modeling method to predict DM EMI spectrum of three-phase inverter circuit. To calculate the DM noise for such complex circuit, the noise source and propagation path have to be identified clearly. Assuming that the active device current is the DM noise source, the first step is to determine the period in which phase current flows through active switch or freewheeling diode according to inverter operation. Fig. 3.5 shows the combination of inverter output current distribution. Here, the upper half wave of the phase current flow is defined as positive. The inverter operation can be divided into six part represented by six sub-circuits

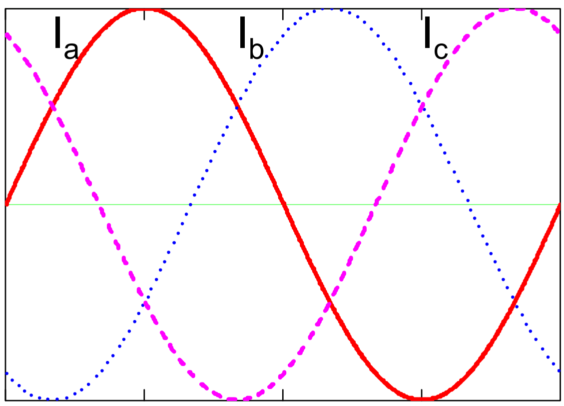

(1) $I_a>0$, $I_b>0$, $I_c<0$
(2) $I_a>0$, $I_b<0$, $I_c<0$
(3) $I_a>0$, $I_b<0$, $I_c>0$
(4) $I_a<0$, $I_b<0$, $I_c>0$
(5) $I_a<0$, $I_b>0$, $I_c>0$
(6) $I_a<0$, $I_b>0$, $I_c<0$

Fig. 3.5 Combination of inverter output current distribution

These sub-circuits are shown in Fig. 3.6 according to the direction of current distribution. In each sub-circuit, each phase leg is reduced to an active switch and a freewheeling diode, which is the same as the single-phase chopper circuit. Therefore, the high frequency equivalent circuit for the chopper can be applied to each phase leg. The high frequency equivalent circuit can be used to represent the nonlinear switch model of each phase leg with respect to the current direction. Fig. 3.7 presents the high frequency model in which the current source is pulsating current representing the current going through the active switch and C_{out} is the device output capacitance.

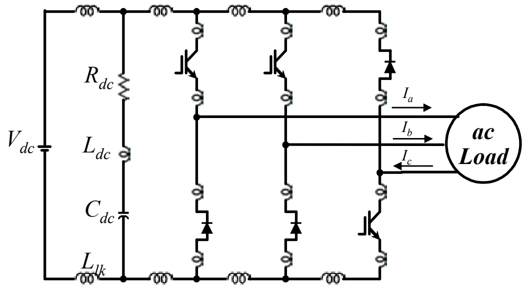

(1) $I_A>0, I_B>0, I_C<0$

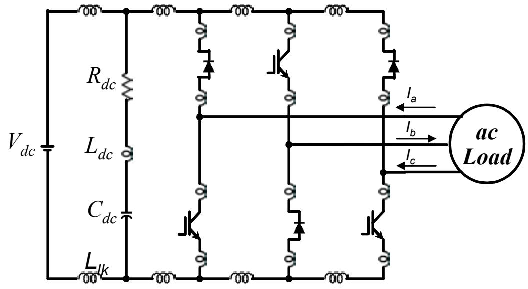

(2) $I_A<0, I_B>0, I_C<0$

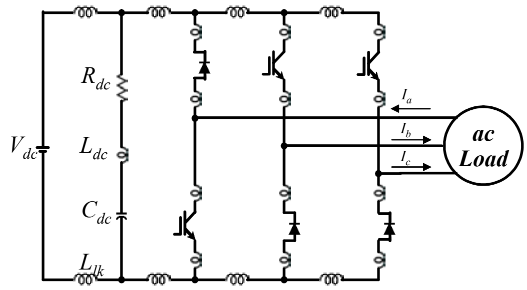

(3) $I_A<0, I_B>0, I_C>0$

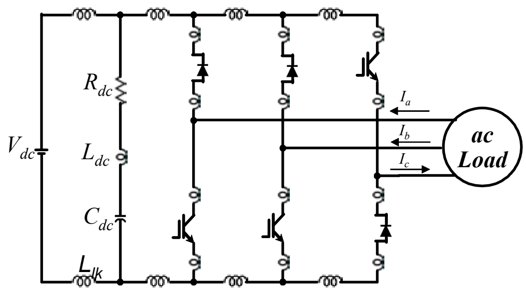

(4) $I_A<0, I_B<0, I_C>0$

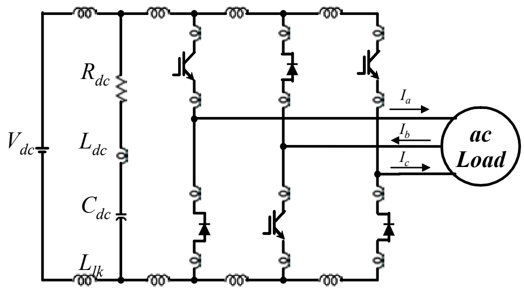

(5) $I_A>0$, $I_B<0$, $I_C>0$

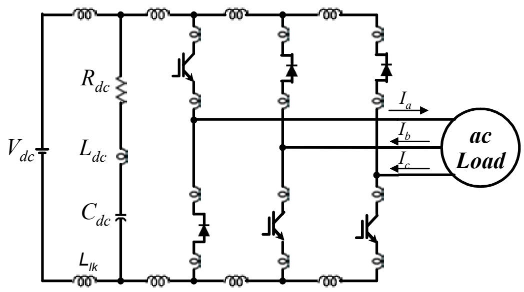

(6) $I_A>0$, $I_B<0$, $I_C<0$

Fig. 3.6 Sub-circuits of inverter operation

By putting the high frequency model into each sub-circuit, each sub-circuit becomes a linear circuit that can directly be solved in frequency domain. For example, Fig. 3.8 shows the high frequency circuit for sub-circuit 1, and the DM noise voltage across LISN during this period can be calculated with (3-2). The total DM noise across the LISN for the inverter during a fundamental cycle can be achieved by summing the DM noise voltage of all the sub-circuits according to (3-3).

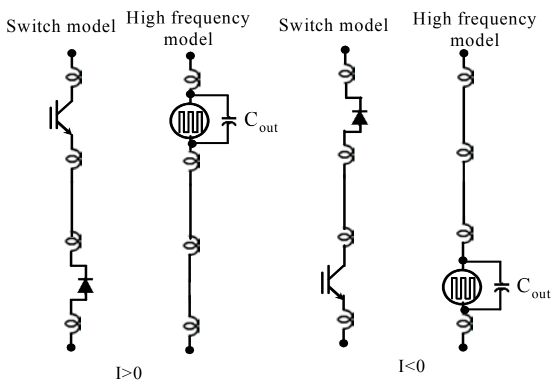

Fig. 3.7 High frequency model of phase leg

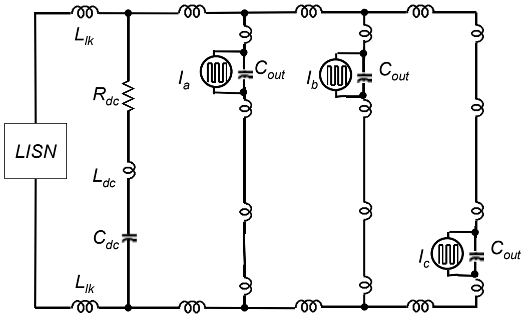

Fig. 3.8 High frequency linear circuit of sub-circuit 1

$$V_k(f) = V_{ak}(f) + V_{bk}(f) + V_{ck}(f)$$
$$V_{ak}(f) = I_{ak}(f) Z_{ak}(f) \qquad k=1,2\cdot\cdot\cdot 6$$
$$V_{bk}(f) = I_{bk}(f) Z_{bk}(f)$$
$$V_{ck}(f) = I_{ck}(f) Z_{ck}(f) \tag{3-2}$$

Here, k is the number of the sub-circuit, $V_{ak}(f)$, $V_{bk}(f)$ and $V_{ck}(f)$ are the noise voltage at LISN produced by current noise source $I_{ak}(f)$, $I_{bk}(f)$ and $I_{ck}(f)$ respectively. $Z_{ak}(f)$, $Z_{bk}(f)$ and $Z_{ck}(f)$ are noise propagation path for each phase in the sub-circuits.

$$V_{dm}(f) = \sum_{k=1}^{6} V_k(f) \tag{3-3}$$

It can be derived from Fig. 3.7 and Fig. 3.8 that all the sub-circuits have the same configuration except that the expressions of the current sources are different. Hence, it is possible to unify all the six sub-circuit together to one equivalent circuit which is much more convenient to calculate the noise generated on LISN. The DC link current always satisfies the condition in (3-4).

$$i_{dc} = S_a i_a + S_b i_b + S_c i_c \tag{3-4}$$
$$S_k = \begin{cases} 1 & \text{when top switch is on} \\ 0 & \text{when bottom switch is on} \end{cases} \quad k = a, b, c$$

In other words, (3-4) can be applied to each sub-circuit in Fig. 3.6, therefore, a unified circuit model shown in Fig. 3.9 can be achieved for noise calculation. It is also indicated that each phase leg of the inverter can be replaced with a unified high frequency linear model. Fig. 3.10 shows the switch model of inverter phase leg and its unified high frequency linear model. The total DM noise across the LISN for the inverter during a fundamental cycle can be achieved just by calculating the unified circuit model without summing the DM noise voltage of all the sub-circuits in Fig. 3.6.

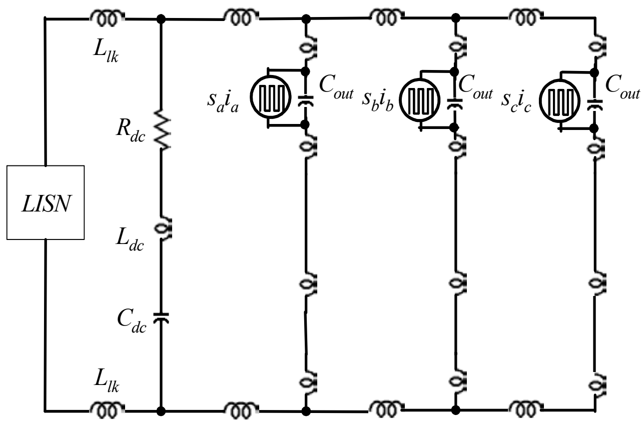

Fig. 3.9 A unified circuit model for DM noise calculation

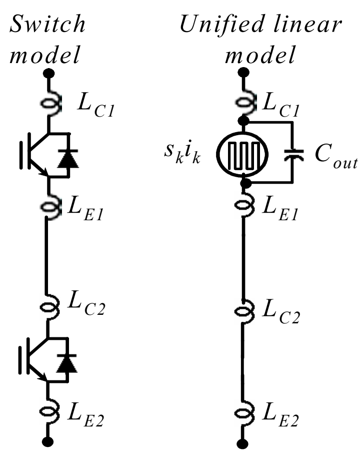

Fig. 3.10 Unified High Frequency linear model of inverter phase leg

The DM noise generated on the LISN, $V_{dm}(f)$, is shown in (3-5)

$$V_{dm}(f) = \sum_{k=a,b,c} I_k(f) Z_k(f) \qquad (3\text{-}5)$$

Here, $I_k(f)$ is expression of $s_k i_k$ in frequency domain.

It is difficult to use the circuit simulator to solve the linear circuit shown in Fig 3.9, because it requires a huge table to describe the current source in a fundamental cycle. Therefore, the frequency domain representation of the current source is necessary.

3.3 Differential mode noise source modeling

Unlike the current source in chopper circuit that has constant duty cycle and amplitude in each switching period, the pulse current of current source in Fig. 3.9 has variable duty cycle and amplitude for each switching period, which leads to the difficulty in Fourier series integral. The common solution to obtaining Fourier integral for SPWM waveform is the double integral Fourier form. The double integral Fourier form applied to device current is given in (3-6).

$$C_{mn} = A_{mn} + jB_{mn} = \frac{1}{2\pi^2} \int_{y_s}^{y_e} \int_{x_r}^{x_f} I(t) \ell^{-j(m\omega_S t + n\omega_0 t)} d(\omega_s t) d(\omega_0 t) \qquad (3\text{-}6)$$

Here $I(t)$ is the phase current going through the device, ω_s is switching frequency, ω_0 is fundamental frequency. The outer integral limit y_e, y_r and inner integral limit x_r, x_f are determined by the modulation scheme and the inverter we studied is operated under the center-aligned SVM. Therefore, in order to derive the frequency domain expression of noise source in Fig. 3.9, the first step should be to determine the outer integral limit and then the inner integral limit with space vector sectors. Fig. 3.11 shows that there are six sectors for inverter operation during a fundamental cycle. The double integral Fourier form can be applied to device current in each sector respectively and thus the double integral Fourier form in a fundamental cycle can be achieved by adding them together as given in (3-7).

$$C_{mn} = \sum_{k=I}^{VI} C_{mnk} \tag{3-7}$$

For instance, the double integral Fourier Form applied to device current in sector I is shown in (3-8) in which the outer integral limit is replaced with $\pi/3$.

$$C_{mnI} = \frac{1}{2\pi^2}\int_0^{\frac{\pi}{3}}\int_{x_r}^{x_f} I_p(t)\ell^{-j(m\omega_s t + n\omega_0 t)} d(\omega_s t) d(\omega_0 t) \tag{3-8}$$

where subscript p can be either of a, b, or c, $I_a(t) = I\cos(\omega_0 t - \alpha)$, $I_b(t) = I\cos(\omega_0 t - \alpha - 2\pi/3)$, $I_c(t) = I\cos(\omega_0 t - \alpha + 2\pi/3)$, $x_r = -\pi d(\omega_0 t)$, $x_f = \pi d(\omega_0 t)$, and $d(\omega_0 t)$ is the duty cycle function of the top switch of each leg.

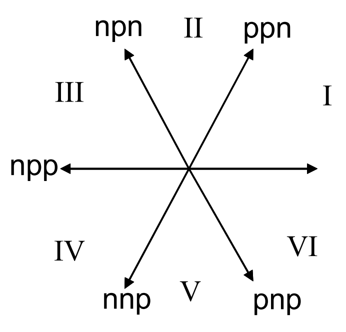

Fig. 3.11 Space vector

The next step is to determine the inner integral limit and the inner integral limit is determined by the duty cycles of the top switch and these duty cycles also have different expressions in different sector regions. The duty cycle functions of the top switch of each leg during different sectors are given in Table 3.I. Fig. 3.12 illustrates those functions in one fundamental cycle when modulation index is 1.

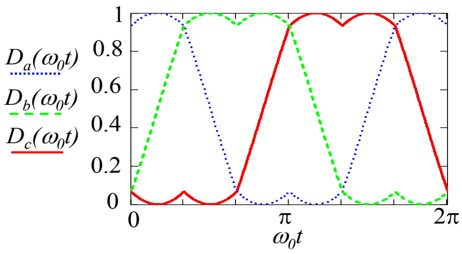

Fig. 3.12 Duty cycles of the upper switch of each phase under center aligned SVM

Table 3.1 Duty cycle function of top switch in each space vector sector

	$d_a(\omega_0 t)$	$d_b(\omega_0 t)$	$d_c(\omega_0 t)$
$[0,\frac{\pi}{3}]$	$\frac{1}{2}(1+M\cos(\omega_0 t-\frac{\pi}{6}))$	$\frac{1}{2}(1+\sqrt{3}M\sin(\omega_0 t-\frac{\pi}{6}))$	$\frac{1}{2}(1-M\cos(\omega_0 t-\frac{\pi}{6}))$
$[\frac{\pi}{3},\frac{2\pi}{3}]$	$\frac{1}{2}(1+\sqrt{3}M\cos(\omega_0 t))$	$\frac{1}{2}(1+M\sin(\omega_0 t))$	$\frac{1}{2}(1-M\sin(\omega_0 t))$
$[\frac{2\pi}{3},\pi]$	$\frac{1}{2}(1+M\cos(\omega_0 t+\frac{\pi}{6}))$	$\frac{1}{2}(1-M\cos(\omega_0 t+\frac{\pi}{6}))$	$\frac{1}{2}(1-\sqrt{3}M\cos(\omega_0 t-\frac{\pi}{3}))$
$[\pi,\frac{4\pi}{3}]$	$\frac{1}{2}(1+M\cos(\omega_0 t-\frac{\pi}{6}))$	$\frac{1}{2}(1+\sqrt{3}M\sin(\omega_0 t-\frac{\pi}{6}))$	$\frac{1}{2}(1-M\cos(\omega_0 t-\frac{\pi}{6}))$
$[\frac{4\pi}{3},\frac{5\pi}{3}]$	$\frac{1}{2}(1+\sqrt{3}M\cos(\omega_0 t))$	$\frac{1}{2}(1+M\sin(\omega_0 t))$	$\frac{1}{2}(1-M\sin(\omega_0 t))$
$[\frac{5\pi}{3},2\pi]$	$\frac{1}{2}(1+M\cos(\omega_0 t+\frac{\pi}{6}))$	$\frac{1}{2}(1-M\cos(\omega_0 t+\frac{\pi}{6}))$	$\frac{1}{2}(1-\sqrt{3}M\cos(\omega_0 t-\frac{\pi}{3}))$

To further derive the analytical expression of (3-8), the double Fourier form can still be applied. With switching current of phase A in vector sector I as a example, the inner integral in (3-8) can be changed based on Table 3.1, and the result is shown in (3-9). Initially, the sideband effect is not taken into account n is assumed to be zero. More completed result will be presented in the following section with the consideration of sideband effect.

$$
\begin{aligned}
C_{mnI} &= \frac{1}{2\pi^2}\int_0^{\frac{\pi}{3}}\int_{-\frac{\pi}{2}(1+M\cos(\omega_0 t-\frac{\pi}{6}))}^{\frac{\pi}{2}(1+M\cos(\omega_0 t-\frac{\pi}{6}))} I\cos(\omega_0 t-\varphi)\ell^{-j(m\omega_s t)}d(\omega_s t)d(\omega_0 t) \\
&= \frac{I}{2\pi^2 m}\int_0^{\frac{\pi}{3}}\cos(\omega_0 t-\varphi)(\ell^{j(m\frac{\pi}{2}(1+M\cos(\omega_0 t-\frac{\pi}{6})))}-\ell^{-j(m\frac{\pi}{2}(1+M\cos(\omega_0 t-\frac{\pi}{6})))})d(\omega_0 t)
\end{aligned}
\tag{3-9}
$$

The integral result of (3-9) is summations of Bessel function. It indicates that the integral results over a fundamental cycle are several summations of Bessel function according to (3-7). Fig. 3.13 shows the frequency spectrum of the switch current in each phase over a fundamental cycle, which was plotted by Mathcad™. It should be pointed out that this spectrum is identical for all three phases. Although the switching frequency, f_s, is 20 kHz, and the fundamental frequency, f_0, is 200 Hz, the first peak occurs at 40 kHz instead of 20 kHz and the rest of peak in switching frequency harmonic range only occurs at even harmonics of switching frequency. In high frequency range, the frequency spectrum introduces a near 30 dB/dec slope drop.

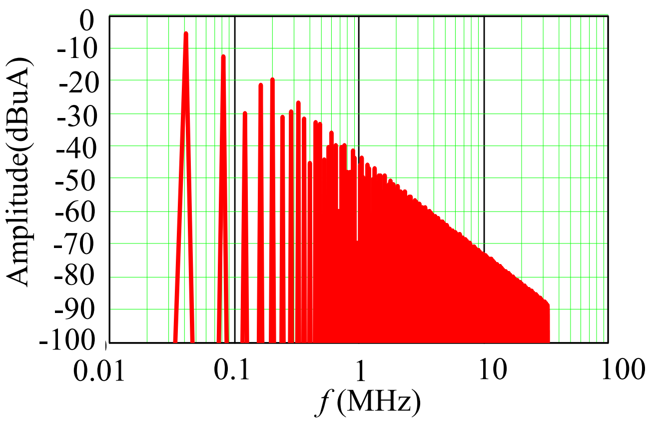

Fig. 3.13 Spectral representation of noise source in each phase

3.4 Differential mode path modeling

Parasitic parameters of EMI-related components, including resistors, capacitors, power buses and devices must be determined for EMI prediction. To facilitate an experimental verification of this prediction approach, a 10-kW three-phase IGBT-based inverter made on PCB board was used. Resistor and inductor are connected in series as the inverter load. The motor was not used as load for the purpose of isolation of noise generated from motor and those form inverter. In this paper, we are only concerned about noise generated from inverter. There are no high frequency capacitors putting across devices on each bridge because the noise caused by the parasitic component of devices and PCB can be magnified to show the significance of the individual parasitic components. The parameters of the parasitic components are identified through numerical computations using FEA tools.

A. IGBT parasitic inductance

The IGBT used on this inverter was IRG4PSC71UD with TO247 pacakge and the device parasitics were analyzed using Maxwell Q3D. The resulting parasitic inductance are shown in Table 3.2. In this table, the diagonal elements of the matrices are self inductances, and the off-diagonal elements are the mutual inductances.

Table 3.2 calculated results of the device parasitic inudctance

	Inductance (nH)		
Lead	Collector	Emitter	Gate
Collector	15.9	5.88	5.88
Emitter	5.88	15.9	3.73
Gate	3.73	5.88	15.9

The calculated inductance mathematically represents the component of the inductance that results from the part of the current loop being modeled. The current always flow in collector (emitter) lead and out emitter (collector) lead, therefore the loop inductance between collector and emitter can be obtained by

$$L_{loop\text{-}ce} = L_{cc} + L_{ee} - L_{ce} - L_{ec} = 20.04 \text{ nH}$$

Assuming that L_c=L_e=10.02nH, and the coupling effect between device leads is negligible, the total parasitic inductance induced by IGBT leads on one phase leg becomes 40.08 nH.

B. DC bus parasitic inductance

The inverter PCB consists of inverter DC buses, AC bus, gate drive part and auxiliary power supply part. Among them, the DC buses occupy the largest area on the board and it is the dominant DM EMI path. To reduce the computation load of parameter extraction, only parasitic inductance on DC bus was extracted.

The dc buses consist of copper traces on four major PCB layers as shown in Fig. 3.14, where the top two layers are DC positive and the bottom two layers are DC negative. The coupling effect between each phase has to be taken into account, and Table 3.3 shows the extracted parasitic inductance from Maxwell Q3D.

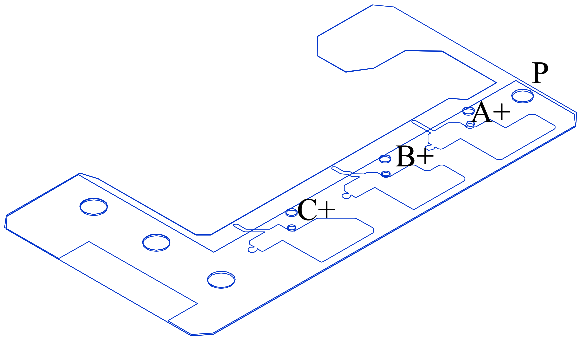

(a)

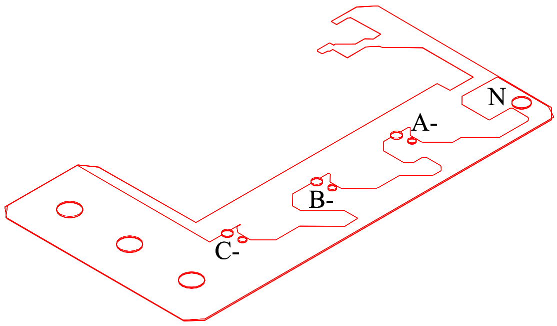

(b)

Fig. 3.14 DC bus structure (a) positive bus (b) negative bus

Table 3.3 Calculated results of the DC bus parasitic inudctance

	Inductance (nH)					
	L_{C+}	L_{B+}	L_{A+}	L_{A-}	L_{B-}	L_{C-}
L_{C+}	86.7	45.8	14.1	26.3	60.5	91.4
L_{B+}	45.8	53.9	15.1	23.6	37.2	41.6
L_{A+}	14.1	15.1	9.5	9.7	11.7	12.7
L_{A-}	26.3	23.6	9.7	20.3	26.5	29.3
L_{B-}	60.5	37.2	11.7	26.5	53.8	67.6
L_{C-}	91.4	41.6	12.7	29.3	67.6	114.4

The above table can be simplified based on the fact that three pairs of parasitic inductance L_{C+} and L_{C-}, L_{B+} and L_{B-} , and L_{A+} and L_{A-} , are all in series as illustrated in Fig. 3.15. According the concept of loop inductance given in (3-10) and (3-11), a reduced parasitic inductance matrix that is more convenient for DM noise analysis can be derived. Table 3.4 shows the reduced parasitic inductance matrix of DC bus.

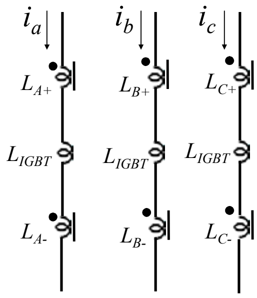

Fig. 3.15. Equivalent circuit of extracted inductance matrix

$$L_{mm}=L_{m+m+}+L_{m-m-}-2L_{m+m-} \tag{3-10}$$

$$L_{mn}=L_{m+n+}+L_{m-n-}-L_{m-n+}-L_{m+n-} \tag{3-11}$$

where, $m=A,B,C,\ n=A,B,C.$

Table 3.4 Reduced parasitic inductance matrix of DC bus

	Inductance (nH)		
	L_C	L_B	L_A
L_C	33.2	11.3	6.3
L_B	11.3	18.3	4.3
L_A	6.3	4.3	10.3

With most of the high-frequency parasitic inductance identified for major EMI-related components in the tested inverter, a high-frequency linear model of the inverter circuit can be developed as shown in Fig. 3.16. The parameters in the circuit are L_{IGBT}=40.08 nH, C_{out}=0.6 nF, C_{dc}=620 uF, L_{dc}=100 nH and R_{dc}=15 mΩ.

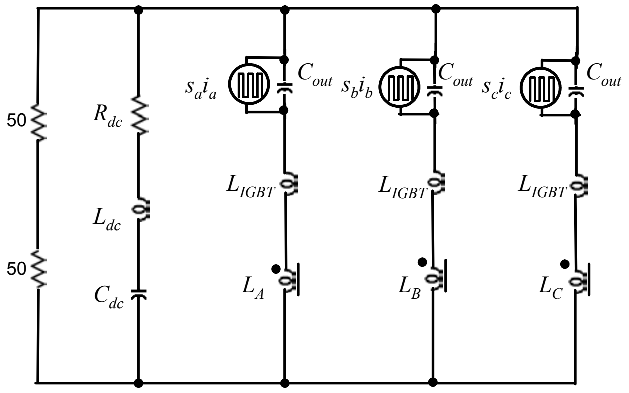

Fig. 3.16 High frequency model of inverter of DM noise prediction

Since all the parasitic components are known, we can calculate the propagation path transfer function by solving the equivalent linear circuit in Fig. 3.17. The definition of the propagation path transfer function is given in (3-12)

$$Z_a(f) = \frac{V_a(f)}{I_a(f)}, Z_b(f) = \frac{V_b(f)}{I_b(f)}, Z_c(f) = \frac{V_c(f)}{I_c(f)} \tag{3-12}$$

where $V_a(f)$ is the noise voltage across the LISN excited by the noise source $I_a(f)$.

Fig. 3.17 shows the propagation path transfer function plotted by Mathcad. It can be seen that the resonant points occur at the same point for different phases that are excited by the noise sources. For the first resonant point, not only the frequency but also the peak is equal. Different damping occurs for the rest of resonant points. These resonant points are basically determined by the loop inductance and the parasitic output capacitance of the IGBT.

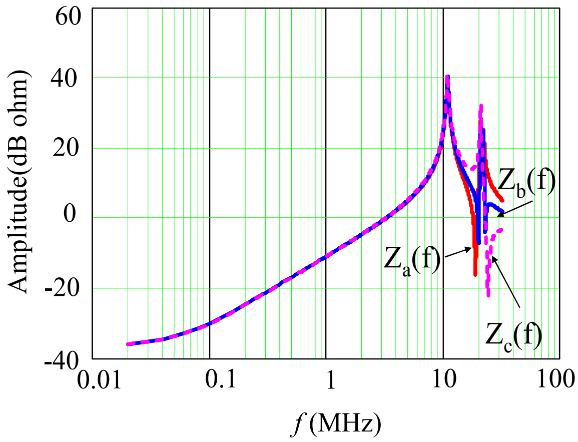

Fig. 3.17 The plot of the propagation path transfer function

3.5 Validation through simulation and experiment

To validate the proposed modeling and calculation method, the high frequency noise produced by the inverter has to be measured. A set of LISNs are placed between the battery source and the inverter under test. The LISN provides 50-ohm impedance matching for entire high frequency range. The output of the LISN can be connected to oscilloscope or spectrum analyzer to obtain the spectrum. A two way 180-degree power combiner manufactured by Mini-Circuits is used to extract the DM noise. Fig. 3.18 shows the EMI test setup. The center aligned SVM signals are sent out by a digital signal processor (DSP) – ADMC 401™. The output of the inverter feeds to a three-phase resistor (48 ohm) and inductor (600 uH) load with Y configuration. The inverter operation condition is as following:

switching frequency f_s	20 kHz
output fundamental frequency f_0	200 Hz
modulation index M	0.75
peak value of output current I_{pk}	4 A
output power P_{in}	620 W
DC bus voltage V_{in}	300 V

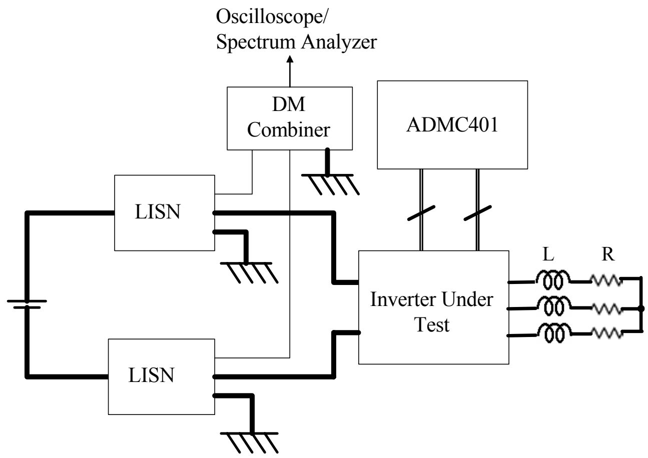

Fig. 3.18 Block diagram of EMI test setup

The DM EMI spectrum of inverter during a fundamental cycle can be calculated using (3-4) based on the source and path models derived in sections 3 and 4. Fig. 3.19 shows the calculated results, which are compared with experimental results in Fig. 3.20. The calculated result using the proposed method matches the experimental result both in switching frequency range and in high frequency range very precisely. It can be seen that in switching frequency harmonic range noise peak only occurs at even harmonics, which validates the modeling of the noise source. In high frequency range, the resonant point matches well between the calculated result and the experimental result, which validates the modeling of noise propagation path. It is also indicated that the resonant points of the noise propagation path determine the location of the peak of the EMI spectrum.

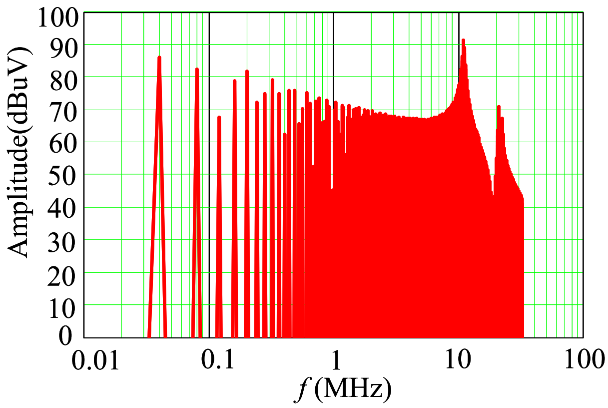

Fig. 3.19 Frequency domain calculated result of DM EMI spectrum

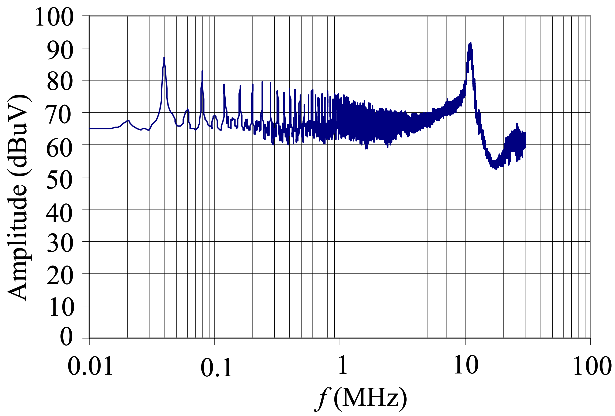

Fig. 3.20 Experimental result of DM EMI spectrum

A slight difference is observed between the calculated result and experimental results in higher frequency range around the second resonant peak. The differences in higher frequency spectrum may be caused by lack of models of other parasitic effects on the inverter board. For example, no ac bus parasitics were taken into account and the AC resistance, which is regarded as a fixed value, is a function of frequency and it will increase dramatically as in high frequency region because of skin effect and proximity effect.

3.6 Modulation scheme effect on DM EMI spectrum

Since the DM EMI prediction results from this modeling method match well with experiment results both in low frequency and high frequency ranges for three-phase inverter under center-aligned space vector modulation (SVM), it is interesting to extend this method to other modulation scheme to predict DM EMI spectrum.

Although PWM technique has been the subject of intensive research of three-phase inverters for the last couple decades, most of the work has concentrated on the harmonics produced on the ac output, rather than the effect of modulation scheme on EMI spectrum at the dc input. Hence, it is the intension of this chapter to evaluate the effect of different modulation schemes on EMI spectrum at the dc input.

3.6.1. Noise source modeling under different Modulation Scheme

Over the last several decades, a number of PWM methods have been develop, however, only several of them have been widely accepted [12]. These accepted methods can be divided input two classes, continuous PWM and discontinuous PWM method. The continuous PWM method indicates that these are always switching actions occurring for each phase leg during a switching cycle. The common SPWM and center-aligned SVM method belong to this class. In discontinuous PWM method a phase has a period during which the output voltage of this phase is clamped to either positive dc bus rail or negative dc bus rail. This period lasts at most one third of the fundamental cycle. This method is known for less switching loss compared to SPWM and center-aligned SVM method because it takes less switching actions. However, the effect on EMI spectrum imposed by this method has not been studied. In this paper, three PWM methods, SPWM, SVM and DPWM, will be discussed. Although only one of DPWM methods is discussed, the result can be extended to other DPWM methods.

A. SPWM

In the conventional SPWM method, the duty cycle function of the phase-*a* top switch can be represented in (3.13).

$$d_a(\omega_0 t) = \frac{1}{2}(1 + M\cos(\omega_0 t)) \tag{3-13}$$

For phase-b and -c, the only difference is a 120° phase shift, thus the duty cycle function of three-phase top switches on each phase under SPWM can be illustrated in Fig. 3.21.

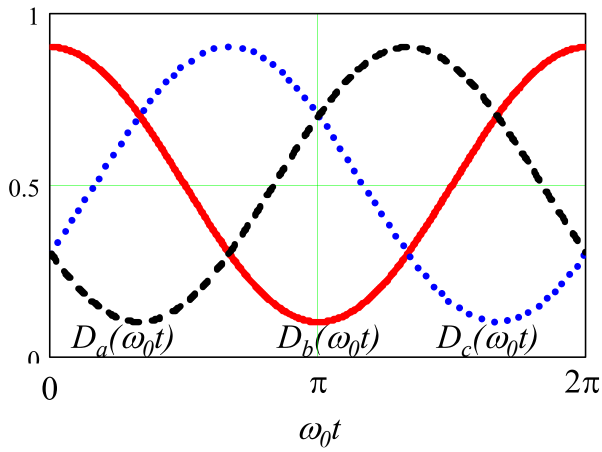

Fig. 3.21 Duty cycles of the upper switch of each phase under SPWM

The noise source model under SPWM method can be obtained from double integral Fourier form applied to device current, which is shown in (3-14).

$$C_{mn} = \frac{1}{2\pi^2}\int_0^{2\pi}\int_{-\frac{\pi}{2}(1+M\cos(\omega_0 t))}^{\frac{\pi}{2}(1+M\cos(\omega_0 t))} I\cos(\omega_0 t - \varphi)\ell^{-j(m\omega_s t+\omega_0 t)} d(\omega_s t)d(\omega_0 t) \tag{3-14}$$

$$= \frac{I}{2\pi^2 m}\int_0^{2\pi}\cos(\omega_0 t - \varphi)\ell^{-j(\omega_0 t)}(\ell^{j(m\frac{\pi}{2}(1+M\cos(\omega_0 t)))} - \ell^{-j(m\frac{\pi}{2}(1+M\cos(\omega_0 t)))})d(\omega_0 t)$$

It was demonstrated above that the LISN absorbs the sum of the currents flowing in each phase at the switching frequency and its harmonics range. The sum of the noise source models for all three phases is given in (3-15).

$$C_{mn} = \sum_{k=a,b,c} C_{kmn} \tag{3-15}$$

Fig. 3.22 illustrates the sum of the noise source model for all three phases under SPWM method at switching frequency (20 kHz) and its harmonics range. Note that the side band effect is considered. The highest peak occurs at the second harmonics frequency 40 kHz, not at the switching frequency.

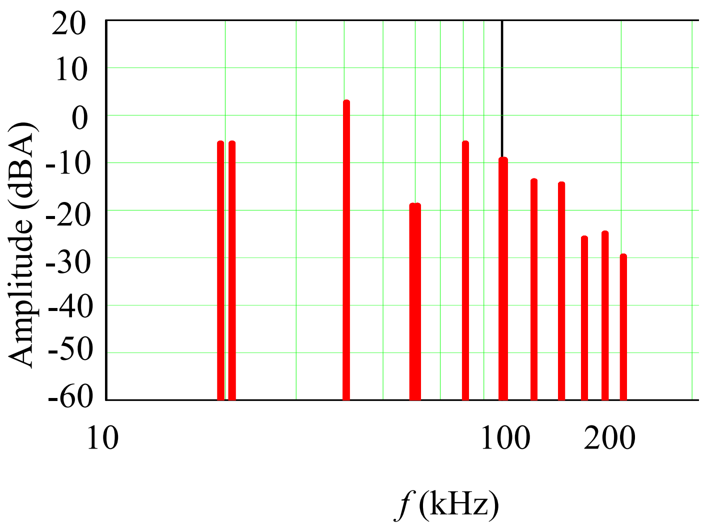

Fig. 3.22 Sum of the noise source models under SPWM.

B. SVM

The center-aligned SVM method was proposed in 1980s and was obtained by averaging the duty cycle over two consecutive switching states. The phase-a top switch duty cycle function is described in (3-16). The duty cycle function of three top switches on each phase under SVM method is then illustrated in Fig. 3.23.

$$d_a(\omega_0 t)=\begin{cases}\frac{1}{2}(1+M\cos(\omega_0 t-\frac{\pi}{6})) & if\ 0<\omega_0 t<\frac{\pi}{3}\\ \frac{1}{2}(1+\sqrt{3}M\cos(\omega_0 t)) & if\ \frac{\pi}{3}<\omega_0 t<\frac{2\pi}{3}\\ \frac{1}{2}(1+M\cos(\omega_0 t+\frac{\pi}{6})) & if\ \frac{2\pi}{3}<\omega_0 t<\pi\\ \frac{1}{2}(1+M\cos(\omega_0 t-\frac{\pi}{6})) & if\ \pi<\omega_0 t<\frac{4\pi}{3}\\ \frac{1}{2}(1+\sqrt{3}M\cos(\omega_0 t)) & if\ \frac{4\pi}{3}<\omega_0 t<\frac{5\pi}{3}\\ \frac{1}{2}(1+M\cos(\omega_0 t+\frac{\pi}{6})) & if\ \frac{5\pi}{3}<\omega_0 t<2\pi\end{cases} \tag{3-16}$$

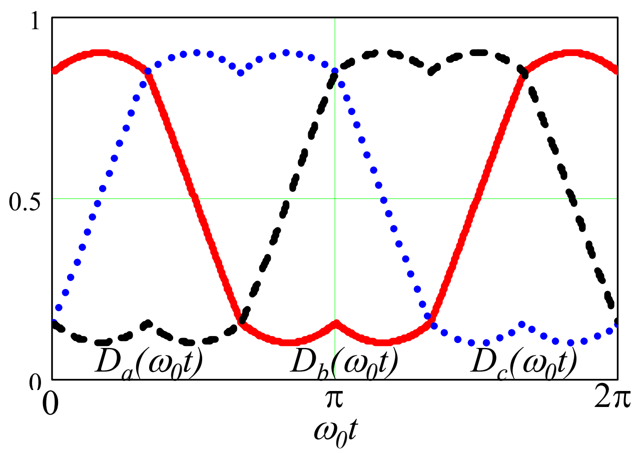

Fig. 3.23 Duty cycles of the upper switch of each phase under SVM

The noise source model under SVM method can be obtained from double integral Fourier form applied to device current according to the duty cycle function, which is shown in (3-17).

$$
\begin{aligned}
C_{amn} = {} & \frac{1}{2\pi^2}\int_{0}^{\frac{\pi}{3}}\int_{-\frac{\pi}{2}(1+M\cos(\omega_0 t-\frac{\pi}{6}))}^{\frac{\pi}{2}(1+M\cos(\omega_0 t-\frac{\pi}{6}))} A d(\omega_s t) d(\omega_0 t) \\
& + \frac{1}{2\pi^2}\int_{\frac{\pi}{3}}^{\frac{2\pi}{3}}\int_{-\frac{\pi}{2}(1+\sqrt{3}M\cos(\omega_0 t))}^{\frac{\pi}{2}(1+\sqrt{3}M\cos(\omega_0 t))} A d(\omega_s t) d(\omega_0 t) \\
& + \frac{1}{2\pi^2}\int_{\frac{2\pi}{3}}^{\pi}\int_{-\frac{\pi}{2}(1+M\cos(\omega_0 t+\frac{\pi}{6}))}^{\frac{\pi}{2}(1+M\cos(\omega_0 t+\frac{\pi}{6}))} A d(\omega_s t) d(\omega_0 t) + \\
& \frac{1}{2\pi^2}\int_{\pi}^{\frac{4\pi}{3}}\int_{-\frac{\pi}{2}(1+M\cos(\omega_0 t-\frac{\pi}{6}))}^{\frac{\pi}{2}(1+M\cos(\omega_0 t-\frac{\pi}{6}))} A d(\omega_s t) d(\omega_0 t) + \\
& \frac{1}{2\pi^2}\int_{\frac{4\pi}{3}}^{\frac{5\pi}{3}}\int_{-\frac{\pi}{2}(1+\sqrt{3}M\cos(\omega_0 t))}^{\frac{\pi}{2}(1+\sqrt{3}M\cos(\omega_0 t))} A d(\omega_s t) d(\omega_0 t) + \\
& \frac{1}{2\pi^2}\int_{\frac{5\pi}{3}}^{2\pi}\int_{-\frac{\pi}{2}(1+M\cos(\omega_0 t+\frac{\pi}{6}))}^{\frac{\pi}{2}(1+M\cos(\omega_0 t+\frac{\pi}{6}))} A d(\omega_s t) d(\omega_0 t)
\end{aligned}
\tag{3-17}
$$

where $A=I\cdot\cos(\omega_0 t - \varphi)\lambda^{-j(m\omega_s t+\omega_0 t)}$. Fig. 3.24 illustrates the sum of the noise source model for all three phases under SVM method at the switching frequency (20 kHz) and its harmonics range. It is the same with SPWM that the highest peak occurs at the second harmonics frequency 40 kHz, not at the switching frequency. In addition, this method shows lower peak value at the switching frequency and its associated odd harmonics compared with the SPWM method.

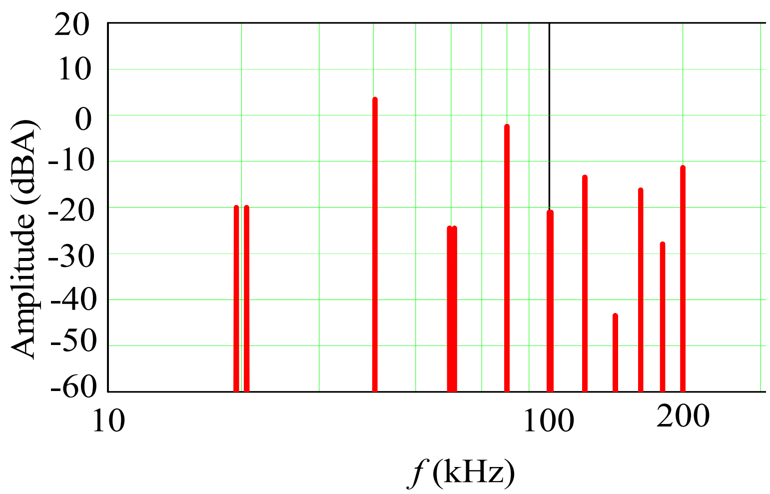

Fig. 3.24 Sum of the noise source models under SVM

C. DPWM

Using a discontinuous type of zero-sequence signal, a modulation method with discontinuous modulation waves was developed. Since during each carrier cycle one phase ceases modulation, the associated phase is clamped to the positive or negative dc rail and the switching losses of the associated inverter leg are eliminated. One DPWM method is chosen for study, which is described by (3-18).

$$d_a(\omega_0 t) = \begin{cases} 1 \ \ if \ \ 0 < \omega_0 t < \dfrac{\pi}{3} \\ M\cos(\omega_0 t - \dfrac{\pi}{6}) \ \ if \ \ \dfrac{\pi}{3} < \omega_0 t < \dfrac{2\pi}{3} \\ 1 + M\cos(\omega_0 t + \dfrac{\pi}{6}) \ \ if \ \ \dfrac{2\pi}{3} < \omega_0 t < \pi \\ 0 \ \ if \ \ \pi < \omega_0 t < \dfrac{4\pi}{3} \\ M\cos(\omega_0 t - \dfrac{\pi}{6}) \ \ if \ \ \dfrac{4\pi}{3} < \omega_0 t < \dfrac{5\pi}{3} \\ 1 + M\cos(\omega_0 t + \dfrac{\pi}{6}) \ \ if \ \ \dfrac{5\pi}{3} < \omega_0 t < 2\pi \end{cases} \quad (3\text{-}18)$$

The duty cycle function of three top switches on each phase is shown in Fig. 3.25.

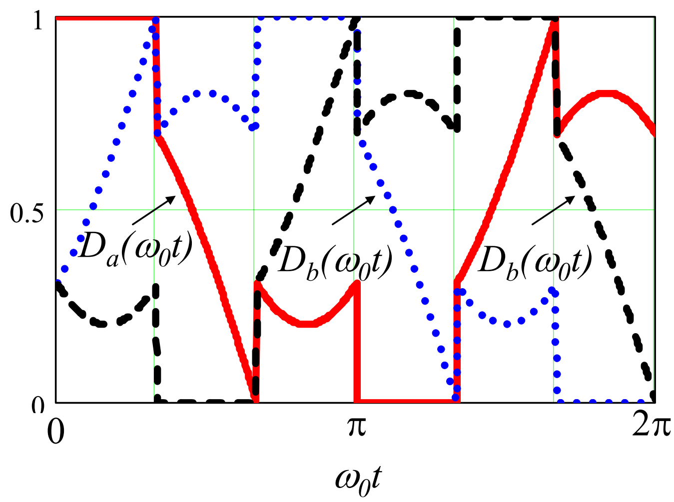

Fig. 3.25 Duty cycles of the upper switch of each phase under clamped-bus DPWM

The noise source model under DPWM method can be obtained from double integral Fourier form applied to the device current, which is a function of the duty cycle. The noise source model of the DPWM method can be expressed in (3-19).

$$
\begin{aligned}
C_{mn} &= \frac{1}{2\pi^2}\int_{\frac{\pi}{3}}^{\frac{2\pi}{3}}\int_{-\pi M\cos(\omega_0 t-\frac{\pi}{6})}^{\pi M\cos(\omega_0 t-\frac{\pi}{6})} A d(\omega_s t) d(\omega_0 t) \\
&+\frac{1}{2\pi^2}\int_{\frac{2\pi}{3}}^{\pi}\int_{-\pi(1+M\cos(\omega_0 t+\frac{\pi}{6}))}^{\pi(1+M\cos(\omega_0 t+\frac{\pi}{6}))} A d(\omega_s t) d(\omega_0 t)+ \\
&\frac{1}{2\pi^2}\int_{\frac{4\pi}{3}}^{\frac{5\pi}{3}}\int_{-\pi M\cos(\omega_0 t-\frac{\pi}{6})}^{\pi M\cos(\omega_0 t-\frac{\pi}{6})} A d(\omega_s t) d(\omega_0 t)+ \\
&\frac{1}{2\pi^2}\int_{\frac{5\pi}{3}}^{2\pi}\int_{-\pi(1+M\cos(\omega_0 t+\frac{\pi}{6}))}^{\pi(1+M\cos(\omega_0 t+\frac{\pi}{6}))} A d(\omega_s t) d(\omega_0 t)
\end{aligned}
\tag{3-19}
$$

where $A = I\cdot\cos(\omega_0 t - \varphi)\lambda^{-j(m\omega st+\omega 0t)}$. Fig. 3.26 illustrates the sum of the noise source model for all three phases under DPWM method at the switching frequency of 20 kHz and its associated harmonics. Unlike SPWM and SVM methods, DPWM method presents the highest peak at the switching frequency. This proves that that different modulation schemes present different noise source models that lead to different noise spectra at the switching frequency and its associated harmonics.

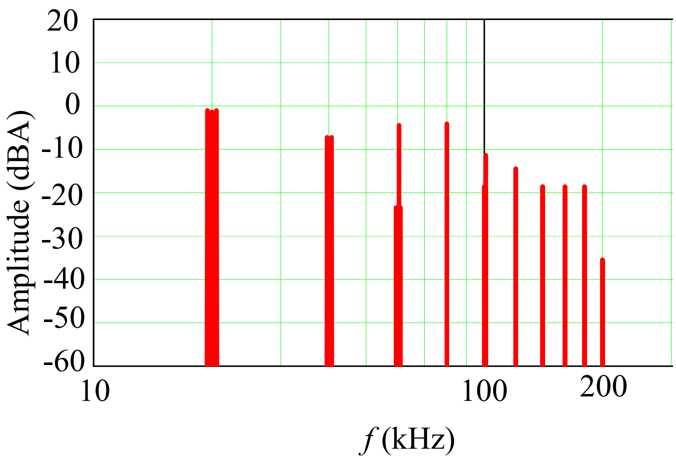

Fig. 3.26 Sum of the noise source models under DPWM.

3.6.2 Experiment Verification

The DM EMI spectrum of inverter during a fundamental cycle can be calculated using (3-4) based on the source and path models derived in sections 3 and 4. Fig. 3.27 shows the calculated results under three different modulation schemes. The most significant difference among the EMI spectra is shown at switching frequency 20 kHz and its second harmonic, 40 kHz. SVM scheme gives the lowest noise peak amplitude at switching frequency compared to SPWM and DPWM scheme. In both SPWM and SVM schemes, the noise peak amplitude at the even harmonic of switching frequency is higher than that at the odd harmonics of switching frequency, which is not the case for DPWM scheme. In high frequency range, SVM gives the highest noise envelop and DPWM gives the lowest one. The difference between these two envelops is about 5dB. To validate the proposed modeling and calculation method, the high frequency noise produced by the inverter has to be measured. A set of LISNs are placed between the source and the inverter under test. Different PWM schemes are implemented by a digital signal processor (DSP) – ADMC 401™.

Fig. 3.28 shows experimental results of DM EMI spectrum under different PWM schemes. The calculated result using the frequency domain method matches the experimental result both in switching frequency range and in high frequency range very precisely. The experimental results show the same distinction of the EMI spectrum among different schemes as the calculated results. It is also indicated that the resonant points of the noise propagation path determine the location of the peak of the EMI spectrum, which is not related to modulation scheme.

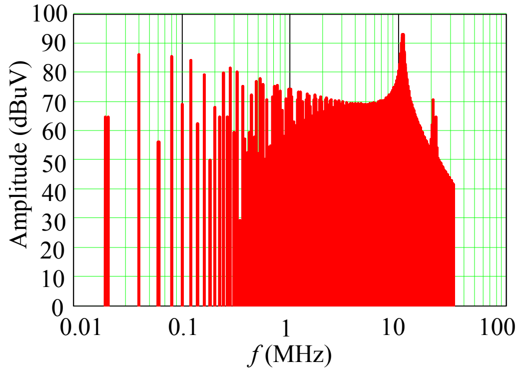

(A)

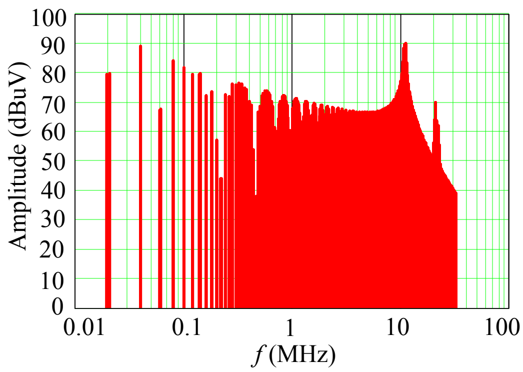

(B)

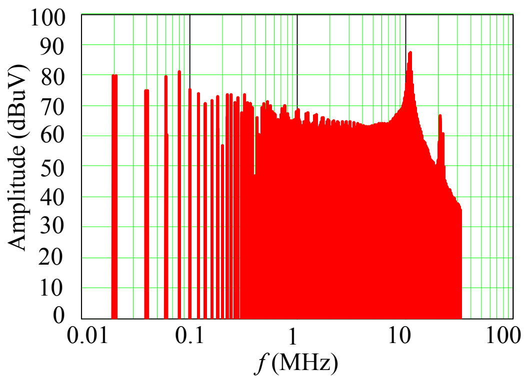

(c)

Fig. 3.27 Calculated DM EMI spectrum under different modulation Schemes (a) SVM (b) SPWM (c) DPWM

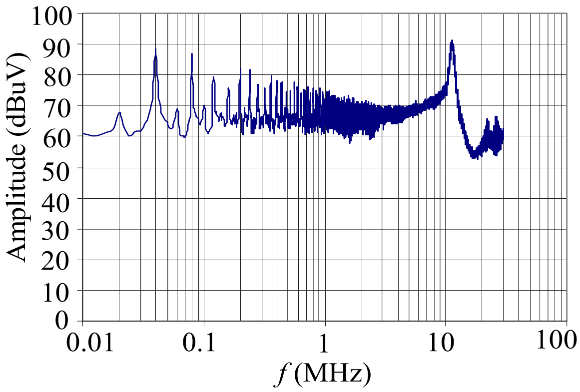

(A)

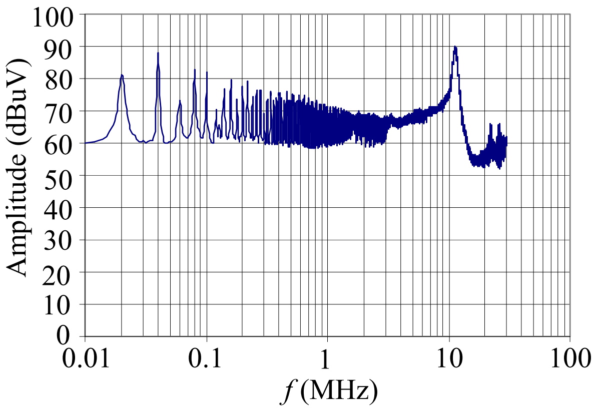

(B)

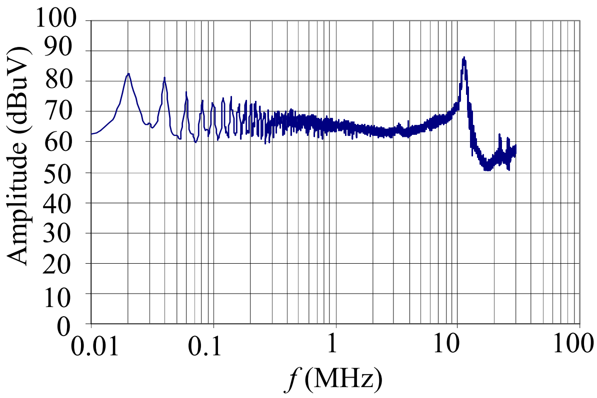

(C)

Fig. 3.28 Experimental results of DM EMI spectrum under different modulation Schemes

(a) SVM (b) SPWM (c) DPWM

3.7 Summary

A frequency domain approach to prediction of DM conducted EMI from three-phase inverter has been presented. This approach relies on identification of noise source based on inverter operation and extraction of parasitic parameters of the inverter components to predict the EMI currents produced in an inverter circuit. Methodologies for extraction of parasitic parameters of the inverter circuit are developed using finite element analysis. With accurate noise source and path models, the proposed "frequency-domain analysis" method avoids the computational problems in the conventional "time-domain analysis" and effectively predicts the DM EMI performance in high frequencies for an SVM based inverter.

The effect of different modulation schemes on DM EMI spectrum are evaluated through frequency domain method analytically. Different modulation scheme leads to different noise sources, which are represented in frequency domain respectively. The calculated results are verified through experiment test. But the noise path is generic, and its associated resonant frequency is the same regardless of the modulation scheme. The EMI performance, however, is highly affected by the modulation scheme both in the switching frequency related harmonic frequencies and in the noise path related resonant frequencies. In high frequency range, center-aligned PWM gives the highest noise envelop and DPWM gives lowest noise envelop. The DPWM has a significant portion running with zero duty, and thus overall producing lowest noise source in frequency domain including in high frequency regions where the EMI performance is mainly dominated by the noise path related impedance. The SVM, though, produces lowest peak

EMI amplitude at the switching frequency, with more than 10 dB reduction over the other two methods. This feature may be desirable when considering the design of EMI filters.

Chapter 4 CM Noise modeling and prediction for three phase inverter

The common mode (CM) EMI of motor drives has been an intensive research area of power electronics in recently years. Most researches were focusing on the common mode current generated by the motor side rather than by the inverter side. The inverter side can generate significant CM current due to the parasitic capacitance between the inverter and ground plane.

The frequency domain CM EMI prediction method was presented in Chapter 2. In this method, the CM noise source is determined as two parts, one is the switching characteristics such as dv/dt, and the other is parasitic ringing on the voltage waveform. The former part accounts for the noise up to MHz range, while the latter causes the noise up to tens of MHz range. To derive the noise source model of the first part, the PWM pattern should be considered. The interconnect parasitics and device parasitics should be included in the high frequency equivalent circuit in order to derive the noise source model of the second part. This method shows the appreciation of the fundamental mechanisms by which the CM EMI noises are excited and propagated. The CM EMI is dominated in the low-frequency region by the pulse-width-modulation (PWM) switching and the resonant peak in high frequency region is caused by the parasitic elements coupling with device switching dynamics in the EMI excitation.

This chapter attempts to predict the CM EMI of a three-phase inverter with complex PWM patterns along with the noise propagation path using the proposed modeling method. The inverter described in the previous chapter was used as the studied circuit. The three different noise source models based on three different modulation schemes, sinusoidal pulse width modulation (SPWM), SVM and bus-clamped discontinuous pulse width modulation (DPWM) are derived. The impact of modulation index on EMI spectrum is studied. Predictions with the proposed modeling method were performed for different modulation schemes and different modulation indexes, and the predicted results are compared with those from experiments. The results show that the modulation schemes have effects not only in switching frequency related harmonics, but also in high frequency range as well, while the modulation index mainly has its impact in switching frequency and its related harmonics range.

4.1 Introduction

The noise source and propagation path concept has to be used to obtain insightful analysis and modeling for the CM noise of three phase inverter system. The noise source is called common mode voltage that will be discussed in the following paragraph. The noise propagation path of a three phase inverter motor system is much more complicated than that of a single phase circuit because the system consists of inverter, AC output cable and motor. All the above elements have parasitic capacitance to the ground that can conduct leakage current. Besides, the parasitic capacitance and inductance of these elements in the motor drives system create multi-resonant peak in CM noise spectrum, which is difficult to characterize. To understand the resonance mechanism or noise propagation path, the system must be decomposed into several parts and studied separately. It is a common practice to divide the motor drive system into several subsystems such as inverter circuit, auxiliary power supply, AC output cable and motor. Each subsystem could contribute to the propagation of common mode noise. Much of past research on the path of common mode noise was focusing on the high frequency impedance from the motor and AC output cable, for instance, one research area that draws researcher's attention is the impedance of output cable connecting the inverter and motor. Reference [20] explained the long cable effect on CM mode voltage as a result of transmission line. However, the common mode noise path of inverter itself is not well studied due to the complexity of its operation. This chapter will focus on the common noise propagation by the inverter itself.

The previous studies of noise source [13,14], which is common mode source, were also concentrated on the high frequency current and CM mode voltage at the motor side. Fig. 4.1 shows the inverter motor drive system that includes three-phase inverter, AC output filter and motor. L_F is output filter inductance and R_F is output filter resistance. C_g is the stray capacitors between stator winding and motor frame, which conducts high frequency leakage current.

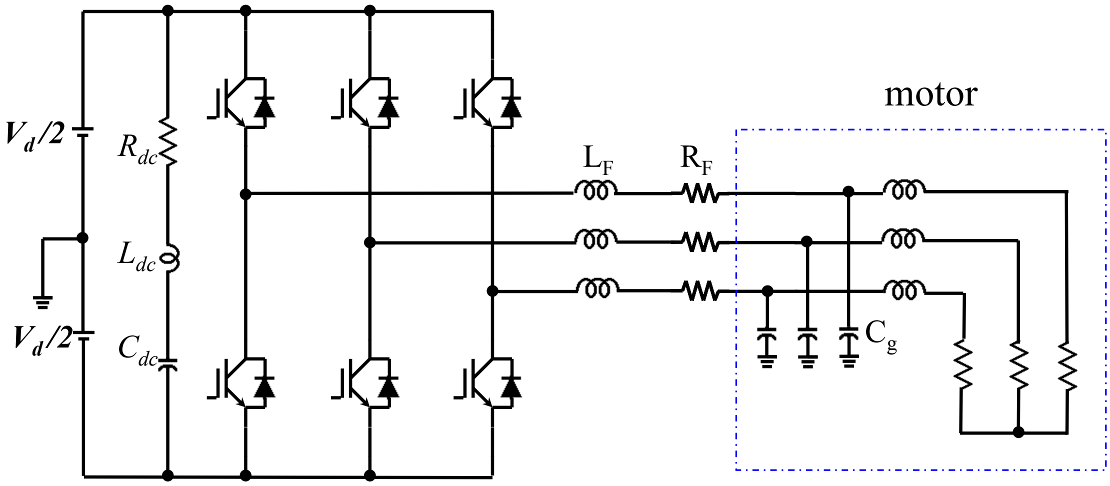

Fig. 4.1 Inverter motor system

This leakage current is caused by the step change of the common mode voltage produced by the PWM inverter switching action. The common mode voltage from motor side is given by

$$v_0 = \frac{v_a + v_b + v_c}{3} = \frac{S_a V_{dc} + S_b V_{dc} + S_c V_{dc}}{3} \qquad (4\text{-}1)$$

where v_a, v_b and v_c are the output voltages at the mid point of each phase. S_a, S_b and S_c are switching states for each phase, which is 1 when the top switch is on and is -1 when the bottom device is on.

Table 4.1 shows the value of v_a, v_b and v_c under each switching vector if the inverter is under SVM operation.

Table 4.1 v_a, v_b and v_c under each switching vector

	v_a	v_b	v_c
pnn	$V_d/2$	$-V_d/2$	$-V_d/2$
ppn	$V_d/2$	$V_d/2$	$-V_d/2$
ppp	$V_d/2$	$V_d/2$	$V_d/2$
npp	$-V_d/2$	$V_d/2$	$V_d/2$
npn	$-V_d/2$	$V_d/2$	$-V_d/2$
nnn	$-V_d/2$	$-V_d/2$	$-V_d/2$
nnp	$-V_d/2$	$-V_d/2$	$V_d/2$
pnn	$V_d/2$	$-V_d/2$	$-V_d/2$

Fig. 4.2 shows the common mode voltage v_0. It indicates that the common mode voltage changes $V_d/3$ for every switching instant.

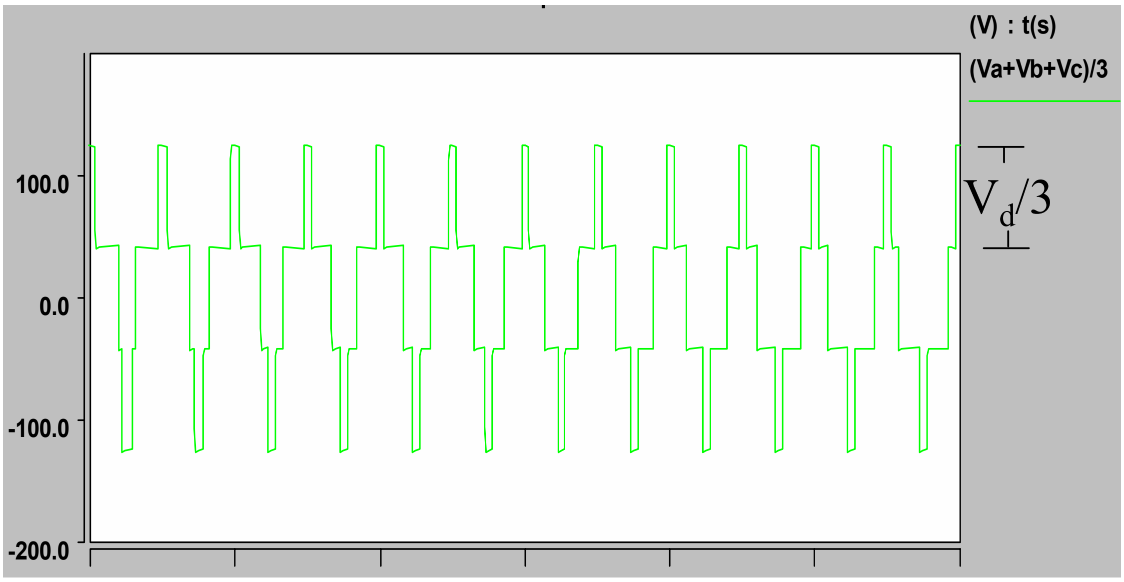

Fig. 4.2 Common mode voltage at motor side

Based on the common mode voltage at the motor side, an equivalent circuit was proposed in [13] that maps the measured impedance of output cable and motor. Fig. 4.3

shows the common mode equivalent circuit from the motor side. The noise source is approximated as a pulse train the amplitude of which is $V_{dc}/3$. Although this circuit provides some hints for the CM noise current, it lacks of details about CM noise generation and distribution. First, the noise current imposed by the common mode voltage at inverter side is neglected. Second, the noise source needs more analytically rigorous model considering the switching instant and control scheme, which indicates that more investigation should be done at inverter side. To avoid the interference from the motor side, the following research will focus on the inverter side to get the insightful analysis and modeling for the noise generated and propagated by the inverter itself.

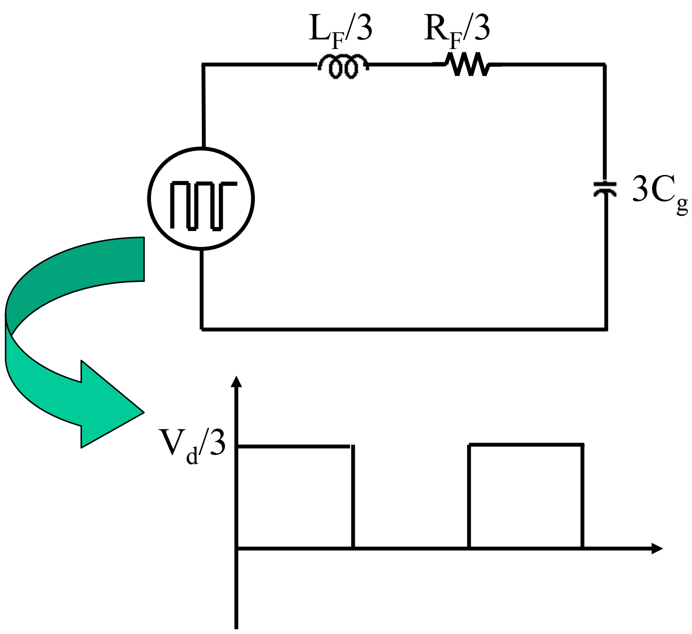

Fig. 4.3 Common mode equivalent circuit from motor side

4.2 Inverter common mode model-based on PWM switching

The research on CM voltage and high frequency leakage current is far from complete with regard to the noise source and noise propagation path determination from inverter side. First, the high frequency leakage current flowing through parasitic capacitance between the device and heatsink has to be taken in to account. Thus, from noise propagation path point of view, this parasitic capacitance should be included. Second, the noise source has to be thoroughly studied, considering the pulse width, switching instant and control scheme.

Fig. 4.4 shows the inverter circuit with lumped parasitic capacitances. The inverter circuit has distributed parasitic capacitances because the devices and components can be thought of having a capacitance to ground from each node. C_a, C_b and C_c are parasitic capacitances between the midpoint of each phase leg and ground. C_p is the parasitic capacitance between dc positive bus or negative bus and ground plane. Trying to calculate and include the effects of all these capacitances would be quite cumbersome, hence, it is necessary to identify the dominant parasitic capacitance.

Two factors have to be considered during the dominant parasitic capacitance. One is the size of the capacitance and the other is the magnitude variation of the voltage on that capacitance. In inverter circuit, a large capacitance to ground is the capacitance between device collector and heatsink. The device back plate which is connected to device collector is attached to the heatsink through soft, heat-conducting material that provides good thermal conduct. And also for safety reasons, this kind of soft, heat-conducting material needs to be electrically isolated. Parasitic capacitances associated with the insulation material will be generated between device collector and the heatsink. If this contact area is considered as a pair of parallel plates, the capacitance can be determined by

$$C = \varepsilon_r A / d \tag{4-2}$$

where A is the surface area of the device, and d is the thickness of the insulator. Therefore, if the surface area of the device is 2 cm^2 and the thickness of the insulator is 0.03 cm, the parasitic capacitance will be 30 pF. There are totally six devices in three phase inverter circuit, and each of them will have the same parasitic capacitance to ground. But for the three top devices, even with fairly large capacitances between their collectors to ground, since the voltage is near a constant of $V_{dc}/2$, there is a little effect on the common-mode EMI spectrum. Similarly for the negative dc bus or the emitter of the lower devices, the voltage is nearly constant, and its common mode EMI effect can be neglected. Hence, the dominant capacitance is the parasitic capacitance between the bottom device collectors and the heatsink. In other words, these are the capacitances between the midpoints of phase legs and the earth ground.

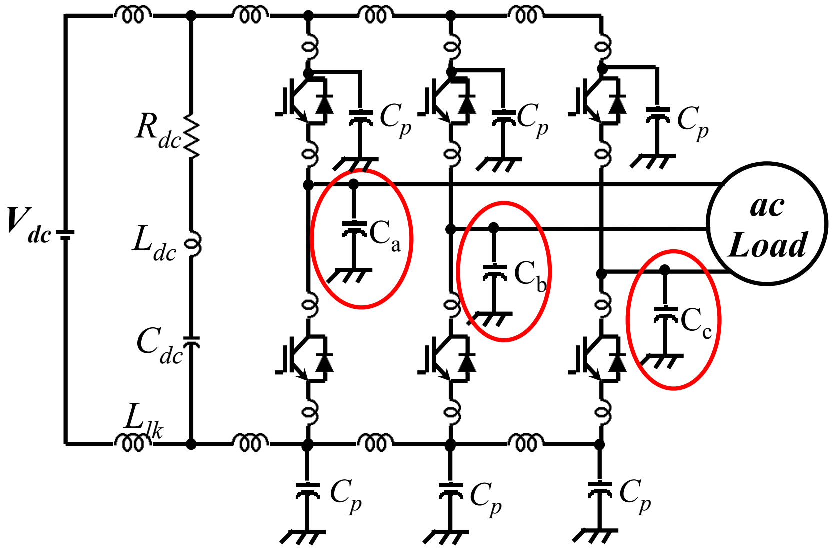

Fig. 4.4 Inverter Circuit with parasitic capacitance

In order to reduce complexity of the above circuit, a simplified model to predict CM EMI in switching frequency and its harmonics range is shown in Fig. 4.5. The parasitic inductance of device and DC bus, the parasitic capacitance C_p that is imposed by little voltage variation are all neglected. Only the dominant component of CM noise propagation path C_a, C_b and C_c is included. The noise source is determined as switching voltage, and S_a, S_b and S_c are 1 when the top device is on and -1 when the bottom device is on.

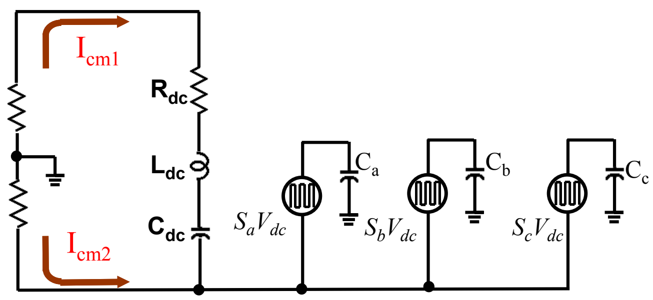

Fig. 4.5 Simplified CM model of inverter

If the parasitic capacitance between the midpoint of each phase leg and ground plane are identical, $C_a=C_b=C_c$, the simplified model can be reorganized to the circuit shown in Fig. 4.6. In this circuit, $C_{para}=C_a=C_b=C_c$. The CM noise source model V_n for the three phase inverter is given in

$$V_n = S_a V_{dc} + S_b V_{dc} + S_c V_{dc} \tag{4-3}$$

This common mode voltage source obtained from inverter side is three times of that derived from motor side as given in (4-1). The common mode voltage received across LISN is

$$V_{cm}(f) = \frac{V_n(f)}{Z(f)} \tag{4-4}$$

where, $V_n(f)$ is the frequency domain expression of V_n, and Z(f) is the transfer function of the noise propagation path shown in Fig. 4.6

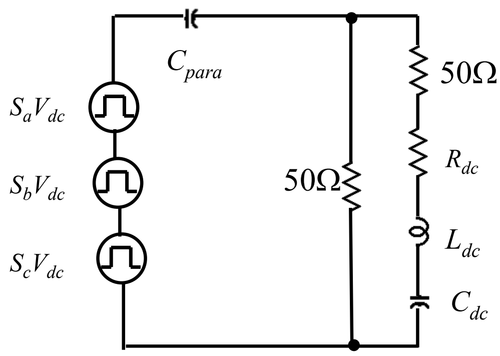

Fig. 4.6 Derived CM model of inverter

After the equivalent circuit is derived, the next step is to identify the frequency domain representation of the noise sources model, which is shown in the following section.

4.3 Common mode noise source model

The noise source model in (4-3) shows that it is a function of switching instant. Therefore the duty cycle of phase leg output voltage should be considered when deriving the noise source model. Unlike the duty cycle in the dc-dc converter, the duty cycle of inverter varies as a result of sinusoidal modulation. Fig. 4.7 shows the duty cycle waveform of the three phase inverter. It can be seen that the duty cycle varies from 0 to 1 during a fundamental line cycle. Although the switching waveform can still be approximated as trapezoidal waveform, the impact of duty on trapezoidal spectra has to be studied.

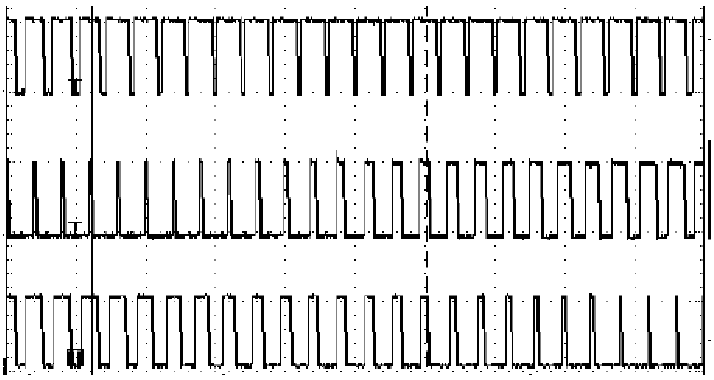

Fig. 4.7 Duty cycle waveform of the three phase inverter

4.3.1 Duty cycle effect on common mode source spectra

The frequency domain expression of trapezoidal waveform is given in

$$V_{trape} = 2A\frac{\tau}{T}\frac{\sin(n\pi \tau/T)}{n\pi \tau/T}\frac{\sin(n\pi t_f/T)}{n\pi t_f/T}, \tag{4-5}$$

which is the same as that given in Chapter 2. The duty cycle D is equal to τ/T. Considering two trapezoidal waveforms with different duty cycles, $0.5>D_1>D_2$, Fig. 4.8 shows the bounds of spectra of trapezoidal waveforms. It shows that the trapezoidal waveform with large duty cycle has higher bounds around switching frequency and its harmonics range than that with small duty cycle. While at high frequency ranges, the duty cycle effect disappears.

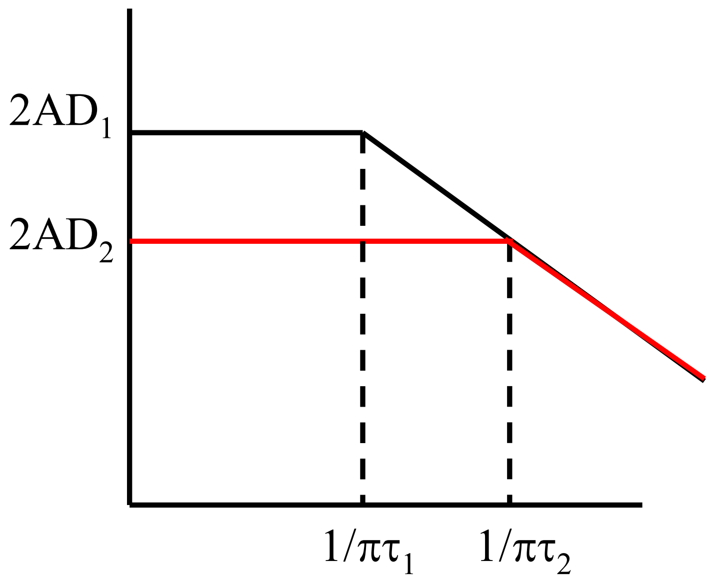

Fig. 4.8 The bounds of spectra of trapezoidal waveform with different duty

Fig. 4.9 shows the calculated spectra of the trapezoidal waveform under different duty cycles with the same frequency of 20kHz, and the effect of duty cycle for switching frequency and its harmonics range is well illustrated.

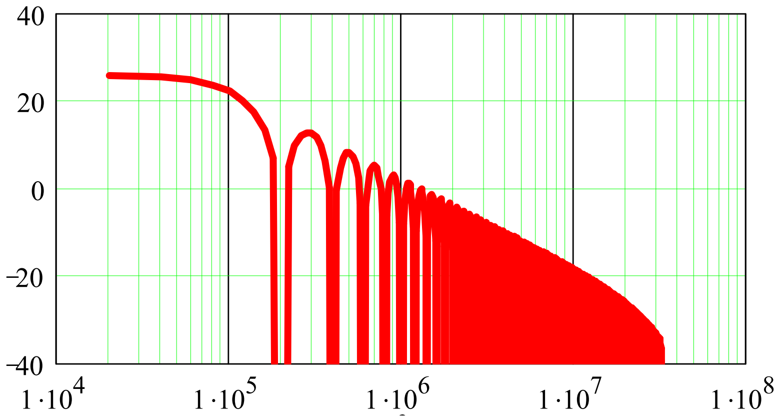

(a) d=0.1

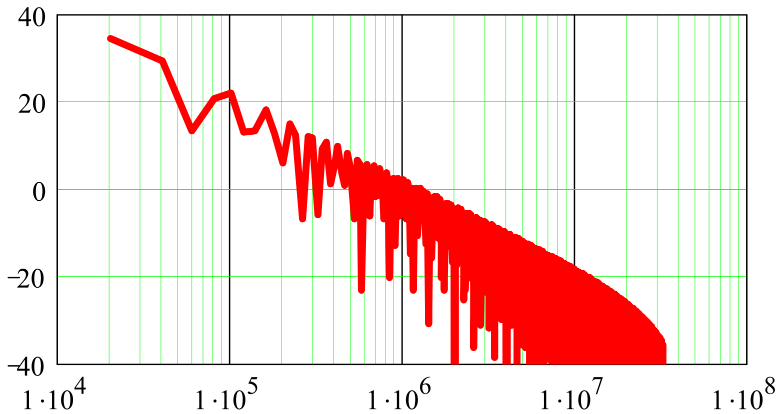

(b) d=0.3

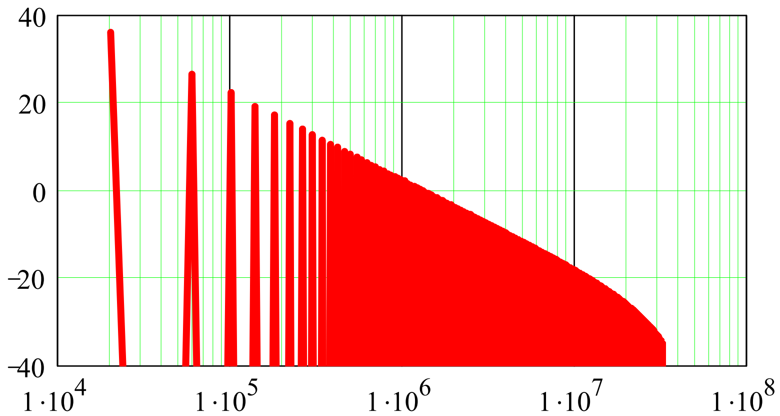

(c) d=0.5

Fig. 4.9 Frequency spectra of trapezoidal waveform with different duty cycles

The previous research [14] that regards the common mode noise source of three phase inverter as a trapezoid waveform with fixed duty cycle is not rigorous enough to predict common mode EMI noise in frequency domain. This is an area that needs to be explored to achieve reasonable accuracy in the predicted result.

4.3.2 Common mode noise source model under different PWM schemes

The frequency and amplitude of the common mode noise source is critical for common mode EMI modeling and prediction. As has been pointed out above, when the voltage at the midpoint changes from $+V_{dc}/2$ to $-V_{dc}/2$, the duty within each switching period varies based on sinusoidal function. The frequency domain representation for this voltage under a fundamental line cycle can be achieved by applying the double integral Fourier form. The double integral Fourier form applied to voltage at the midpoint of each phase leg is given in (4-6).

$$C_{mn} = A_{mn} + jB_{mn} = \frac{1}{2\pi^2}\int_{y_s}^{y_e}\int_{x_r}^{x_f} V_{dc}\ell^{-j(m\omega_S t + n\omega_0 t)} d(\omega_s t) d(\omega_0 t) \qquad (4\text{-}6)$$

This equation can be considered as the common mode noise source model for each phase leg. Here V_{dc} is the voltage across the dc bus, ω_s is switching frequency, ω_0 is fundamental frequency. The outer integral limit y_e, y_r and inner integral limit x_r, x_f are determined by the modulation scheme. Thus, it indicates that the modulation scheme has impact on the frequency and amplitude of the common model noise source model.

It has been demonstrated in Chapter 3 that the differential mode EMI noise source model changes within the witching frequency and its harmonics range under different modulation schemes, which leads to variance in DM EMI spectrum. Moreover, the discontinuous PWM method shows even lower DM EMI noise envelop in high frequency range than continuous PWM method as the result of less switching action. In this chapter, the effect of different modulation scheme on CM noise source model plus CM EMI spectrum will be investigated.

Two classes of modulation schemes, continuous PWM and discontinuous PWM method, are studied. The chosen continuous PWM methods are the common SPWM and center-aligned SVM. These are always switching actions occurring for each phase leg during a switching cycle, which indicates the voltage at the midpoint of the phase leg changes during each switching cycle. This causes the leakage current going through the parasitic capacitance between the midpoint and ground phase during each switching action. In discontinuous PWM method a phase has a period of at most one third of the fundamental cycle during which the output voltage of this phase is clamped to either positive dc bus rail or negative dc bus rail. Less switching action will lead to less leakage current going through the parasitic capacitance, thus, reduce the CM noise. It is interesting to quantify the improvement on DPWM method compared to SPWM and center-aligned SVM method. In this chapter, three PWM methods, SPWM, SVM and DPWM, will be discussed. It is noted that there are other DPWM schemes; however the result can be extended to other DPWM methods although only one of DPWM methods is discussed here.

A. SPWM

In the conventional SPWM method, the duty cycle function of the top switch of three phases can be represented in (4-7). The differences among three phases are 120° phase shifts.

$$
\begin{aligned}
d_a(\omega_0 t) &= \frac{1}{2}(1 + M\cos(\omega_0 t)) \\
d_b(\omega_0 t) &= \frac{1}{2}(1 + M\cos(\omega_0 t - \frac{2\pi}{3})) \\
d_c(\omega_0 t) &= \frac{1}{2}(1 + M\cos(\omega_0 t - \frac{4\pi}{3}))
\end{aligned}
\tag{4-7}
$$

The noise source model under SPWM method can be obtained from double integral Fourier form applied to voltage at the midpoint of each leg, and the noise source model for phase A is shown in (4-8).

$$
\begin{aligned}
C_{avmn} &= \frac{1}{2\pi^2}\int_0^{2\pi}\int_{-\frac{\pi}{2}(1+M\cos(\omega_0 t))}^{\frac{\pi}{2}(1+M\cos(\omega_0 t))} V_{dc}\,\ell^{-j(m\omega_s t+n\omega_0 t)}\,d(\omega_s t)d(\omega_0 t) \\
&= \frac{V_{dc}}{2\pi^2 m}\int_0^{2\pi}\ell^{-j(n\omega_0 t)}(\ell^{j(m\frac{\pi}{2}(1+M\cos(\omega_0 t)))} - \ell^{-j(m\frac{\pi}{2}(1+M\cos(\omega_0 t)))})d(\omega_0 t) \\
&= \frac{V_{dc}}{2\pi^2 m}\int_0^{2\pi}\ell^{-j(n\omega_0 t)}(\ell^{jm\frac{\pi}{2}}\ell^{jm\frac{\pi}{2}M\cos(\omega_0 t)} - \ell^{-jm\frac{\pi}{2}}\ell^{-jm\frac{\pi}{2}M\cos(\omega_0 t)})d(\omega_0 t)
\end{aligned}
\tag{4-8}
$$

The close form solution of (4-9) can be obtained by applying Jacobi-Anger expansion [74] of $\ell^{\pm j(\alpha\cos(\omega_0 t)))}$, which is

$$
\ell^{\pm j(\alpha\cos(\omega_0 t)))} = J_0(\alpha) + 2\sum_{k=1}^{\infty} j^{\pm k} J_k(\alpha)\cos(ky)
\tag{4-9}
$$

Substituting (4-9) into (4-8), the noise source model of phase A can be changed and simplified to

$$C_{avmn}=\frac{V_{dc}}{\pi^2 m}\int_0^{2\pi}\ell^{-j(n\omega_0 t)}(\sin(m\frac{\pi}{2})J_0(m\frac{\pi}{2}M)+2\sum_{k=1}^{\infty}\sin((m+k)\frac{\pi}{2})J_k(m\frac{\pi}{2}M)\cos(k\omega_0 t))d(\omega_0 t) \quad \text{(4-10)}$$

Applying the same principle, the noise source model of phase B and phase C can be derived and simplified to (4-11), (4-12).

$$C_{bvmn}=\frac{1}{2\pi^2}\int_0^{2\pi}\int_{-\frac{\pi}{2}(1+M\cos(\omega_0 t-2\pi/3))}^{\frac{\pi}{2}(1+M\cos(\omega_0 t-2\pi/3))}V_{dc}\ell^{-j(m\omega_S t+n\omega_0 t)}d(\omega_s t)d(\omega_0 t)$$
$$=\frac{V_{dc}}{\pi^2 m}\int_0^{2\pi}\ell^{-j(n\omega_0 t)}(\sin(m\frac{\pi}{2})J_0(m\frac{\pi}{2}M)+2\sum_{k=1}^{\infty}\sin((m+k)\frac{\pi}{2})J_k(m\frac{\pi}{2}M)\cos(k(\omega_0 t-\frac{2\pi}{3})))d(\omega_0 t) \quad \text{(4-11)}$$

$$C_{cvmn}=\frac{1}{2\pi^2}\int_0^{2\pi}\int_{-\frac{\pi}{2}(1+M\cos(\omega_0 t-4\pi/3))}^{\frac{\pi}{2}(1+M\cos(\omega_0 t-4\pi/3))}V_{dc}\ell^{-j(m\omega_S t+n\omega_0 t)}d(\omega_s t)d(\omega_0 t)$$
$$=\frac{V_{dc}}{\pi^2 m}\int_0^{2\pi}\ell^{-j(n\omega_0 t)}(\sin(m\frac{\pi}{2})J_0(m\frac{\pi}{2}M)+2\sum_{k=1}^{\infty}\sin((m+k)\frac{\pi}{2})J_k(m\frac{\pi}{2}M)\cos(k(\omega_0 t-\frac{4\pi}{3})))d(\omega_0 t) \quad \text{(4-12)}$$

The sum of the noise source models of each phase is given in (4-13)

$$C_{vmn}=\sum_{k=a,b,c}C_{kvmn} \quad \text{(4-13)}$$

Substituting (4-10), (4-11) and (4-12) into (4-13) gives

$$C_{vmn}=\frac{V_{dc}}{\pi^2 m}\int_0^{2\pi}\ell^{-j(n\omega_0 t)}(3\sin(m\frac{\pi}{2})J_0(m\frac{\pi}{2}M)+2\sum_{k=1}^{\infty}\sin((m+k)\frac{\pi}{2})J_k(m\frac{\pi}{2}M)A_k)d(\omega_0 t) \quad \text{(4-14)}$$

, where

$$A_k=\cos(k\omega_0 t)+\cos(k(\omega_0 t-\frac{4\pi}{3}))+\cos(k(\omega_0 t-\frac{4\pi}{3})) \quad \text{(4-15)}$$

The solution of (4-15) is given in (4-16)

$$A_k=\begin{cases}3\cos(k\omega_0 t),\ k=3p, 1\le p\le\infty\\ 0, k\ne 3p, 1\le p\le\infty\end{cases} \quad \text{(4-16)}$$

Therefore, (4-14) can be simplified to

$$C_{vmn} = \frac{V_{dc}}{\pi^2 m}\int_0^{2\pi} \ell^{-j(n\omega_0 t)}(3\sin(m\frac{\pi}{2})J_0(m\frac{\pi}{2}M) + 6\sum_{p=1}^{\infty}\sin((m+3p)\frac{\pi}{2})J_{3p}(m\frac{\pi}{2}M)\cos(3p\omega_0 t))d(\omega_0 t) \tag{4-17}$$

It is indicated that only when $|n| = 3p$, the second term of (4-17) will not be zero. Hence, the common mode noise source model under SPWM can be derived as

$$C_{vmn} = \frac{6V_{dc}}{\pi m}\sin((m+n)\frac{\pi}{2})J_n(m\frac{\pi}{2}M),\ n = 3p, -\infty \le p \le \infty \tag{4-18}$$

It can be seen from (4-18) that the common model noise source model of three phase inverter under SPWM control scheme is the function of the DC bus voltage, modulation index and the multiples of carrier frequency and the triple multiples of fundamental frequency. If the sideband effect is not taken into account, which means that *n=0,* (4-18) can be simplified to

$$C_{vm0} = \frac{6V_{dc}}{\pi m}\sin(m\frac{\pi}{2})J_0(m\frac{\pi}{2}M) \tag{4-19}$$

, which gives non-zero solution only when m is odd number. This is different from the discussion for DM noise source model as shown in Chapter 3, which gives non-zero solution only when m is even number.

Both (4-18) and (4-19) shows modulation index M as the parameter of the Bessel function, hence, the variation of M will cause the changes of amplitude of CM mode EMI source model plus CM EMI spectrum. It is interesting to investigate the trend of the amplitude of CM noise source model following the change of modulation index.

Fig. 4.10 illustrates the CM noise source model for all three phases under SPWM method at switching frequency (20 kHz) and its harmonics range. Note that the side band effect is considered. The modulation index varies from 0.1 to 0.75. When M is 0.1 the peaks mainly occur at switching frequency 20kHz, and its odd harmonics, as the modulation index increases, the sideband effect appears around the even harmonics of switching frequency. The amplitude at switching frequency is highest when M is 0.1. And it drops as the modulation index increases. There is about 5dB difference between the amplitude under 0.1 and that under 0.75. Besides, the noise source envelop within 1 MHz range is highest when M is 0.1 and it drops about 5 dB as the modulation index increases to 0.75.

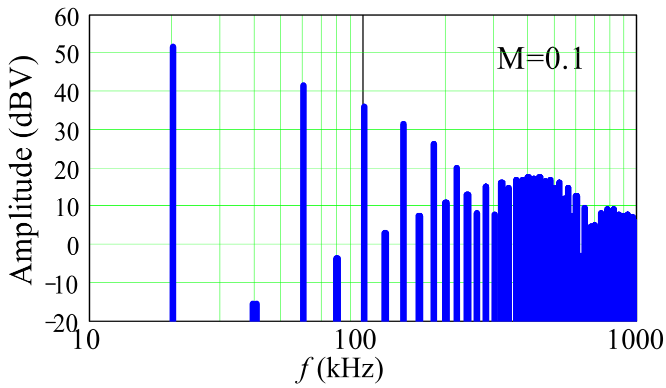

(a) M=0.1

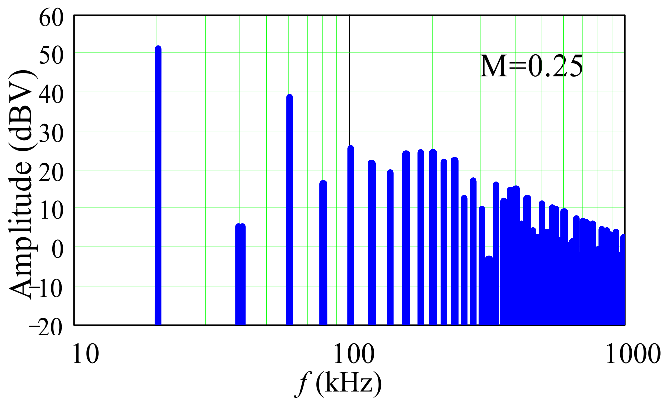

(b) M=0.25

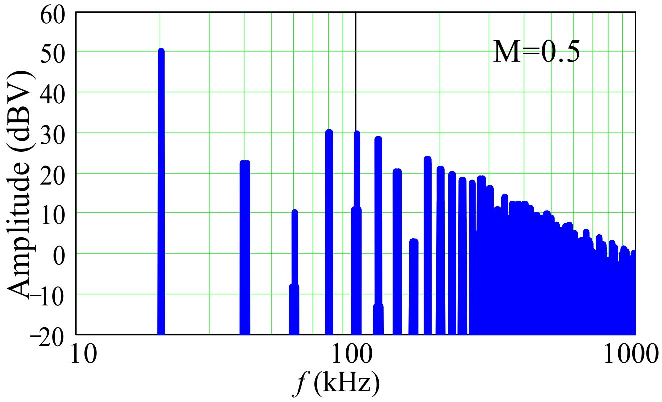

(c) M=0.5

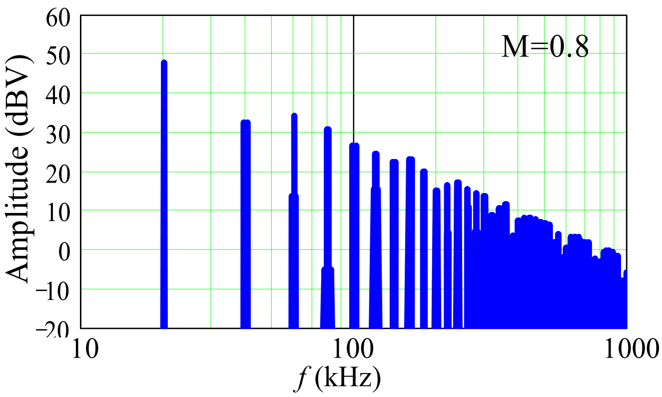

(d) M=0.75

Fig. 4.10 CM noise source model under SPWM with different modulation index

B. SVM

Another continuous PWM scheme discussed here is the center-aligned SVM method that was obtained by averaging the duty cycle over two consecutive switching states. Its effect on DM noise source model and DM EMI spectrum was presented the previous chapter. For the derivation of frequency domain expression of CM noise source model, the same technique can be applied. (4-6) is still the fundamental principle to apply except that the inner integral limit and the outer integral limit have to be selected properly based on SVM scheme. As was presented the above, the out integral limit is determine by sector region and the inner integral limit is determined by the duty cycle function of top switch of each phase leg in each sector region. The phase-a top switch duty cycle function is described in (4-20). The duty cycle functions of phase b and phase C are 2π/3 and 4π/3 phase shift of that of phase a respectively, which are given in (4-21).

$$d_a(\omega_0 t) = \begin{cases} \frac{1}{2}(1 + M\cos(\omega_0 t - \frac{\pi}{6})) & if\ \ 0 < \omega_0 t < \frac{\pi}{3} \\ \frac{1}{2}(1 + \sqrt{3}M\cos(\omega_0 t)) & if\ \ \frac{\pi}{3} < \omega_0 t < \frac{2\pi}{3} \\ \frac{1}{2}(1 + M\cos(\omega_0 t + \frac{\pi}{6})) & if\ \ \frac{2\pi}{3} < \omega_0 t < \pi \\ \frac{1}{2}(1 + M\cos(\omega_0 t - \frac{\pi}{6})) & if\ \ \pi < \omega_0 t < \frac{4\pi}{3} \\ \frac{1}{2}(1 + \sqrt{3}M\cos(\omega_0 t)) & if\ \ \frac{4\pi}{3} < \omega_0 t < \frac{5\pi}{3} \\ \frac{1}{2}(1 + M\cos(\omega_0 t + \frac{\pi}{6})) & if\ \ \frac{5\pi}{3} < \omega_0 t < 2\pi \end{cases} \tag{4-20}$$

$$\begin{aligned} d_b(\omega_0 t) &= d_a(\omega_0 t - \frac{2\pi}{3}) \\ d_c(\omega_0 t) &= d_a(\omega_0 t - \frac{4\pi}{3}) \end{aligned} \tag{4-21}$$

The noise source model for each sector under SVM method can be obtained from double integral Fourier form applied to midpoint voltage of phase leg. For instance, (4-22) shows double integral Fourier form applied to midpoint voltage of phase A in sector I by substituting the outer integral with the boundary of the sector region and the inner integral limit with the duty cycle function.

$$C_{mnI} = \frac{1}{2\pi^2}\int_0^{\frac{\pi}{3}}\int_{-\frac{\pi}{2}(1+M\cos(\omega_0 t-\frac{\pi}{6}))}^{\frac{\pi}{2}(1+M\cos(\omega_0 t-\frac{\pi}{6}))} V_{dc}\ell^{-j(m\omega_s t+n\omega_0 t)}d(\omega_s t)d(\omega_0 t)$$

$$= \frac{V_{dc}}{2\pi^2 m}\int_0^{\frac{\pi}{3}}\ell^{-jn\omega_0 t}\left(\ell^{j(m\frac{\pi}{2}(1+M\cos(\omega_0 t-\frac{\pi}{6})))} - \ell^{-j(m\frac{\pi}{2}(1+M\cos(\omega_0 t-\frac{\pi}{6})))}\right)d(\omega_0 t) \qquad (4\text{-}22)$$

The noise source model for a fundamental cycle can be given by adding the noise source model under each sector together as shown in (4-23) and (4-24) shows noise source model for phase A for a fundamental cycle.

$$C_{mn} = \sum_{k=I}^{VI} C_{mnk} \qquad (4\text{-}23)$$

$$\begin{aligned}
C_{amn} &= \frac{1}{2\pi^2}\int_0^{\frac{\pi}{3}}\int_{-\frac{\pi}{2}(1+M\cos(\omega_0 t-\frac{\pi}{6}))}^{\frac{\pi}{2}(1+M\cos(\omega_0 t-\frac{\pi}{6}))} V_{dc}\ell^{-j(m\omega_s t+n\omega_0 t)}d(\omega_s t)d(\omega_0 t) \\
&+ \frac{1}{2\pi^2}\int_{\frac{\pi}{3}}^{\frac{2\pi}{3}}\int_{-\frac{\pi}{2}(1+\sqrt{3}M\cos(\omega_0 t))}^{\frac{\pi}{2}(1+\sqrt{3}M\cos(\omega_0 t))} V_{dc}\ell^{-j(m\omega_s t+n\omega_0 t)}d(\omega_s t)d(\omega_0 t) \\
&+ \frac{1}{2\pi^2}\int_{\frac{2\pi}{3}}^{\pi}\int_{-\frac{\pi}{2}(1+M\cos(\omega_0 t+\frac{\pi}{6}))}^{\frac{\pi}{2}(1+M\cos(\omega_0 t+\frac{\pi}{6}))} V_{dc}\ell^{-j(m\omega_s t+n\omega_0 t)}d(\omega_s t)d(\omega_0 t) + \\
&\frac{1}{2\pi^2}\int_{\pi}^{\frac{4\pi}{3}}\int_{-\frac{\pi}{2}(1+M\cos(\omega_0 t-\frac{\pi}{6}))}^{\frac{\pi}{2}(1+M\cos(\omega_0 t-\frac{\pi}{6}))} V_{dc}\ell^{-j(m\omega_s t+n\omega_0 t)}d(\omega_s t)d(\omega_0 t) + \\
&\frac{1}{2\pi^2}\int_{\frac{4\pi}{3}}^{\frac{5\pi}{3}}\int_{-\frac{\pi}{2}(1+\sqrt{3}M\cos(\omega_0 t))}^{\frac{\pi}{2}(1+\sqrt{3}M\cos(\omega_0 t))} V_{dc}\ell^{-j(m\omega_s t+n\omega_0 t)}d(\omega_s t)d(\omega_0 t) + \\
&\frac{1}{2\pi^2}\int_{\frac{5\pi}{3}}^{2\pi}\int_{-\frac{\pi}{2}(1+M\cos(\omega_0 t+\frac{\pi}{6}))}^{\frac{\pi}{2}(1+M\cos(\omega_0 t+\frac{\pi}{6}))} V_{dc}\ell^{-j(m\omega_s t+n\omega_0 t)}d(\omega_s t)d(\omega_0 t)
\end{aligned} \qquad (4\text{-}24)$$

The sum of the noise source model can be calculated as (4-13) and be simplified to

$$
\begin{aligned}
C_{vmn} &= \frac{V_{dc}}{\pi^2 m}\int_0^{\frac{\pi}{3}} \ell^{-j(n\omega_0 t)}(3\sin(m\frac{\pi}{2})J_0(m\frac{\pi}{2}M)+6\sum_{p=1}^{\infty}\sin((m+3p)\frac{\pi}{2})J_{3p}(m\frac{\pi}{2}M)\cos(3p(\omega_0 t-\frac{\pi}{6})))d(\omega_0 t)\\
&+\frac{V_{dc}}{\pi^2 m}\int_{\frac{\pi}{3}}^{\frac{2\pi}{3}} \ell^{-j(n\omega_0 t)}(3\sin(m\frac{\pi}{2})J_0(\sqrt{3}m\frac{\pi}{2}M)+6\sum_{p=1}^{\infty}\sin((m+3p)\frac{\pi}{2})J_{3p}(\sqrt{3}m\frac{\pi}{2}M)\cos(3p\omega_0 t))d(\omega_0 t)\\
&+\frac{V_{dc}}{\pi^2 m}\int_{\frac{2\pi}{3}}^{\pi} \ell^{-j(n\omega_0 t)}(3\sin(m\frac{\pi}{2})J_0(m\frac{\pi}{2}M)+6\sum_{p=1}^{\infty}\sin((m+3p)\frac{\pi}{2})J_{3p}(m\frac{\pi}{2}M)\cos(3p(\omega_0 t+\frac{\pi}{6})))d(\omega_0 t)\\
&+\frac{V_{dc}}{\pi^2 m}\int_{\pi}^{\frac{4\pi}{3}} \ell^{-j(n\omega_0 t)}(3\sin(m\frac{\pi}{2})J_0(m\frac{\pi}{2}M)+6\sum_{p=1}^{\infty}\sin((m+3p)\frac{\pi}{2})J_{3p}(m\frac{\pi}{2}M)\cos(3p(\omega_0 t-\frac{\pi}{6})))d(\omega_0 t)\\
&+\frac{V_{dc}}{\pi^2 m}\int_{\frac{4\pi}{3}}^{\frac{5\pi}{3}} \ell^{-j(n\omega_0 t)}(3\sin(m\frac{\pi}{2})J_0(\sqrt{3}m\frac{\pi}{2}M)+6\sum_{p=1}^{\infty}\sin((m+3p)\frac{\pi}{2})J_{3p}(\sqrt{3}m\frac{\pi}{2}M)\cos(3p\omega_0 t))d(\omega_0 t)\\
&+\frac{V_{dc}}{\pi^2 m}\int_{\frac{5\pi}{3}}^{2\pi} \ell^{-j(n\omega_0 t)}(3\sin(m\frac{\pi}{2})J_0(m\frac{\pi}{2}M)+6\sum_{p=1}^{\infty}\sin((m+3p)\frac{\pi}{2})J_{3p}(m\frac{\pi}{2}M)\cos(3p(\omega_0 t+\frac{\pi}{6})))d(\omega_0 t)
\end{aligned}
\tag{4-25}
$$

Although (4-25) can not be simplified as elegant as (4-18) under SPWM method, it can be seen that the common model noise source model of three phase inverter under SVM control scheme is the function of the DC bus voltage, modulation index and the multiples of carrier frequency and the triple multiples of fundamental frequency.

Fig. 4.11 illustrates the CM noise source model for all three phases under SVM method at switching frequency (20 kHz) and its harmonics range with the consideration of sideband effect. The modulation index varies from 0.1 to 0.75. When M is 0.1 the peaks mainly occur at switching frequency 20kHz, and its odd harmonics, as the modulation index increases, the sideband effect appears around the even harmonics of switching frequency. The amplitude at switching frequency is highest when M is 0.1 and it drops about 5 dB as the modulation index increases to 0.75. Besides, the noise source envelop within 1 MHz range is highest when M is 0.1 and as the modulation index increases, there is about 5dB difference between the amplitude under 0.1 and that under 0.75.

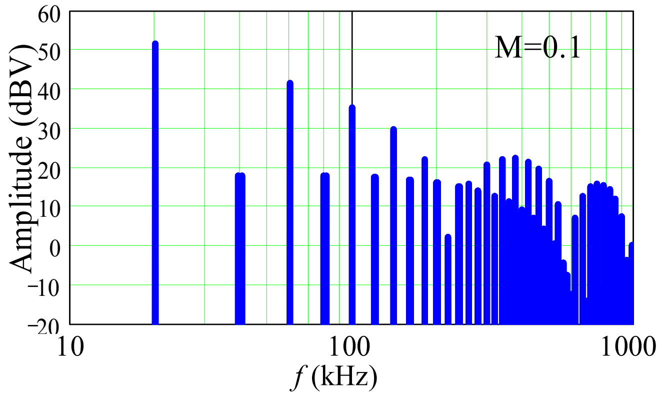

(a) M=0.1

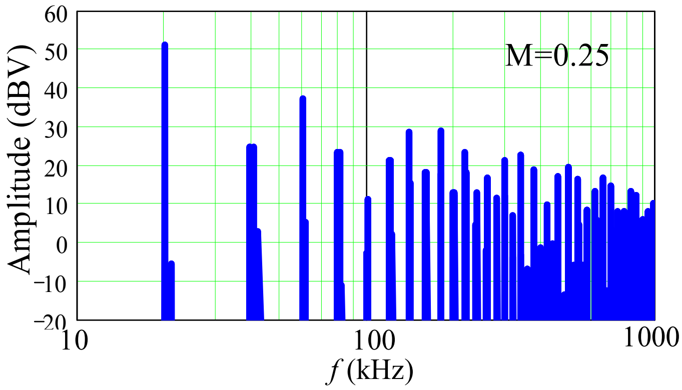

(b) M=0.25

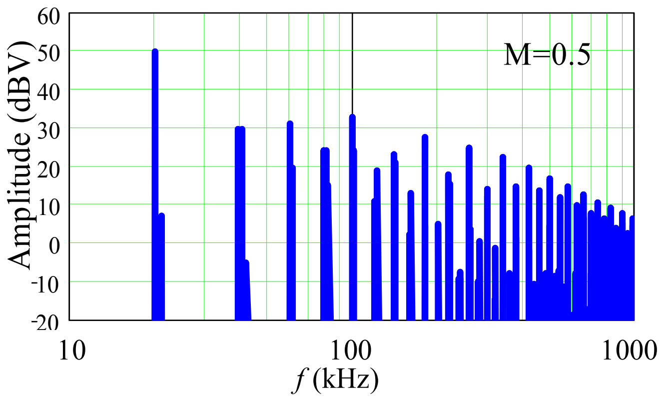

(c) M=0.5

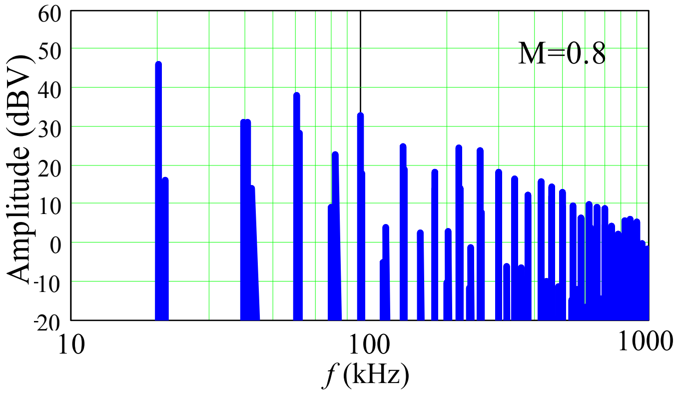

(d) M=0.75

Fig. 4.11 CM noise source model under SVM with different modulation index

C. DPWM

The DPWM scheme was found on the principle that discontinuous modulation waves was developed using a discontinuous type of zero-sequence signal. Since during each carrier cycle one phase ceases modulation, the associated phase is clamped to the positive or negative dc rail, the total number of switching action for a fundamental cycle is reduced. This leads to less switching losses and lower DM EMI spectrum as presented in Chapter 3. However, its impact on CM EMI spectrum has not been explored before. It is interesting to investigate and quantify its impact on CM mode EMI spectrum. Although there are several different DPWM scheme, only DPWM method is chosen for study. The duty cycle function of three phase leg under this method is described by (4-26).

$$d_a(\omega_0 t)=\begin{cases}1 \;\; if \;\; 0<\omega_0 t<\frac{\pi}{3}\\ M\cos(\omega_0 t-\frac{\pi}{6}) \;\; if \;\; \frac{\pi}{3}<\omega_0 t<\frac{2\pi}{3}\\ 1+M\cos(\omega_0 t+\frac{\pi}{6}) \;\; if \;\; \frac{2\pi}{3}<\omega_0 t<\pi\\ 0 \;\; if \;\; \pi<\omega_0 t<\frac{4\pi}{3}\\ M\cos(\omega_0 t-\frac{\pi}{6}) \;\; if \;\; \frac{4\pi}{3}<\omega_0 t<\frac{5\pi}{3}\\ 1+M\cos(\omega_0 t+\frac{\pi}{6}) \;\; if \;\; \frac{5\pi}{3}<\omega_0 t<2\pi\end{cases} \qquad d_b(\omega_0 t)=\begin{cases}1+M\cos(\omega_0 t-\frac{5\pi}{6}) \;\; if \;\; 0<\omega_0 t<\frac{\pi}{3}\\ M\sin(\omega_0 t) \;\; if \;\; \frac{\pi}{3}<\omega_0 t<\frac{2\pi}{3}\\ 1 \;\; if \;\; \frac{2\pi}{3}<\omega_0 t<\pi\\ M\cos(\omega_0 t-\frac{5\pi}{6}) \;\; if \;\; \pi<\omega_0 t<\frac{4\pi}{3}\\ 0 \;\; if \;\; \frac{4\pi}{3}<\omega_0 t<\frac{5\pi}{3}\\ 1+M\cos(\omega_0 t-\frac{5\pi}{6}) \;\; if \;\; \frac{5\pi}{3}<\omega_0 t<2\pi\end{cases}$$

$$d_c(\omega_0 t)=\begin{cases}1-M\cos(\omega_0 t-\frac{\pi}{6}) \;\; if \;\; 0<\omega_0 t<\frac{\pi}{3}\\ 0 \;\; if \;\; \frac{\pi}{3}<\omega_0 t<\frac{2\pi}{3}\\ 1-M\sin(\omega_0 t) \;\; if \;\; \frac{2\pi}{3}<\omega_0 t<\pi\\ -M\cos(\omega_0 t-\frac{\pi}{6}) \;\; if \;\; \pi<\omega_0 t<\frac{4\pi}{3}\\ 1 \;\; if \;\; \frac{4\pi}{3}<\omega_0 t<\frac{5\pi}{3}\\ -M\sin(\omega_0 t) \;\; if \;\; \frac{5\pi}{3}<\omega_0 t<2\pi\end{cases} \tag{4-26}$$

The noise source model under DPWM method can be obtained from double integral Fourier form applied to voltage at midpoint of each phase leg, which is a function of the duty cycle and sector region. Substituting the outer integral and inner integral in (4-6) with duty cycle function and sector region given in (4-26) derives the double integral Fourier form for each sector region. Adding the noise source model under each sector together gives the noise source model under a fundamental cycle, which is expressed in (4-27) for phase A.

$$\begin{aligned}C_{amn}&=\frac{1}{2\pi^2}\int_{\frac{\pi}{3}}^{\frac{2\pi}{3}}\int_{-\pi M\cos(\omega_0 t-\frac{\pi}{6})}^{\pi M\cos(\omega_0 t-\frac{\pi}{6})} V_{dc}\ell^{-j(m\omega_S t+n\omega_0 t)}d(\omega_s t)d(\omega_0 t)\\&+\frac{1}{2\pi^2}\int_{\frac{2\pi}{3}}^{\pi}\int_{-\pi(1+M\cos(\omega_0 t+\frac{\pi}{6}))}^{\pi(1+M\cos(\omega_0 t+\frac{\pi}{6}))} V_{dc}\ell^{-j(m\omega_S t+n\omega_0 t)}d(\omega_s t)d(\omega_0 t)+\\&\frac{1}{2\pi^2}\int_{\frac{4\pi}{3}}^{\frac{5\pi}{3}}\int_{-\pi M\cos(\omega_0 t-\frac{\pi}{6})}^{\pi M\cos(\omega_0 t-\frac{\pi}{6})} V_{dc}\ell^{-j(m\omega_S t+n\omega_0 t)}d(\omega_s t)d(\omega_0 t)+\\&\frac{1}{2\pi^2}\int_{\frac{5\pi}{3}}^{2\pi}\int_{-\pi(1+M\cos(\omega_0 t+\frac{\pi}{6}))}^{\pi(1+M\cos(\omega_0 t+\frac{\pi}{6}))} V_{dc}\ell^{-j(m\omega_S t+n\omega_0 t)}d(\omega_s t)d(\omega_0 t)\end{aligned} \tag{4-27}$$

By solving the inner integral, (4-27) can be simplified to

$$C_{amn} = \frac{1}{2\pi^2}\int_{\frac{\pi}{3}}^{\frac{2\pi}{3}} \ell^{-jn\omega_0 t}(\ell^{j(m\pi(M\cos(\omega_0 t-\frac{\pi}{6})))} - \ell^{-j(m\pi(M\cos(\omega_0 t-\frac{\pi}{6})))})d(\omega_0 t)$$
$$+\frac{1}{2\pi^2}\int_{\frac{2\pi}{3}}^{\pi} \ell^{-jn\omega_0 t}(\ell^{j(m\pi(1+M\cos(\omega_0 t+\frac{\pi}{6})))} - \ell^{-j(m\pi(1+M\cos(\omega_0 t+\frac{\pi}{6})))})d(\omega_0 t)+ \quad (4\text{-}28)$$
$$\frac{1}{2\pi^2}\int_{\frac{4\pi}{3}}^{\frac{5\pi}{3}} \ell^{-jn\omega_0 t}(\ell^{j(m\pi(M\cos(\omega_0 t-\frac{\pi}{6})))} - \ell^{-j(m\pi(M\cos(\omega_0 t-\frac{\pi}{6})))})d(\omega_0 t)+$$
$$\frac{1}{2\pi^2}\int_{\frac{5\pi}{3}}^{2\pi} \ell^{-jn\omega_0 t}(\ell^{j(m\pi(1+M\cos(\omega_0 t+\frac{\pi}{6})))} - \ell^{-j(m\pi(1+M\cos(\omega_0 t+\frac{\pi}{6})))})d(\omega_0 t)$$

The noise source model under DPWM can be calculated by adding C_{amn}, C_{bmn} and C_{cmn} together. Fig. 4.12 illustrates the CM noise source model for all three phases under DSPWM method at switching frequency (20 kHz) and its harmonics range and the sideband impact is taken into account. It shows different trend at switching frequency from continuous PWM method as modulation index changes. The modulation index varies from 0.1 to 0.75. The sideband effect appears without regard to modulation index. When M is 0.75 the amplitude at switching frequency 20k Hz is highest. And it drops as the modulation index decreases. There is about 10dB difference between the amplitude under 0.75 and that under 0.1. Up to higher frequency with 1 MHz range, the noise source envelop shows the same trend as continuous PWM schemes. It is highest when M is 0.1 and it drops about 10 dB as the modulation index increases to 0.75.

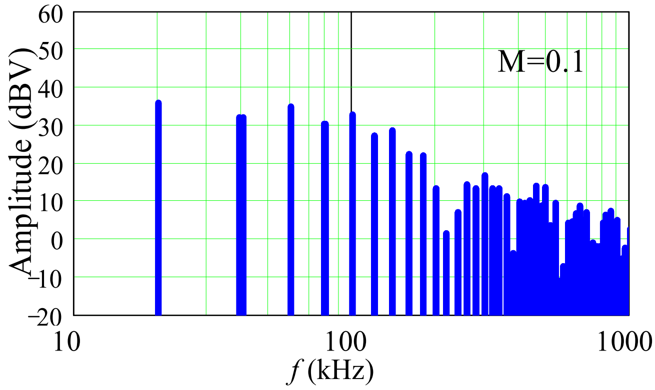

(a) M=0.1

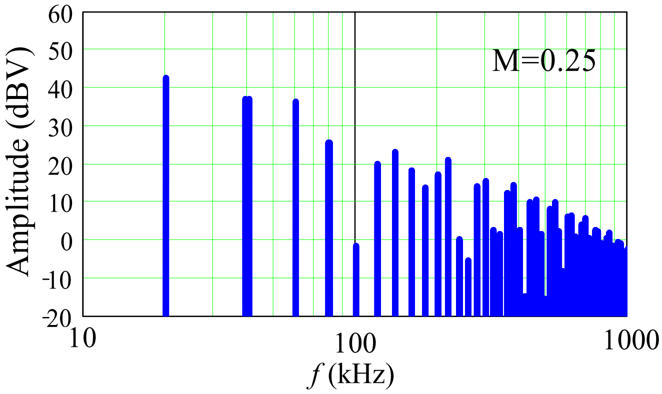

(b) M=0.25

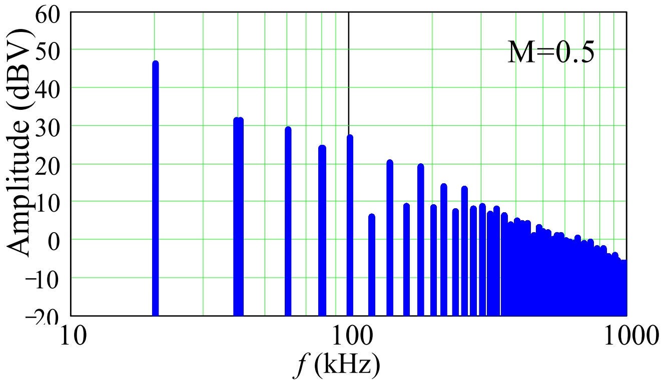

(c) M=0.5

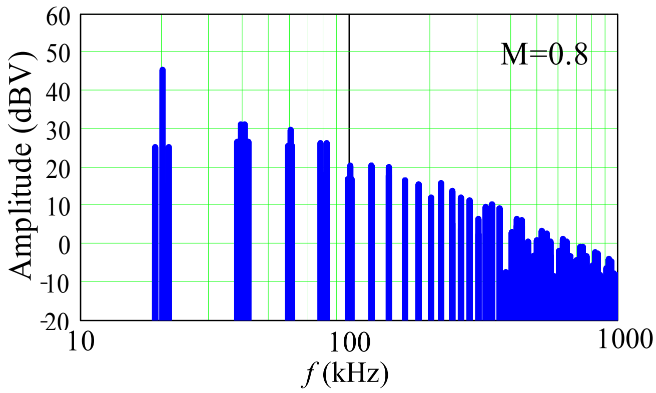

(d) M=0.75

Fig. 4.12 CM noise source model under DPWM with different modulation index

4.4 High frequency CM mode noise model for inverter-based on parasitic resonance

The above present noise propagation path model neglect the parasitics inductance from inverter board and parasitic capacitance and inductance from the device. This method is suitable for a quick EMI analysis and prediction without knowing too much detail circuit parasitics is good to predict inverter CM EMI up to MHz range. The limitation of this method is that it lacks of the accuracy up to tens of MHz range where the resonance between inverter board parasitics and devices parasitics dominate. If the aim is to obtain reasonable accuracy up to tens of MHz range, the critical parasitic of inverter layout such as dc bus parasitic capacitance, device parasitic inductance and output capacitance has be to included in the model.

A method is verified for the resonant peak prediction in CM EMI spectrum of single phase chopper in Chapter 2, and we attempt to extend this methodology to three phase operation. This principle of this method is to calculate the noise voltage across the parasitic capacitance between the device and ground around the resonant frequency from the high frequency equivalent circuit, then add it to the noise voltage source for switching frequency and its harmonics given in (4-3). Hence, the first step is to derive the high frequency equivalent circuit and calculate the noise voltage across the parasitc capacitance around resonant frequency.

Fig. 4.13 shows a high frequency equivalent circuit for CM EMI modeling for three-phase inverter, which is for the prediction of parasitic resonance in EMI spectrum. This model consists of parasitic values extracted in Chapter 3, which are device lead inductance L_{IGBT}, dc bus parasitic inductance L_A, L_B and L_C, and dc bus capacitor inductance and resistance. C_{out} is device output parasitic capacitance as the combination of the output capacitance of IGBT and the junction capacitance of the anti-parallel diode. R is device on resistance plus AC resistance of the circuit which acts as damping factor for the resonance. Because there must be two cases, either top device on and bottom device off or top device off and bottom device on, in the phase leg of inverter operation, the phase leg can be model as L_{IGBT} in series with R for on device and L_{IGBT} in series with C_{out} for off device. The noise source is a step voltage with finite rising time, which represents turn-on and turn-off transition.

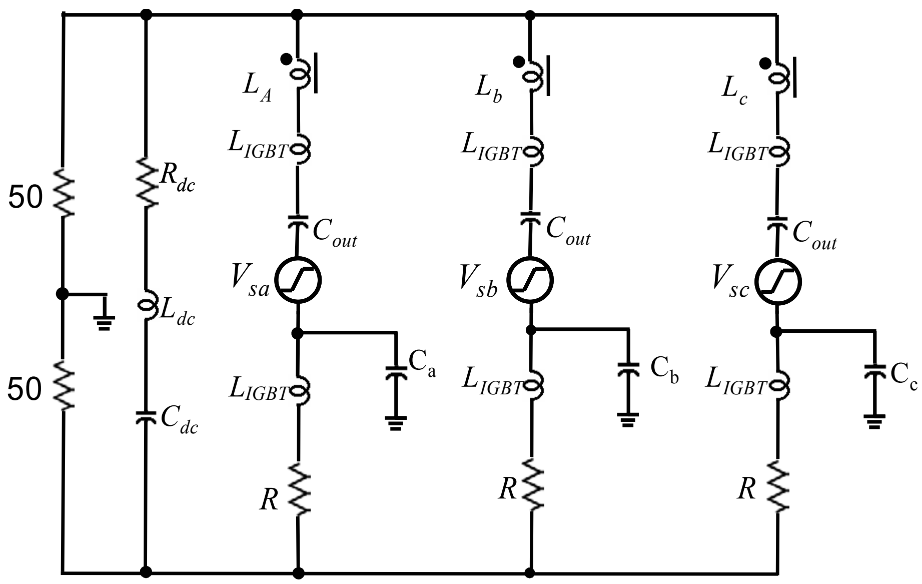

Fig. 4.13 High frequency model for CM EMI modeling

As pointed out in the previous analysis, the critical part of CM EMI modeling and prediction is the voltage across the parasitic capacitance between the device and ground. Each voltage source in Fig. 4.13 will impose voltage on C_a, C_b and C_c respectively during switching transition. For instance, Fig. 4.14 shows the equivalent circuit of three phase inverter during switching transition of phase A. The voltage source for phase B and phase C can be regarded as short circuit because only one phase is switching during switching transition for three phase operation. The sum of the voltage across the parasitic capacitance between device and ground is given by

$$v_r = v_a + v_b + v_c \tag{4-29}$$

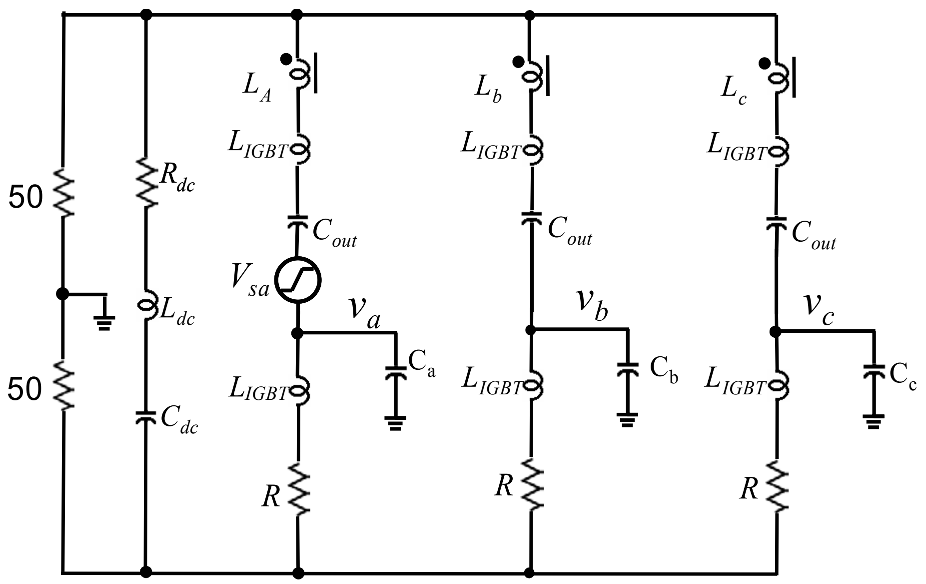

Fig. 4.14 Equivalent circuit during switching transition of phase A

The transfer function between V_r and V_{sa} can be obtained by solving the equivalent circuit show in Fig. 4.14. Equally, the transfer function between V_r and V_{sb}, V_r and V_{sc} can be calculated using the equivalent circuits during switching transition of phase B and phase C. These transfer function are defined by

$$Z_a = \frac{v_r(f)}{V_{sa}(f)}, Z_b = \frac{v_r(f)}{V_{sb}(f)}, Z_c = \frac{v_r(f)}{V_{sc}(f)} \quad (4\text{-}30)$$

Fig. 4.15 shows the plot of the voltage transfer functions from the step voltage source of each phase to v_r. The parameters in the circuit are L_{IGBT}=20.04 nH, C_{out}=0.6 nF, C_{dc}=620 uF, L_{dc}=100 nH and R_{dc}=15 mΩ. It can be seen that the amplitude and resonant frequency of the first resonant points are identical for the transfer function of each phase. This resonant frequency is the same as that calculated in Chapter 3 as a result of the resonance between the loop inductance and the parasitic output capacitance of the IGBT. This also indicates the interaction between the differential mode noise and common mode noise. To simplify the further analysis, it is assumed that Z_a=Z_b=Z_c.

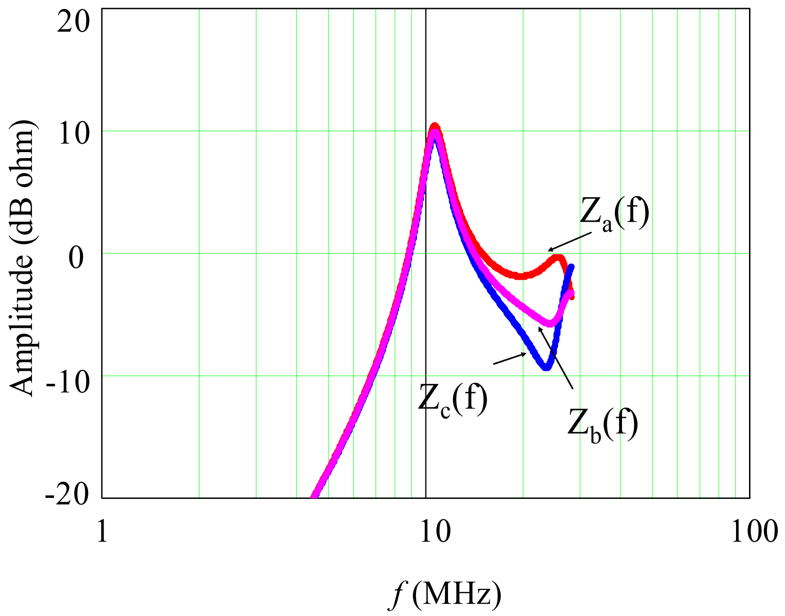

Fig. 4.15 The voltage transfer function of each phase

The frequency expression of the step of the voltage source in given in (4-31)

$$V_s = V_{sa} = V_{sb} = V_{sc} = V_{dc}\left(\frac{1}{s^2\tau_r} - \frac{1}{s^2\tau_r}e^{-s\tau_r}\right) \tag{4-31}$$

where τ_r is the rising time of the voltage step. Thus, v_r can be calculated using (4-30). However, the result will be in the form of Laplace transform that is non-periodic transform. To transfer this result to Fourier series that is periodic transform, the switching period must be taken into account. Fig. 4.16 shows the switching function of inverter during a switching period with different PWM schemes. It is shown that there are 6 switching transitions for SVM or SPWM, while there are 4 switching transitions for DSPWM.

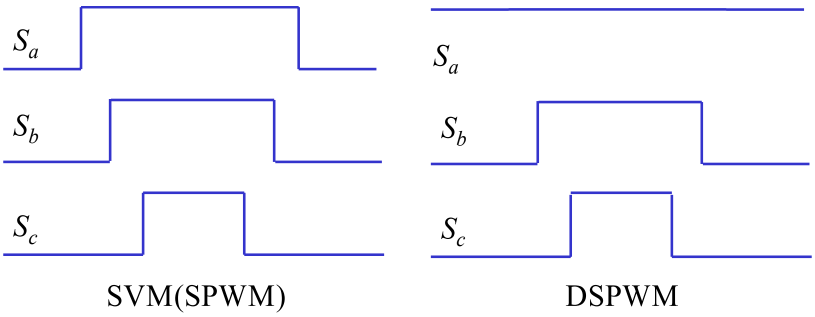

Fig. 4.16 Switching function under different scheme

Therefore, the Fourier series of noise source v_r can be obtained for different PWM operation respectively. (4-32) shows that for SVM or SPWM operation and (4-33) for DSPWM operation. Note that $\sqrt{2}$ accounts for the rms value of spectrum analyzer.

$$v_r(j\omega) = \frac{V_s(j\omega)}{\sqrt{2}T/6} Z_a = 3\sqrt{2}V_{dc}T\left(\frac{1}{(j\omega)^2\tau_r} - \frac{1}{(j\omega)^2\tau_r}e^{-(j\omega)\tau_r}\right)Z_a \quad (4\text{-}32)$$

$$v_r(j\omega) = \frac{V_s(j\omega)}{\sqrt{2}T/4} Z_a = 2\sqrt{2}V_{dc}T\left(\frac{1}{(j\omega)^2\tau_r} - \frac{1}{(j\omega)^2\tau_r}e^{-(j\omega)\tau_r}\right)Z_a \quad (4\text{-}33)$$

The CM EMI spectrum in wide frequency range thus can be calculated using (4-34)

$$V_{cm}(f) = \frac{V_n(f) + v_r(j2\pi f)}{Z(f)} \quad (4\text{-}34)$$

where, Vn(f) is the noise voltage source in (4-3) and Z(f) is the transfer function of noise propagation path shown in Fig. 4.6.

4.5 Experimental Verification

To validate the proposed modeling and calculation method, the high frequency noise produced by the inverter has to be measured. Fig. 4.17 shows the test setup for the CM EMI. A set of LISNs are placed between the battery source and the inverter under test. The LISN provides 50-ohm impedance matching for entire high frequency range. The output of the LISN can be connected to oscilloscope or spectrum analyzer to obtain the spectrum. A two way 0-degree power combiner manufactured by Mini-Circuits is used to extract the CM noise. The different PWM schemes are programmed and the signals are sent out by a digital signal processor (DSP) – ADMC 401™. To isolate the noise from the load side and completely concentrate the noise generated from the inverter side, the inverter will operate under no load condition. The switching frequency is 20 kHz, the fundamental frequency is 200 Hz and the dc bus voltage is 200 V.

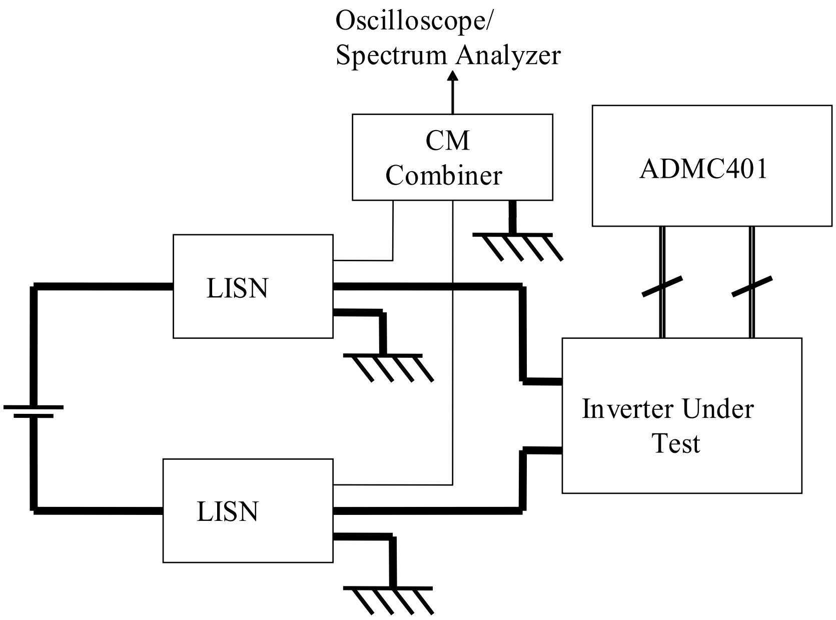

Fig. 4.17 inverter CM EMI test setup

The first part is to verify the impact of different PWM schemes and modulation index on the EMI spectrum in the switching frequency and its harmonics range. The CM EMI spectrum of inverter in the switching frequency and its harmonics range can be calculated using (4-3) based on the source and path models derived in sections 4.3.2. Note that the total LISN impedance should be taken into account because it is not exactly 50Ω at switching frequency and related harmonics. The modulation index varies from 0.1 to 0.75. Fig. 4.18 shows the calculated results under SPWM scheme with different modulation index, which are compared with experimental results in Fig. 4.19. The calculated results match using the frequency domain method matches the experimental result very precisely. The impact of modulation index on EMI spectrum is also shown which further verifies the noise source model. The amplitude at switching frequency is highest when M is 0.1. And it drops as the modulation index increases. There is about 5 dB difference between the amplitude under 0.1 and that under 0.75. Besides, the noise source envelop within 1 MHz range is highest when M is 0.1 and it drops about 8 dB as the modulation index increases to 0.75. Note that there are differences at the second harmonics of switching frequency between calculated result and experimental result when modulation index is low, this is due to the background noise in the measurement that are neglected in the calculation.

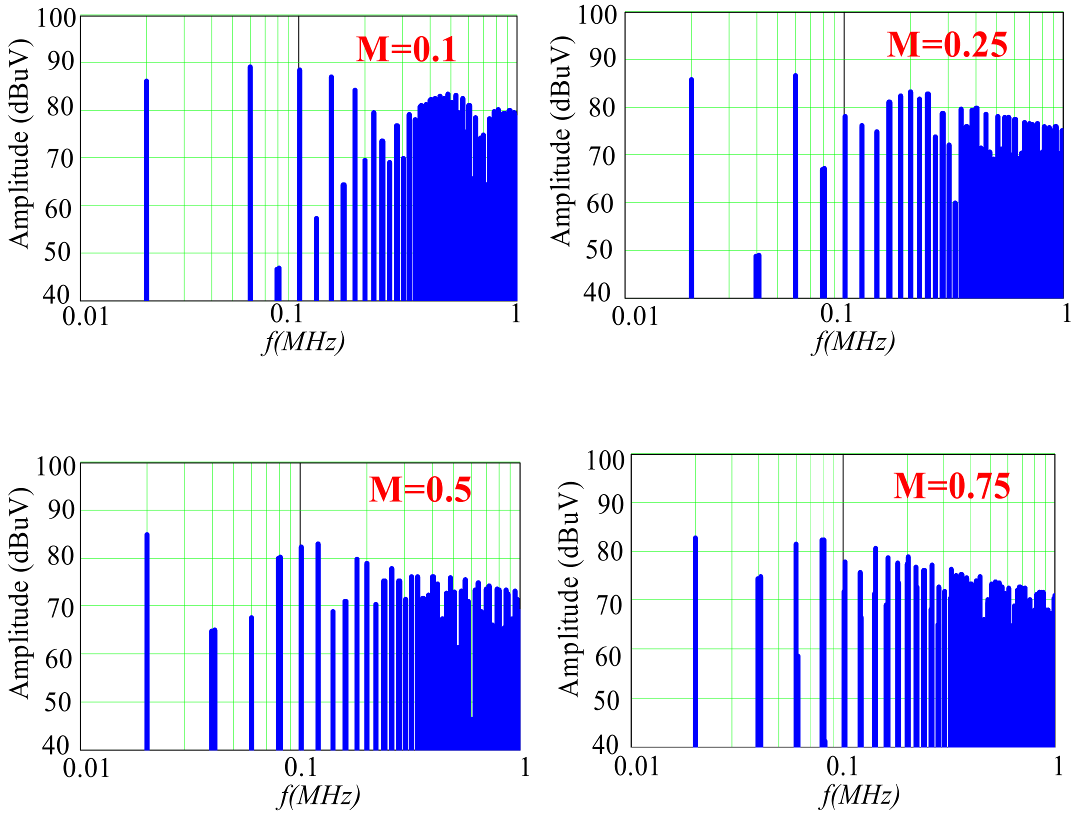

Fig. 4.18 Calculated EMI spectrum under SPWM

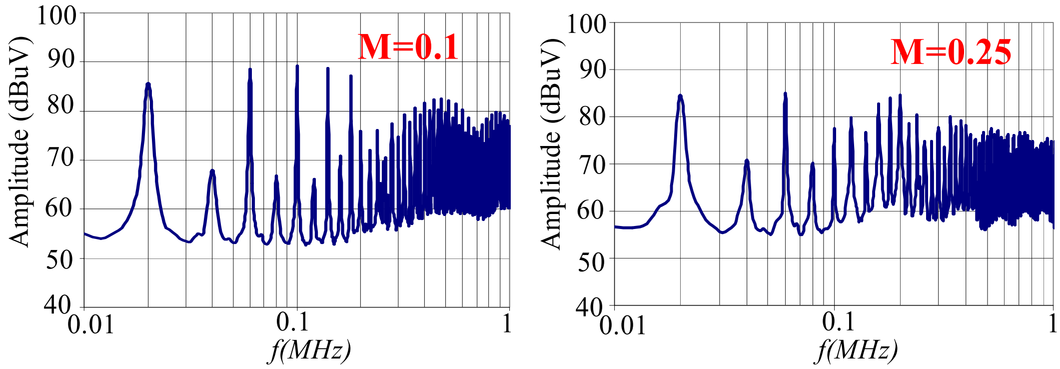

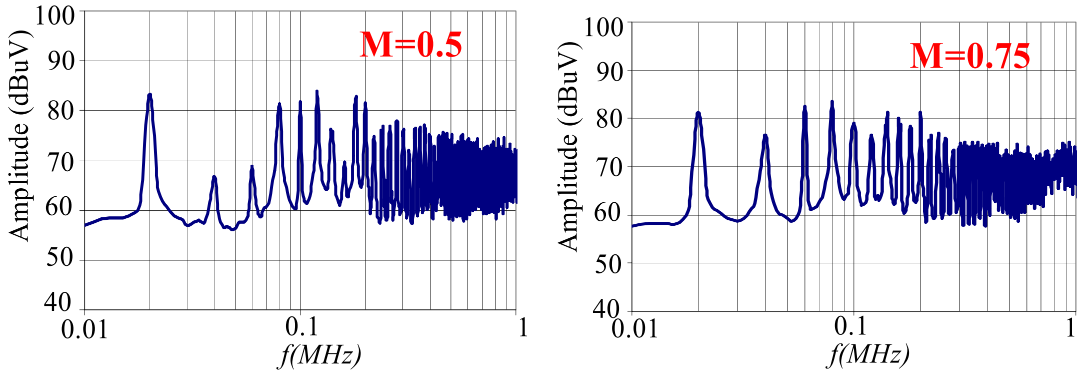

Fig. 4.19 Experimental CM EMI results under SPWM

Fig. 4.20 shows the calculated results and Fig. 4.21 shows the experimental result under SVM scheme with different modulation index. The impact of modulation index on EMI spectrum is also shown in experimental result and the calculated results match using matches the experimental result very precisely. The results show the same distinction of the EMI spectrum as those under SPWM scheme. The amplitude at switching frequency is highest when M is 0.1. And it drops as the modulation index increases. There is about 5 dB difference between the amplitude under 0.1 and that under 0.75. Besides, the noise source envelop within 1 MHz range is highest when M is 0.1 and it drops about 5 dB as the modulation index increases to 0.75.

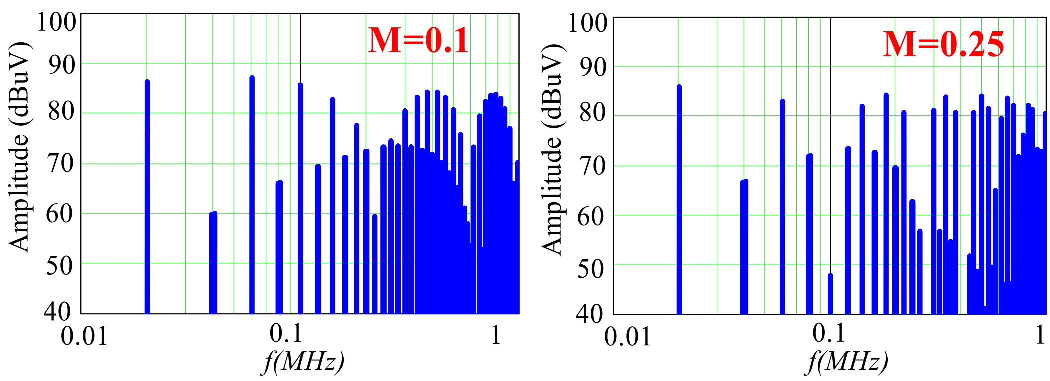

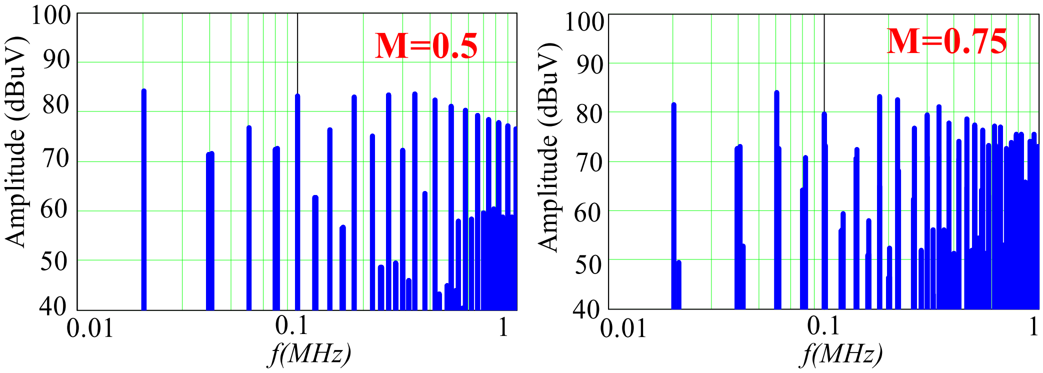

Fig. 4.20 Calculated EMI spectrum under SVM

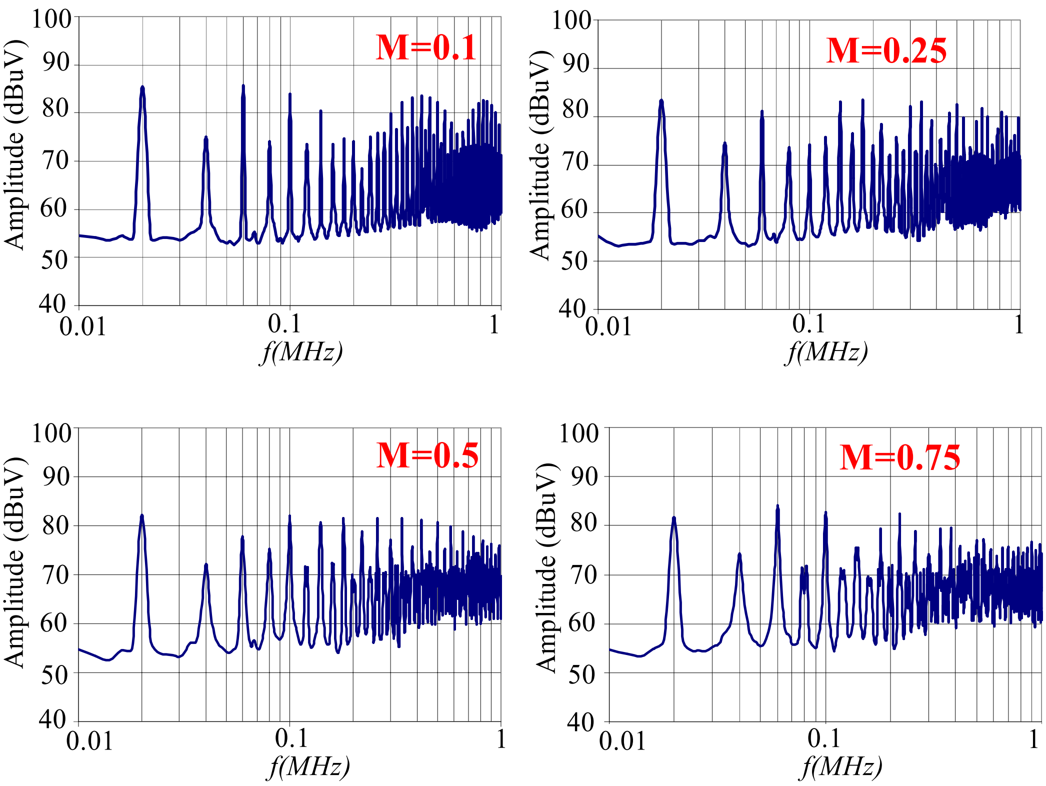

Fig. 4.21 Experimental CM EMI results under SVM

The calculated results of EMI spectrum under DPWM scheme are shown in Fig. 4.22 and the experimental result is shown in Fig. 4.23. In contrast to the results under continuous PWM scheme, it shows different trend as modulation index changes. When M is 0.75 the amplitude at switching frequency 20k Hz is highest. And it drops as the modulation index decreases. This is opposite to the result under SPWM and SVM scheme and there is about 10dB difference between the amplitude under 0.75 and that under 0.1. However, up to higher frequency with 1 MHz range, the noise source envelop shows the same trend as continuous PWM schemes. It is highest when M is 0.1 and it drops about 3 dB as the modulation index increases to 0.75.

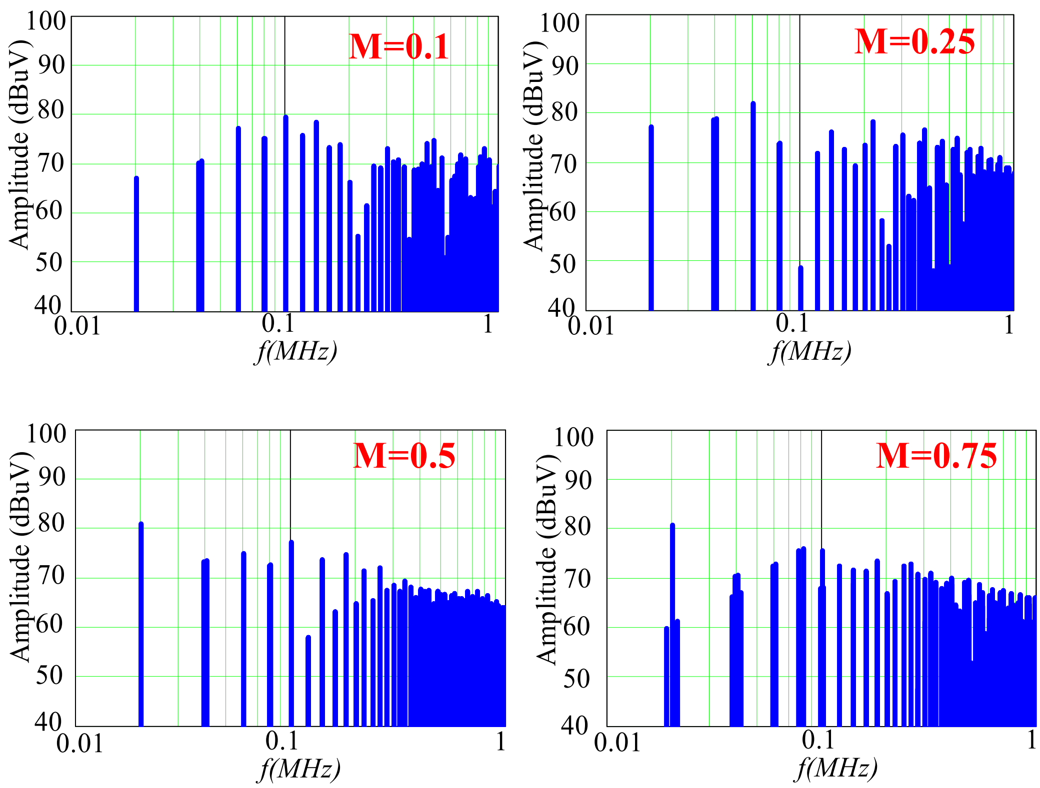

Fig. 4.22 Calculated EMI spectrum under DPWM

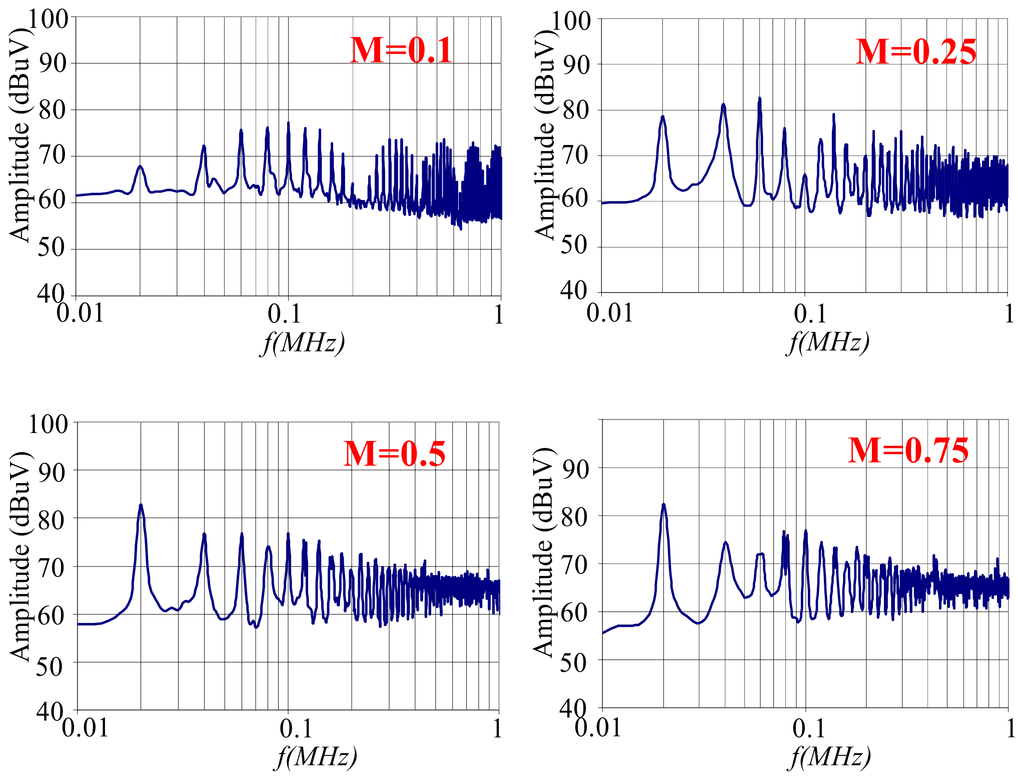

Fig. 4.23 Experimental EMI spectrum under DPWM

The next part is to verify the prediction in the high frequency range up to tens of MHz. The CM EMI spectrum of inverter can be calculated using (4-34) with the consideration of effect of parasitics resonance. The extracted circuit parameter is given in Chapter 3. The finite voltage rise time is 50 ns. Fig.4.24, Fig. 4.25 and Fig. 4.26 shows the calculated and experiment results of CM EMI spectrum under different modulation schemes. In high frequency range, the resonant point matches well between the calculated and the experimental results, which indicates that the resonant points of the noise propagation path determine the location of the peak of the CM EMI spectrum. DPWM gives the lowest noise peak around 11 MHz, which is about 4 dB less than that under continuous PWM scheme. This is due to less switching action of DPWM scheme. SVM gives the highest noise envelop in the frequency range from 200 kHz to 3 MHz. Fig. 4. 25

and Fig. 4.26 also shows the differences between calculated results and experimental results in the frequency range from 1 MHz to 6 MHz. The differences are caused by the background noise from the gate drive and auxiliary power supply. Fig. 4.27 shows the CM background noise and it can be seen that the noise level is around 70 dBuV from 1 MHz to 6 MHz, which is higher than the calculated results. In other words, under DPWM schemes, gate drive and auxiliary power supply cause more CM noise than inverter itself in the frequency range from 1 MHz to 6 MHz.

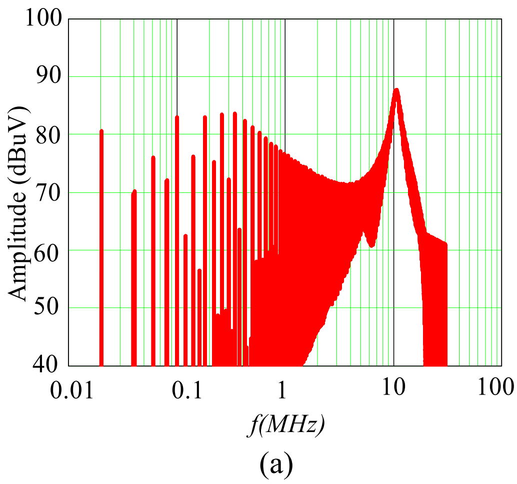

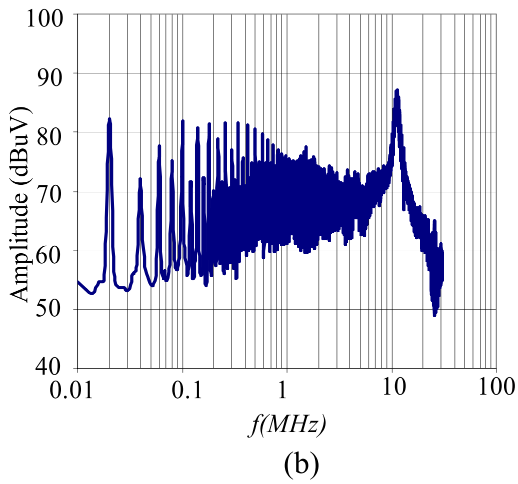

Fig. 4.24 EMI Spectrum comparison in high frequency range under SVM (a) Calculated result (b) Experimental result

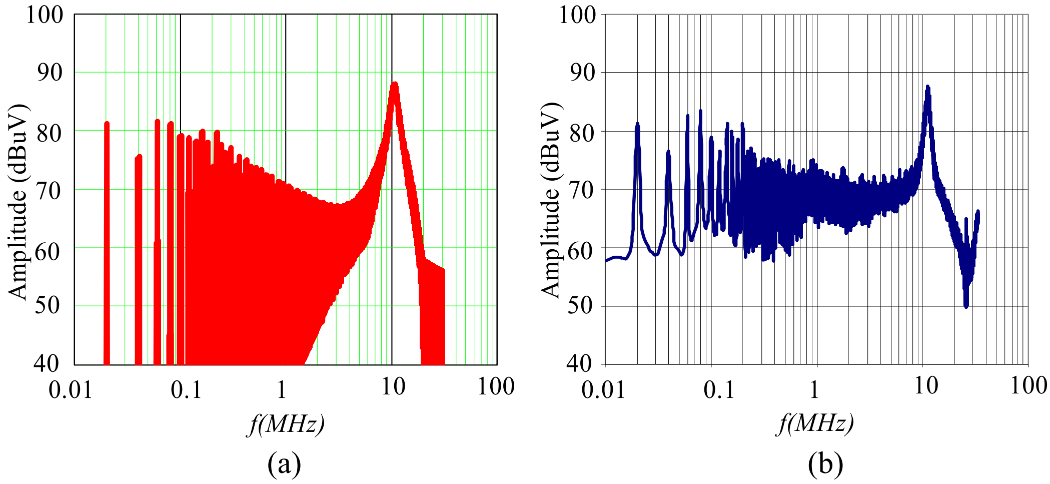

Fig. 4.25 EMI Spectrum comparison in high frequency range under SPWM (a) Calculated result (b) Experimental result

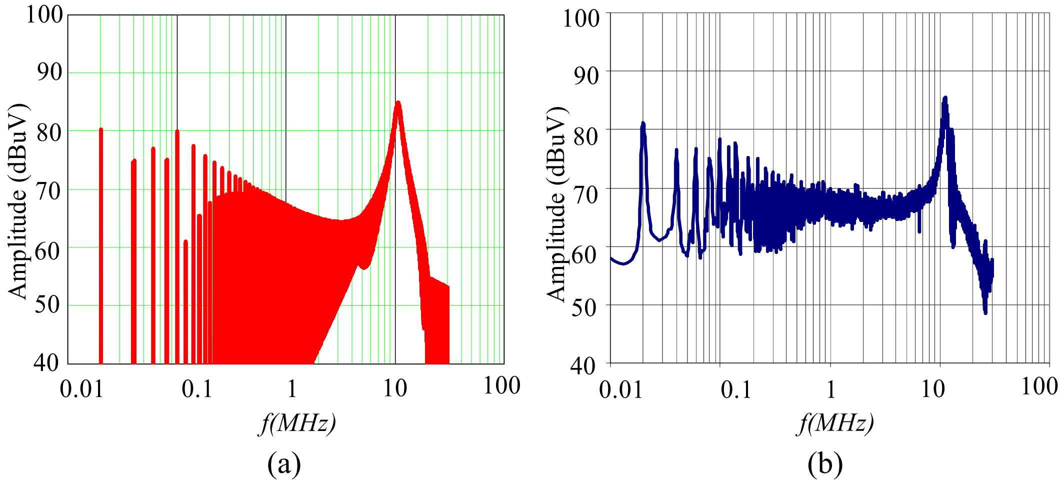

Fig. 4.26 EMI Spectrum comparison in high frequency range under DPWM (a) Calculated result (b) Experimental result

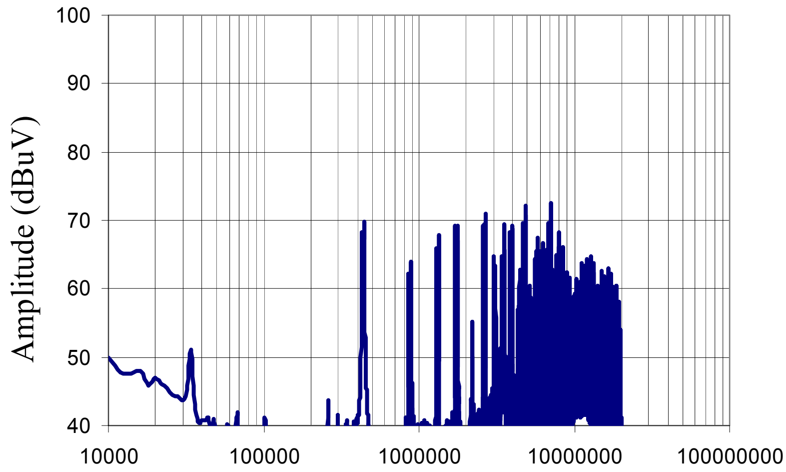

Fig. 4.27 CM background noise

Fig. 4.28 shows the phase voltage waveform in a switching period. It shows the high frequency ringing caused by the switching of other phases.

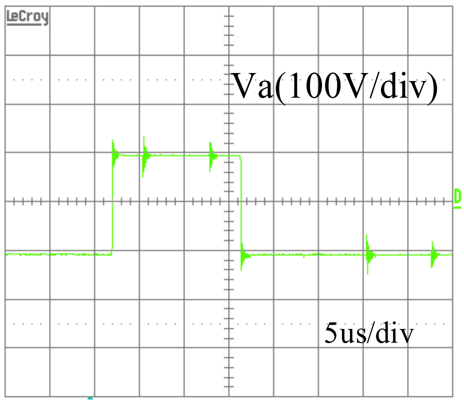

Fig. 4.28 Parasitic ringing in the phase voltage

Fig. 4.29 shows the phase voltage waveform during the switching transition. The high frequency ringing can be seen during turn-on and turn-off. This ringing frequency matches the resonant frequency in the CM EMI spectrum. This explains that the parasitics ringing of the phase voltage is a major noise source of CM noise in high frequency.

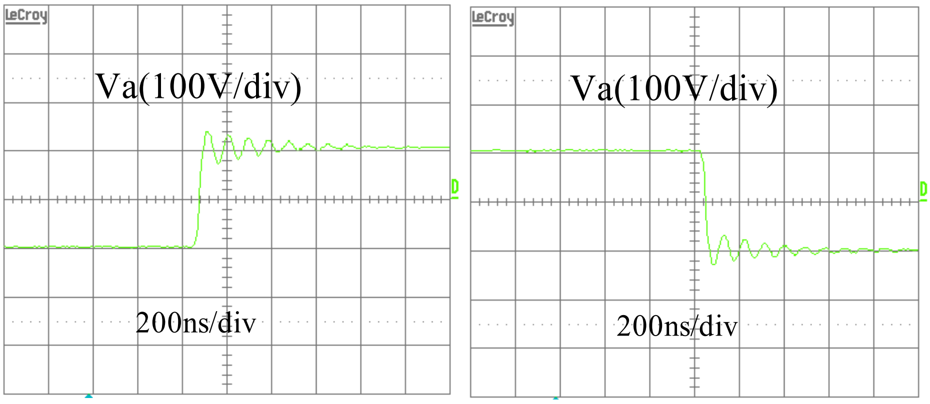

(a) (b)

Fig. 4.29 Phase voltage waveform during switching transition (a) turn-off (b) turn-on

4.6 Summary

A frequency domain approach to prediction of CM conducted EMI from three-phase inverter has been presented. Unlike the conventional method, this approach focuses on the inverter side for the identification of noise source and parasitic parameters of the inverter components to predict the CM EMI currents produced in an inverter circuit. A simplified CM circuit model is proposed and the noise source model is analytically derived. It can predict the CM EMI in switching frequency and its harmonics range. High frequency equivalent circuit model is derived with extracted parasitic parameters of the inverter circuit to predict the noise peak caused by the resonance of parasitic components. With accurate noise source and path models, the proposed "frequency-domain analysis" method effectively predicts the CM EMI performance not only in switching frequency and its harmonics range but also in high frequency range.

The effect of different modulation schemes on CM EMI spectrum are evaluated through frequency domain method analytically. Different modulation schemes lead to different noise sources, which are represented in frequency domain respectively. The calculated results have been verified through experiments. The EMI performance, however, is highly affected by the modulation scheme both in the switching frequency related harmonic frequencies and in the noise path related resonant frequencies. In high frequency range, DPWM gives lowest noise envelop due to less switching action.

The impact of modulation index on CM EMI spectrum with different modulation schemes also evaluated analytically through frequency domain methods. Major impact occurs at the switching frequency and its harmonics range. For Continuous PWM scheme, the lower the modulation index, the higher the noise amplitude at the switching frequency. For DPWM scheme, the higher the modulation index, the higher the noise amplitude at the switching frequency.

Chapter 5 Conclusion and Future work

With the increasing application of power inverter based motor drives in specialty areas where EMC requirements are more stringent than the traditional industrial drive environment, the research of EMI modeling, simulation and prediction for three phase inverter has become imminent. The dissertation proposes the frequency domain method to analyze and model both DM and CM EMIs from a three phase inverter.

5.1 Conclusion

A part of phase leg in the inverter circuit, single phase chopper was first studied as the starting point for the investigation of EMI modeling and prediction. The conventional model fails to predict DM EMI at high frequencies due to the absence of parasitic components. A new high frequency equivalent model for DM EMI of the chopper circuit is proposed for more accurate prediction. The noise source is the device switching current that is in trapezoidal shape, while the noise propagation path includes the dc capacitor parasitics, dc bus parasitics inductance, device lead inductance and device output capacitance. Based on the equivalent circuit, the closed-form of noise source and noise path can be derived. The calculated DM noise closely matches the measured noise level up to 30 MHz.

The conventional model only considers the trapezoidal waveform as the CM noise source and neglects the voltage ringing as additional important noise source in high frequency range, which results in the inaccuracy of the prediction in high frequency range. The propose CM noise source model consists two parts, one is trapezoidal voltage waveform, the other is the voltage ringing caused by either switching current or switching voltage. The frequency domain equivalent circuit for CM modeling is derived and the closed forms of this noise source expression in frequency domain are presented. The experimental CM EMI spectrum agrees well with the predicted result.

The noise source and noise propagation path can be altered by changing switching speed or adding high frequency capacitor across the dc bus. The switching speed variation achieved by different gate resistance value will have effect on EMI in high frequency range. The large the gate resistance is, the lower the EMI spectrum. However, slower switching speed will lead to more switching loss of the converter. Therefore there should be a tradeoff between converter efficiency and EMI performance when designing the converter at system level. Adding high frequency capacitor will not only add additional path of DM noise propagation but also change the CM noise source in high frequency region by suppressing voltage spike during switching transient, thus producing different spectrum for both CM EMI noise and DM EMI noise. Its impact was clearly demonstrated through frequency domain analysis and hardware experiments.

After matching the predicted DM, CM and total noise level from frequency domain analysis closely with the hardware measurement for the single phase circuit, the dissertation extended the same method to three phase inverter circuits. A frequency domain approach to predicting DM conducted EMI from three-phase inverter was presented. The complexity of PWM pattern of three phase inverter has been taken into account. This approach determines the noise source based on inverter operation and

PWM scheme and identifies the noise path on extraction of parasitic parameters of the inverter components. The analytical expression of DM noise source model was derived based on double Fourier technique. Methodologies for extraction of parasitic parameters of the inverter circuit are developed using finite element analysis. Based on the proposed high frequency equivalent of DM, the proposed method can predict EMI spectrum not only at switching frequency and its harmonics range, but also at high frequency range.

The effects of three different modulation schemes on DM EMI spectrum are analytically evaluated through frequency domain method and verified through experiment. Different modulation schemes lead to different noise sources, which are derived using double Fourier integral technique in frequency domain respectively. However the noise path is generic and its associated resonant frequency is the same regardless of the modulation scheme. The modulation schemes affect the EMI performance both in the switching frequency related harmonic frequencies and in the noise path related resonant frequencies. In high frequencies, the center-aligned SVM gives the highest noise envelop and DPWM gives lowest noise envelop. The DPWM has a significant portion running with zero duty, and thus overall producing lowest noise source in frequency domain including in high frequency regions where the EMI performance is mainly dominated by the noise path related impedance. The SVM, though, produces lowest peak EMI amplitude at the switching frequency, with more than 10 dB reduction over the other two methods.

The frequency domain approach to predicting CM conducted EMI from three-phase inverter was proposed. The proposed approach focuses on the inverter side instead of ac load side to identify the CM noise source and parasitic parameters of the inverter components in order to predict the CM EMI currents. A simplified CM circuit model of CM EMI in switching frequency and its harmonics range is proposed first and the noise source models under different modulation schemes are analytically derived through double Fourier integral technique. To predict the CM EMI up to tens of Mega Hz range, additional CM noise source caused by voltage ringing is identified. A CM high frequency equivalent circuit model is derived with extracted parasitic parameters of the inverter circuit to predict the noise peak caused by the resonance of parasitic components. Compared with experimental results, the proposed "frequency-domain analysis" method effectively predicts the CM EMI performance not only in switching frequency and its harmonics range but also in the high frequency range.

The modulation schemes also affect the CM EMI both in the switching frequency related harmonic frequencies and in the noise path related resonant frequencies due to the different noise source in frequency domain. In high frequency range, discontinuous PWM gives lowest noise envelop due to less switching action. The impact of modulation index on CM EMI spectrum with different modulation schemes also evaluated analytically through frequency domain methods. The impact mainly occurs in the switching frequency and its harmonics range up to MHz range. For Continuous PWM scheme, the lower the modulation index, the higher the noise amplitude at switching frequency. For DPWM scheme, the higher the modulation index, the higher the noise amplitude at switching frequency. Up to High frequency range, continuous and discontinuous PWM scheme show the same trend. The CM EMI spectrum becomes lower as modulation index increases. The experimental results verify these phenomenons.

5.2 Summary of research contributions

This dissertation is dedicated to the development of frequency domain analysis of EMI modeling and prediction for a three phase inverter circuit. The research starts the CM and DM EMI analysis from a part of inverter phase leg, which is a single phase chopper circuits, then extends the results to three phase inverter with complex PWM pattern.

The major research contributions associated with this dissertation are listed below.

- A DM high frequency model for single phase chopper is proposed. This model takes account the device parasitics and dc bus parasitics The DM noise source model and noise path model are derived in closed form.
- A CM high frequency model for single phase chopper is proposed. This noise source model not only includes switching characteristic dv/dt, but also voltage parasitic ringing. The noise path model includes the parasitic capacitance device parasitics and dc bus parasitics. The CM noise source model and noise path model are derived in closed form.
- The CM and DM equivalent circuits for three phase inverter are proposed with the consideration of complex PWM pattern. Analytical CM source model and DM source model have been presented using double Fourier technique.

- The effect of modulation schemes on DM and CM EMI for a three phase inverter is analytically evaluated through frequency domain analysis and verified through experiment.
- Based on frequency domain analysis, the impact of modulation indexes on CM EMI for a three phase inverter is evaluated and verified through experiment.
- The insight analysis is provided for the effect of high frequency capacitor on DM and CM EMI.

5.3 Future work

Developing an effective methodology of EMI modeling and prediction not only provides the insight for EMI generation and distribution, but also help optimize the converter design at the design stage. Although it is verified that the predicted result based on the proposed frequency domain method fairly matches the hardware measurement, a lot of works remain necessary for further research. The conducted EMI noise prediction needs to expand from single converter to multi-converter system which includes the dc/ac inverter and dc/dc converter. It is interesting to investigate coupling effect of the noise source and noise path between different converter stages through frequency domain analysis. Also the effect on different grounding schemes on multi-converter system needs to be studied. In addition, since the frequency domain analysis represent the noise source and path models in closed forms, they can be easily integrated into system optimization design softwares to achieve an optimized EMI and thermal design for the converter system.

Reference

A. General literature on EMI

[1] C. R. Paul, "Introduction to electromagnetic compatibility," New York : Wiley, 1992.

[2] Christos Christopoulos, "Principles and techniques of electromagnetic compatibility," CRC Press, 1995.

[3] M. J. Nave, "Power Line filter design for switched-mode power supplies," New York: Van Nostrand Reinhold, 1991.

[4] Laszlo Tihanyi, "Electromagnetic compatibility in power electronics," New York, N.Y., U.S.A, IEEE Press, 1995.

[5] C. R. Paul and K. B. Hardin, "Diagnosis and reduction of conducted noise emissions," IEEE Transaction on Electromagnetic Compatibility, vol. 30, Issue: 4, November 1988, pp. 553-560.

[6] Ting Guo, "Separation of the common-mode and the differential-mode conducted electromagnetic interference noise," Master Thesis, Virginia Polytechnic Institute and State University, February 1994.

[7] I.E. Nobel, "Electromagnetic Compatibility in Automotive Environment", IEE Proc.-Sci. Meas. Technol., Vol. 141, No. 4, Jul. 1994, pp. 252-258.

[8] K. P. Moy, "EMC Related Issues for Power Electronics", Automotive Power Electronics, 1989, pp. 46-53.

[9] R. Redl, "Power electronics and electromagnetics compatibility," in Conf. Rec. of the IEEE Power Electronics Specialists Conference, Milan, Italy, July 1996, pp. 15-21.

B. EMI issures on Motor drive

[10] E. Zhong and T. A. Lipo, "Improvements in EMC performance of inverter-fed motor drives," *IEEE Trans. Ind. Applicat.,* vol. 31, pp. 1247–1256, Nov./Dec. 1995.

[11] A. von Jouanne, P. Enjeti, and W. Gray, "Application issues for PWM adjustable speed ac motor drives," *IEEE Ind. Applicat. Mag.,* pp. 10–18, Sept./Oct. 1996

[12] Y. Murai, T. Kubota and Y. Kawaso, "Leakage current reduction for a high frequency carrier inverter feeding an induction motor," IEEE Trans. on Industry application, Vol.28, No.4, Aug. 1992, pp. 858-863.

[13] S. Ogasawara, H. Ayano and H. Akagi, " Measurement and reduction of EMI radiated by a PWM fed AC motor drive system," IEEE IAS annual Meeting, 1996, pp.1072-1079

[14] S. Ogasawara, and H. Akagi, " Modeling and damping of High Frequency Leakage Currents in PWM Inverter-Fed AC Motor Drive Systems," IEEE Trans. on Industry Applicatons, Vol.32, No. 5, 1996, pp. 1105-1114.

[15] F. Canavero, J.-C. Kedzi, P. RAVIER and B. Scholl, "Automotive EMC: Numerical Simulation for Early EMC Design of Cars", the 4th European Symposium on Electromagnetic Compatibility, EMC Europe 2000, held in Brugge, Belgium on September 11-15, 2000.

[16] S. Dickmann, J.-C. Kedzia, U. Keller, and T. Kiessling, "Analysis of Radiated Electromagnetic Emissions due to Common-Mode Currents Produced by Electronic Equipment"

[17] J. Sach and H. Schmeer, "Computer Aided Analysis of RFI Voltage generation by Small Commutator Motors" Symposium and Technical Exhibition on Electromagnetic Compatibility No. 6, Zurich, 1985, pp. 551-556.

[18] J. M. Erdman, R. J. Kerkman, D. W. Schlegel, and G. L. Skibinski,"Effect of PWM inverters on ac motor bearing currents and shaft voltages," *IEEE Trans. Ind. Applicat.,* vol. 32, pp. 250–259, Mar./Apr. 1996.

[19] E. Persson, "Transient effects in application of PWM inverters to induction motors," *IEEE Trans. Ind. Applicat.,* vol. 28, pp. 1095–1100, Sept./Oct. 1992.

[20] Von Jouanne, P. Enjeti, and W. Gray, "The effects of long motor leads on PWM inverter fed AC motor drive systems," in Conf. Rec. of IEEE Applied Power Electronics Conference, 1995, pp. 592-597.

[21] R. Kerkman, D. Leggate, and G. Skibinski, “Interaction of drive modulation and cable parameters on ac motor transients,” *IEEE Trans. Ind. Applicat.*, vol. 33, pp. 722–731, May/June 1997.

[22] A. Boglietti, E. Carpaneto, "Induction Motor High Frequency Model", 34th IEEE-IAS Annual Meeting, Phoenix, Arizona USA, October 1999, pp. 1551-1558.

[23] G. Grandi, D. Casadei, A. Massarini, "High Frequency Lumped Parameter Model for AC Motor Windings", EPE 1997, Trondheim, Norwegen, pp. 2578-2583.

[24] S. Chen, T. A. Lipo and D. Fitzgerald, "Source of Induction Motor Bearing Currents Caused by PWM Inverters", IEEE Transactions on Energy Conversion, Vol. 11, No. 1, March 1996, pp. 25-32.

[25] S. Chen, T. A. Lipo, D. Fitzgerald, “Modeling of motor bearing currents in PWM inverter drives,” in Conf. Rec. of IEEE IAS Annual Meeting, 1995, pp. 388-393.

[26] S. Chen, "Generation and Suppression of Conducted EMI from Inverter Motor Drives," Conference Record of IEEE IAS Annual Meeting, Phoenix, Arizona, 3-7 October 1999, pp. 1583-1589.

[27] G. Skibinski, J. Pankau, et al., “Generation, control and regulation of EMI from AC drives,” in Conf. Rec. of IEEE IAS Annual Meeting, 1997, pp. 1571-1583.

C. Literature on Parasitics Extraction

[28] E. Falck, M. Stoisiek, and G. Wachutka, “ Modeling of parasitic inductive effects in power modules,” Proc. Of the IEEE international Symposium on Power Semiconductor Devices and IC’s, May 1997, pp.129-132.

[29] A. E. Ruehli, “ Equivalent Ciruit Models for three-dimensional Multiconductor Systems,” IEEE Trans on Microwave Theory and Tech., Vol. 22, March 1974, pp. 216-221.

[30] J. L. Schanen, E. Clavel, and J. Roudet, “Modeling of Low Inductance busbar connections,” IEEE Industry Applications Magazine, Sept. 1996, pp.39-43.

[31] A. E. Ruehli and A. C. Cangellaris, "Progress in the methodologies for the electrical modeling of interconnects and electronic packages," Proc. IEEE, vol. 89, no. 5, pp. 740-771, 2001.

[32] H. Zhu, A. R. Hefner, Jr., J.-S. Lai, "Characterization of power electronics system interconnect parasitics using time domain reflectometry," in Conf. Rec. of IEEE Power Electronics Specialists Conference, May 1998, pp. 1937-1943.

[33] M. K. Kazimierczuck, G. Sancineto, G. Grandi, U. Reggiani and A. Massarini, " High frequency Small-Signal Model of Ferrite Core Inductors", IEEE Transactions on Magnetics, Vol. 35, No. 5, September 1999, pp. 4185-4191.

[34] A. Massarini, M.K. Kazimierczuk, and G. Grandi, "Lumped Parameter Models for Single- and Multiple-Layer Indutors", Proceedings of Power Electron. Specialist Conf., Baveno, June 1996.

[35] A. Massarini, M.K. Kazimierczuk, "Self-Capacitance of Inductors", IEEE Transactions on Power Electronics, Vol. 12, No. 4, July 1997, pp. 671-676.

D. Modeling and Predition of EMI

[36] G. Antonini, S. Cristina and A. Orlandi, " A Prediction Model of Electromagnetic Interferences Radiated by an Industrial Power Drive System", IEEE Transactions on Industry Applications, Vol. 35, No. 4, July/August 1999, pp. 870-876.

[37] C.R. Suriano, J. R. Suriano, G. Thiele, T.W. Holmes, "Prediction of Radiated Emissions from DC Motors", 1998 IEEE International Symposium on Electromagnetic Compatibility, Vol. 2, 1998, pp. 790 –795.

[38] E. Laboure, F. Costa, C. Gautier and W. Melhem, "Accurate Simulation of Conducted Interference Isolated DC to DC Converters Regarding to EMI Standards," IEEE PESC 96, pp. 1973-1978

[39] Philip F. Okyere and L. Heinemannn, " Computer-Aided Analysis and reduction of Conducted EMI in Switched Mode Power Converter," IEEE APEC 1998, pp. 924-928

[40] V. Prasad Kodali, “Engineering electromagnetic compatibility: principles, measurements, technologies and computer models,” New York, N.Y., U.S.A., IEEE Press, 2001.

[41] Hwan-Kyun Yun; Yuen-Chung Kim; Chung-Yuen Won; Young-Ryul Kim; Young-Seok Kim and Se-Wan Choi; “A study on inverter and motor winding for conducted EMI prediction,” *IEEE International Symposium on Industrial Electronics*, 2001, vol. 2, pp. 752 –758.

[42] L. Ran, S. Gokani, et al., “Conducted electromagnetic emissions in induction motor drive systems Part I: Time domain analysis and identification of dominant modes,” IEEE Trans. Power Electron., Vol. 13, No. 4, 1998, pp. 757-767.

[43] Caponet M.C.; Profumo F.; De Doncker R.W.; Tenconi A.*;* “Low Stray Inductance Bus Bar Design and Constrution for Good EMC Performance in Power Electronics Circuits,” Power Electronics, IEEE Transactions on ,Volume: 17 , March 2002 Pages:225 – 231.

[44] Caponet M.C.; Profumo F.; De Doncker R.W.; “Solutions to Minimize Conducted EMI in Power Electronics Circuits,” in Conf. Rec. of IEEE Applied Power Electrnonics Conference, March 2001, pp. 220̃-224.

[45] H. Zhu, J.-S. Lai, Y. Tang, A. Hefner, Jr. D. Berning, and C. Chen “Analysis of Conducted EMI Emissions from PWM Inverter Based on Empirical Models and Comparative Experiments,” in Conf. Rec. of IEEE Power Electroics Specialists Conference., June 1999, pp. 111̃-123.

[46] H. Zhu; J.-S. Lai; A.R. Hefner, Jr.; Y. Tang; and C. Chen, **“**Modeling-Based Examination of Conducted EMI Emissions from Hard- and Soft-switching PWM Inverters**”,** Conf. Rec. IEEE-IAS Annu. Meeting, 1999, Vol. 3 , pp. 1879 -1886.

[47] H. Zhu, Jih-Sheng Lai, A. R. Hefner, Jr., Y. Tang, and C. Chen, “Modeling Based Examination of Conducted EMI Emission from Hard- and Soft-Switching PWM Inverters,” IEEE Transactions on Industry Applications, Sep./Oct., 2001, pp. 1383 – 1393.

[48] M. K.W. Wu, C.K. Tse, O. B. P. Chan, “Development of an Integrated CAD Tool for Switching Power Supply Design with EMC Performance Evaluation”, IEEE Transactions on Industry Applications”, Vol. 34, No. 2, Macrh/April, 1998.

[49] W. Zhang, M.T. Zhang, F.C. Lee, J. Roudet and E. Clavel, “Conducted EMI analysis of a boost PFC circuit,” APEC 1997, vol.1, pp. 223 –229

[50] S. Chen, T. W. Nehl, X. Huang, E. Pepa, R. DeDoncker, and I. Voss, “Towards EMI Prediction of a PM Motor Drive for Automotive Applications,” in *Proc. of IEEE Appl. Power Electron. Conf.*, Miami, FL, Feb. 2003, pp. 14 – 22.

[51] J.-S. Lai, X. Huang, S. Chen and T. Nehl, “EMI Characterization and Simulation with Parasitic Models for A Low-Voltage High Current AC Motor Drive”, *Conf. Rec. IEEE-IAS Annu. Mtg.*, Pittsburgh, PA, Oct. 2002, pp. 2548 – 2554.

[52] G. Grandi, D. Casadei, D. Reggiani, “Common- and Differential-Mode HF Current Components in AC Motors Supplied by Voltage Source Inverters,” IEEE Trans on Power Electronics, Jan. 2004. Vol. 19, No. 1, pp 16-25.

[53] M. Nave, “Prediction of conducted emissions in switched mode power supplies”, *IEEE Int. Symp. on EMC’86*, pp 167-173.

[54] M. Nave, “ The effect of duty cycle on SMPS common mode emission: theory and experiment,” in *Proc. of IEEE Appl. Power Electron. Conf.,* 1989.

[55] C. Chen, **“**Novel EMC debugging methodologies for high-power converters**”,** IEEE International Symposium on Electromagnetic Compatibility, Vol. 1 , 2000 pp. 385 –390.

[56] Liu D. H, Jiang Jianguo. “A Systematic Approach to Analyze EMI in Control Circuit of Power Electronic Equipment,” Proceedings of 16th IEEE APEC, 2001, pp 208-212.

[57] Liu Q., Shen W., et al., “ Experimental Evaluation of IGBTs for Characterizing and Modeling Conducted EMI Emission in PWM Inverters,” in Conf. Rec. of IEEE Power Electronics Specialists Conf., 2003.

[58] Zhang D., Nave M. J. and Sable D., “Measurement of Noise Source Impedance of Off-line Converters,” *IEEE Trans. on Power Electronics*, Sept. 2000, vol. 15, pp. 820-825.

[59] Zhang D., Chen D. Y., and Sable D., “A new method to characterize EMI filters,” *Applied Power Electronics Conference and Exposition*, Feb. 1998, vol.2, pp.929 –933.

[60] J. C. Crebier, J. roudet, and J.L. Schanen, “ A new method for EMI study in PFC rectifer,” in Conf. Rec. of IEEE Power Electronics Specialist Conf. , 1999, PP. 855-867.

[61] J. C. Crebier, J. P. Ferrieux, “PFC Full Bridge Rectifiers EMI Modeling and Analysis-Common Mode Disturbance Reduction,” IEEE Trans on Power Electronics, March 2004, Vol. 19, No.2,.pp378-387.

[62] P. R. Mugur, J. Roudet, and J.-C. Crebier, “Power Electronic Converter EMC Analysis Through State Variable Approach Techniques,” IEEE Trans. Electronmagnetic Compatibility, Vol. 43, No. 2, May 2001, pp. 229 – 238.

[63] P. Bardos; “Predicting the EMC Performance of High Frequency Inverters,” in Conf. Rec. of IEEE Applied Power Electrnonics Conference, March 2001, pp. 213-219.

[64] J.-Luc Schanen, L. Jourdan, J. Roudet, “Layout Optimization to Reduce EMI of a Switched Mode power Supply,” in Conf. Rec. of IEEE Trans. Power Electroics Specialists Conference., June 2002, pp. 2021-2026.

[65] C. Chen, X. Xu, D. M. Divan, “Conductive electromagnetic interference noise evaluation for an actively clamped resonant dc link inverter for electric vehicle traction drive applications,” in Conf. Rec. of IEEE IAS Annual Meeting 1997 1550-1557.

[66] L. Ran, S. Gokani, et al., “Conducted electromagnetic emissions in induction motor drive systems Part II: Frequency domain analysis,” IEEE Trans. Power Electron., Vol. 13, No. 4, 1998, pp. 757-767.

E. Device charateristic and gate drive

[67] C. Licita, S. Musumeci, A. Raciti, et al., “ A new driver circuits for IGBT devices,” IEEE Trans. on Power Electronics Vol.10, May 1995, pp.373-378.

[68] A. Hefner, "An investigation of the drive circuit requirements for the power insulated gate bipolar transistor," *IEEE Trans. Power Electron.*, vol. 6, pp. 208–219, Apr. 1991.

[69] A. Consoli, S. Musumeci, G. Oriti, et al., "An innovative EMI reduction design technique in power converters," Proc. Of International Symposium on EMC, September, 1994, Italy.

[70] A. Guerra, F. Maddaleno, "Effects of Diode Recovery Characteristics on Electromagnetc Noise in PFCs," in Conf. Rec. of IEEE Applied Power Electrnonics Conference, Feb 1998, pp. 944̃-949.

F. PWM scheme on three phase inverter

[71] H. Van Der Broeck, H. Skudelny, and G. Stanke, "Analysis and realization of a pulse width modulator based on voltage space vectors,"in *IEEE-IAS Conf. Rec.*, 1986, pp. 244–251.

[72] S. Ogasawara, H. Akagi, and A. Nabae, "A novel PWM scheme of voltage source inverter based on space vector theory," in *European Power Electron. Conf. Rec.*, Aachen, Germany, 1989, pp. 1197–1202.

[73] A. M. Hava, R. J. Kerkman, and T. A. Lipo, "Simple Analytical and Graphical Methods forCarrier-Based PWM-VSI Drives," *IEEE Trans. Power Electron.*, vol. 14, pp. 49–61, Jan 1999.

[74] D.G. Holmes, "A general analytical method for determining the theorectical harmonic components of carrier based PWM strategies", in *Conf. Rec. of IEEE IAS Annual Meeting*, 1998, pp. 1207−1214

[75] X. Huang, E. Pepa, J-S Lai, S. Chen and T. W. Nehl, "Three-Phase Inverter Differential Mode EMI Modeling and Prediction In Frequency Domain", in Conf. Rec. of *IEEE IAS Annu. Meeting*, 2003.

Vita

The author, Xudong Huang, was born in Harbin, Heilongjiang, P. R. China in 1973. He received the B.S. and M.S. degrees in Electrical Engineering from Harbin Institute of Technology, in 1996 and 1998, respectively. Since August 1999, he has been working towards his Ph. D degree at the Bradley Department of Electrical and Computer Engineering, Virginia Polytechnic institute and State University. Working as research assistant at the Center for Power Electronics System (CPES) and Future Energy Electronics Center (FEEC), his research interests include EMI modeling and prediction, DC/DC converter design, digital control and soft switching technique.